

Osaka Feedback Model II: Modeling Supernova Feedback Based on High-Resolution Simulations

YURI OKU ¹, KENGO TOMIDA ², KENTARO NAGAMINE ^{1,3,4}, IKKOH SHIMIZU,⁵ AND RENYUE CEN ^{6,1}

¹*Theoretical Astrophysics, Department of Earth & Space Science, Graduate School of Science, Osaka University, 1-1 Machikaneyama, Toyonaka, Osaka 560-0043, Japan*

²*Astronomical Institute, Tohoku University, Aoba, Sendai, Miyagi 980-8578, Japan*

³*Kavli IPMU (WPI), The University of Tokyo, 5-1-5 Kashiwanoha, Kashiwa, Chiba 277-8583, Japan*

⁴*Department of Physics & Astronomy, University of Nevada, Las Vegas, 4505 S. Maryland Pkwy, Las Vegas, NV 89154-4002, USA*

⁵*Shikoku Gakuin University, 3-2-1 Bunkyocho, Zentsuji, Kagawa, 765-8505, Japan*

⁶*Department of Astrophysical Sciences, Princeton University, Peyton Hall, Princeton, NJ 08544, USA*

ABSTRACT

Feedback from supernovae (SNe) is an essential mechanism that self-regulates the growth of galaxies, and a better model of SN feedback is still needed in galaxy formation simulations. In the first part of this paper, using an Eulerian hydrodynamic code ATHENA++, we find universal scaling relations for the time evolution of momentum and radius for a superbubble, when the momentum and time are scaled by those at the shell-formation time. In the second part of this paper, we develop an SN feedback model based on the ATHENA++ simulation results utilizing Voronoi tessellation around each star particle, and implement it into the GADGET3-OSAKA smoothed particle hydrodynamic code. Our feedback model was demonstrated to be isotropic and conservative in terms of energy and momentum. We examined the mass/energy/metal loading factors and find that our stochastic thermal feedback model produced galactic outflow that carries metals high above the galactic plane but with weak suppression of star formation. Additional mechanical feedback further suppressed star formation and brought the simulation results in better agreement with the observations of the Kennicutt–Schmidt relation, with all the results being within the uncertainties of observed data. We argue that both thermal and mechanical feedback are necessary for the SN feedback model of galaxy evolution when an individual SN bubble is unresolved.

Keywords: galaxy formation — numerical simulation — stellar feedback — supernovae — galactic winds — star formation

1. INTRODUCTION

It is widely recognized that baryonic feedback processes play vital roles in the formation and evolution of galaxies in the Λ cold dark matter (Λ CDM) universe (e.g., Larson 1974; Blumenthal et al. 1984; Dekel & Silk 1986). Supernova (SN) feedback is one of the most dominant processes; it impacts the interstellar medium (ISM) and circumgalactic medium (CGM) by generating hot bubbles (McKee & Ostriker 1977; Spitzer 1990), driving turbulence (Chevalier 1974; Ostriker & Shetty 2011), and launching galactic winds (Chevalier & Clegg 1985; Veilleux et al. 2005; Strickland & Heckman

2009). Hence, the study of SN feedback becomes necessary to better understand galaxy-formation processes.

It is challenging to spatially and temporally resolve SN explosions in galaxy formation simulations due to a lack of resolution. In the early days of cosmological galaxy simulation (i.e., the 1990s), SN explosions were modeled as thermal energy injections (Cen & Ostriker 1992; Katz et al. 1996; Cen & Ostriker 1999). However, due to low resolution, the thermal energy was dissipated and radiated away as soon as it was injected (i.e., the overcooling problem, Katz 1992).

To model SN feedback, we must consider what to model. As described above, SN feedback affects galaxy evolution via both kinetic feedback (driving turbulence) and thermal feedback (generating hot bubbles and outflows). When the resolution is high enough to resolve

the Sedov–Taylor phase, its kinetic and thermal energies get converted to one another, and the difference between the thermal and kinetic form, or a combination of both forms, is negligible (Durier & Dalla Vecchia 2012). According to Kim & Ostriker (2015), the spatial resolution of $\Delta x = R_{\text{sf}}/3$, where R_{sf} is the shell-formation radius (see equation 7 below), is necessary to resolve the Sedov–Taylor phase. In most cases of cosmological galaxy simulations, such small scales cannot be resolved. Hence, we need to include both kinetic and thermal feedbacks in the SN feedback model. We note that simply distributing thermal energy is ineffective (Hu 2019) because it leaves the mass of the SN ejecta unresolved in simulations as long as we use simple stellar population (SSP) approximation and the particle masses of stars and gas are comparable (Dalla Vecchia & Schaye 2012). Therefore, the effective modeling of thermal feedback is necessary.

There are four key techniques to overcome the overcooling problem: i) ignoring some physical process, e.g., cooling or hydrodynamical interactions, ii) skipping unresolved physics, iii) scaling up the energy dynamics to a resolvable scale, and iv) modeling the unresolved scale.

The first method is to ignore some physical processes to make the thermal or kinetic SN feedback effective. Thacker & Couchman (2001); Stinson et al. (2006) developed a model to shut down cooling after the SN event to avoid overcooling and make thermal feedback more effective; this is known as the “delayed-cooling model”. Springel & Hernquist (2003) modeled galactic winds driven by SN feedback and stochastically chose gas particles to attain a constant wind velocity. These “wind particles” are briefly decoupled from hydrodynamical interactions to avoid their thermalization and subsequent radiative cooling. The advantage of this method is that it is easier to control the SN feedback effect by tuning the time to cut-off; the disadvantage is that it is unphysical.

The second method is to predict the outcome of kinetic SN feedback and inject the resultant energy and momentum into the simulation. Navarro & White (1993) developed a kinetic SN feedback model under the assumption that some fraction of the SN energy couples with the ISM as kinetic energy. The “mechanical feedback model” developed by Kimm & Cen (2014); Hopkins et al. (2018) estimate the terminal momentum of supernova remnant (SNR) using scaling relations obtained from high-resolution simulations (Chevalier 1974; Cioffi et al. 1988; Blondin et al. 1998) and inject momentum to neighboring fluid elements. Similar models were also developed for kpc-scale ISM simulations (Hennebelle & Iffrig 2014; Gatto et al. 2015; Kim & Ostriker 2017).

The galactic wind model by Springel & Hernquist (2003) could be considered as a combination of the “ignore” and “skip” methods as they skip wind acceleration and kick wind particles at a velocity consistent with observations. The advantage of this method depends on how one estimates the effect of SN feedback; the model can be realistic if the estimation is based on high-resolution numerical simulations, and can be helpful to study the baryon cycle if based on observational results. Its disadvantage, on the other hand, is that it necessitates a good estimator applicable to the wide spectrum of variations in the ISM environment, and we may miss some feedback processes by skipping the unresolved aspects of the physics.

The third method is to scale up the thermal energy of SN feedback to resolvable levels. Kay et al. (2003); Dalla Vecchia & Schaye (2012) developed a thermal feedback model that stochastically increases the temperature of neighboring fluid elements by a constant ΔT . The advantage offered by this method is that we can solve the growth of hot bubbles by thermal feedback using a hydro solver without any ad hoc treatments. However, its disadvantage is that while there remains the freedom of choosing ΔT , its physical interpretation of ΔT is insufficient.

The fourth method is to model the unresolved hot phase formed by thermal SN feedback. Yepes et al. (1997); Springel & Hernquist (2003) developed a two-phase ISM model considering thermal energy injection from SN feedback within the sub-resolution scale. Another two-phase ISM model is developed by Keller et al. (2014) who decomposed the hot and cold phases to store thermal energy injected from stellar particles in neighboring gas particles. The benefit of this method is that the two-phase model enables us to handle the hot phase, which is small in mass and otherwise challenging to resolve. It does, however, have the drawback of the simple two-phase model being unable to solve the kinetic effect of SN feedback on the sub-resolution scale.

Previous studies have compared different feedback models (Valentini et al. 2017; Rosdahl et al. 2017; Smith et al. 2018) and demonstrated that different models predict different galactic properties. In Shimizu et al. (2019, hereafter S19), we combined the kinetic feedback with the delayed-cooling model using the Sedov–Taylor self-similar solution. In the Fiducial model, 70% of the SN energy was injected as thermal energy, while 30% was as kinetic energy. We also temporarily shut off cooling for the neighboring gas particles after the thermal energy injection to increase the effectiveness of thermal feedback. While the “Osaka feedback model” by S19 succeeded in providing an understanding of the self-regulation of star

formation and naturally produced galactic outflow, it did contain some unphysical treatment, such as turning off cooling for the thermal feedback. For kinetic feedback, S19 injected the kinetic energy into scales larger than that of the radius at the Sedov–Taylor phase, which neglects radiative energy dissipation.

To build a good subgrid SN feedback model, we need to go back to the evolution of the single SNR and superbubble. The time evolution of the SNR and superbubble have been analytically and numerically investigated (e.g., Chevalier 1974; Weaver et al. 1977; Tomisaka & Ikeuchi 1986; Ostriker & McKee 1988; Martizzi et al. 2015; Kim & Ostriker 2015; Kim et al. 2017).

The SNR formed by a single SN explosion grows through four steps: 1) free expansion phase, 2) Sedov–Taylor phase, 3) pressure-driven snowplow phase, and 4) momentum-conserving snowplow phase. Amongst these four stages of evolution, about 77 % of the terminal momentum of SNR is acquired in the Sedov–Taylor phase (Kim & Ostriker 2015). Thus, the terminal momentum of the SNR is set by the duration of the Sedov–Taylor phase, i.e., its cooling time, which depends on the density and metallicity. Karpov et al. (2020) studied the effects of metallicity on the momentum of SNR using 1D simulation. They showed that terminal momentum saturates at low metallicities ($Z < 10^{-2} Z_{\odot}$), and that the power-law fit used in previous works (Thornton et al. 1998; Martizzi et al. 2015) overestimates the terminal momentum; this can be attributed to the contribution of metal-line cooling being smaller than that of hydrogen and helium recombination at low metallicities. They derived a three-parameter fitting function to the terminal momentum of SNR and demonstrated it to decrease the mass-loading by a factor of two over the power-law fit from 3D simulations of vertically stratified ISM patches.

In the case of the superbubble formed by multiple SNe, there are two classical theory of its time evolution after the adiabatic phase; pressure-driven and momentum-driven models (Appendix B). The pressure-driven model is applicable to the case where the gas inside the shell is overpressured with respect to the ambient medium, and the momentum-driven model otherwise. Since multiple SN explosions occur repeatedly, the thermodynamic state of the hot bubble fluctuates significantly, which makes it difficult to solve the time evolution of a superbubble with analytical methods (Dekel et al. 2019), necessitating a full numerical simulation.

Kim et al. (2017) performed 3D hydrodynamical simulations with the ATHENA code and found that superbubbles follow the momentum-driven model. They also found that the momentum per SN event is insensitive to

the ambient density, but more sensitive to the interval of SN explosions.

Studying the dynamics of a bubble created by stellar wind can also give significant insight for the evolution of an SN superbubble. Recently, the effect of thermal transfer due to mixing between the shell and its interior has been studied in the context of stellar wind bubbles by Lancaster et al. (2021a,b) using analytical and numerical methods. They showed that the bubbles cool efficiently due to mixing at the fractal interface of the hot bubble surface and that its growth is described by the momentum-driven model. Therefore, 1D simulations neglecting the mixing may overestimate the momentum as was shown by El-Badry et al. (2019) and Gentry et al. (2019) in the context of SN superbubbles. Fielding et al. (2020) have also studied turbulent, fractal mixing/cooling interfaces (Kelvin–Helmholtz instability) between hot and cold gas with resolved simulations.

In this study, we investigate the time evolution of the superbubble momentum via 3D hydrodynamical simulations with a focus on its dependence on metallicity, to supplement the results of Kim et al. (2017), who focused on its dependency on ISM density and time interval of SN explosions. Shell formation is delayed when the metallicity is small due to weaker metal-line cooling, which results in longer cooling times. Since the energy loss is negligible, the superbubble efficiently gains momentum in the adiabatic phase. Thus, one can expect the momentum input from a superbubble to the ISM to be more significant in a low-metallicity environment. Since the metal becomes more abundant during galaxy evolution, it is vital to study the effect of metallicity on SN feedback.

Recent zoom-in simulations of dwarf galaxies reach the pc-scale resolution and resolve the Sedov–Taylor phase of a single SNR (Kimm et al. 2015, 2016; Hu 2019; Agertz et al. 2020; Gutcke et al. 2021), and exascale computing systems are expected to enable star-by-star simulations up to the scale of the Milky Way galaxy within the next decade (Hirai et al. 2021). While subgrid SN feedback models become less necessary in high-resolution zoom-in simulations, there is a growing demand for large-scale cosmological simulations for large observational projects on $> 100 h^{-1} \text{Mpc}$ such as the Subaru Prime Focus Spectrograph (PFS, Takada et al. 2014), the Dark Energy Spectroscopic Instrument (DESI, Levi et al. 2013), the WEAVE (Dalton et al. 2012), the Euclid (Laureijs et al. 2011), and the Nancy Grace Roman Space Telescope (Spergel et al. 2015). Therefore, a better subgrid SN feedback model is still needed.

In this work, we use high-resolution simulation with ATHENA++ to investigate the momentum input from the superbubble and used it, along with previous high-resolution small-box simulations of SN-driven outflow, to develop an SN feedback model for the SPH cosmological simulation code GADGET3-OSAKA. Our strategy to develop a physically motivated model based on high-resolution numerical simulations is similar to the Simulating Multiscale Astrophysics to Understand Galaxies (SMAUG) project¹ (Kim et al. 2020a), where a galactic wind model of the multiphase outflow was developed with TIGRESS simulations (Kim et al. 2020b) and probability density functions of mass, momentum, energy, and metal loading were obtained in terms of the outflow velocity and sound speed. Our goal here is to develop a model of SN feedback from individual stellar particles, which can be applied in the future in both zoom-in and large-scale cosmological simulations for high-redshift galaxies that do not necessarily have fully-developed disks yet.

The structure of this paper is as follows. We discuss our superbubble simulation with Athena++ in Section 2, supplementing it with derivations of scaling relations for terminal momentum and radius of a superbubble shell for multiple SN explosions. We then construct our SN feedback model (both mechanical and thermal) in Section 3, and apply it to an isolated galaxy simulation in Section 4. We then compare our results with those of previous numerical works and discuss its caveats concerning its applications in cosmological simulations in Section 5. We then conclude in Section 6. In Appendix A we briefly review the analytic theory of single SNR and provide equations that are necessary for the formulation of our model, while in Appendix B, we review the analytic theory of a superbubble. Appendix C discusses the resolution requirement for thermal and kinetic feedback, as the final part, Appendix D, depicts the resolution test results of the SN feedback model in an isolated galaxy simulation.

2. SUPERBUBBLE SIMULATION WITH ATHENA++

In this section, we study the momentum input from the superbubble and its dependence on the ISM environment. We first use analytical calculations to study the dependence of the shell-formation time (i.e., when the adiabatic phase finishes and the cold, dense shell forms) on metallicity. Next, we perform high-resolution simu-

lations using ATHENA++ to investigate the time evolution of superbubbles. Finally, we derive fitting functions of typical momentum input by a superbubble per SN and a typical shock radius affected by the superbubble.

2.1. Analytic theory

When multiple SN explosions occur clustered in space and time in stellar clusters, superbubbles are formed with the shell-formation time being a critical timescale for their growth. In Section 2.1.1, we analytically calculate the shell-formation time and investigate its dependence on metallicity.

2.1.1. Shell-formation time

We first consider the shell-formation time of an SNR formed by a single SN and extend it to the case of a superbubble formed by multiple SNe.

Single SN—After SN explosion occurs, heated gas adiabatically expands and forms an SNR. The adiabatic phase is called the Sedov–Taylor phase, during which the SNR time evolution is described by Sedov–Taylor solutions. When the cooling effect is no longer negligible, the SNR can no longer be considered adiabatic, terminating the Sedov–Taylor phase.

SNR cooling is most effective at the shock front, where its density is its highest. The cooling time immediately after the shock wave is estimated to be

$$t_c = \frac{e}{de/dt} = \frac{n_t k_B T_{ST}}{(\gamma + 1) n_H n_e \Lambda(T_{ST})} = \frac{2.3}{1.2} \frac{k_B T_{ST}}{(\gamma + 1) n_H \Lambda(T_{ST})}, \quad (1)$$

where n_H , n_e , and n_t are the number densities of hydrogen, electrons, and total ions and electrons, respectively, while Λ represents the cooling function. Here, we assume the ratio of the number densities of hydrogen to helium atoms to be 10:1. T_{ST} is the temperature at the post-shock layer of the shock wave, obtained from the Sedov–Taylor solution and the Rankine–Hugoniot relation (Kim & Ostriker 2015, see also Appendix A):

$$T_{ST} = 5.3 \times 10^7 \text{ K } E_{51}^{2/5} n_0^{-2/5} t_3^{-6/5}, \quad (2)$$

where $E_{51} = E/(10^{51} \text{ erg})$, $n_0 = n_H/(1 \text{ cm}^{-3})$, $t_3 = t/(1 \text{ kyr})$ denote the energy injected by the SN explosion, the number density of hydrogen atoms in the ISM, and the time from the SN explosion.

Cooling via metal-line emission is most effective at $T \sim 10^5 \text{ K}$, and the cooling function at $10^5 \text{ K} < T < 10^7 \text{ K}$ is well-approximated as

$$\Lambda(T) = 10^{-22} \text{ erg cm}^3 \text{ s}^{-1} \Lambda_{6,-22} \left(\frac{T}{10^6 \text{ K}} \right)^{-0.7}, \quad (3)$$

¹ <https://www.simonsfoundation.org/flatiron/center-for-computational-astrophysics/galaxy-formation/smaug/>

where $\Lambda_{6,-22} = \Lambda(10^6 \text{ K})/(10^{-22} \text{ erg cm}^3 \text{ s}^{-1})$ depicts the value of the cooling function at $T = 10^6 \text{ K}$ (see Fig. 1). From equations (1), (2), and (3), the cooling time of the gas at the shock front at time t_s is

$$t_c(t_s) = 2.6 \times 10^7 \text{ yr} \left(\frac{t_s}{1 \text{ kyr}} \right)^{-2.04} E_{51}^{0.68} n_0^{-1.68} \Lambda_{6,-22}^{-1}. \quad (4)$$

Kim & Ostriker (2015) found that when the cooling time is set to $t_c = 0.6 e/(de/dt)$, the shell-formation time obtained from Eq. (6) is in good agreement with the numerical results (Kim et al. 2017).

The gas that is stirred up at time t_s cools down to form a low-temperature ($T < 10^5 \text{ K}$) dense shell at

$$t_{\text{sf}}(t_s) = t_s + t_c(t_s). \quad (5)$$

The shell-formation time is determined as the minimum value of $t_{\text{sf}}(t_s)$ following the method of Cox & Anderson (1982); Cox (1986):

$$t_{\text{sf}} = 4.5 \times 10^4 \text{ yr} E_{51}^{0.22} n_0^{-0.55} \Lambda_{6,-22}^{-0.33}. \quad (6)$$

Combining Eq. (6) with the Sedov–Taylor self-similar solution (Eq. A4), we obtain the radius, mass, and momentum at shell formation as:

$$R_{\text{sf}} = \xi_0 \left(\frac{E}{\rho} \right) t_{\text{sf}}^{2/5} = 23 \text{ pc} E_{51}^{0.29} n_0^{-0.42} \Lambda_{6,-22}^{-0.13}, \quad (7)$$

$$M_{\text{sf}} = \frac{4}{3} \pi R_{\text{sf}}^3 \rho = 1.8 \times 10^3 M_{\odot} E_{51}^{0.87} n_0^{-0.26} \Lambda_{6,-22}^{-0.39}, \quad (8)$$

$$\begin{aligned} p_{\text{sf}} &= 2.69 \frac{3}{4\pi} M_{\text{sf}} \dot{R}_{\text{sf}} \\ &= 2.2 \times 10^5 M_{\odot} \text{ km s}^{-1} E_{51}^{0.93} n_0^{-0.13} \Lambda_{6,-22}^{-0.19}, \end{aligned} \quad (9)$$

where the coefficient 2.69 is the value obtained when integrating the profiles of the Sedov–Taylor self-similar solution (see Eq. (16) of Kim & Ostriker 2015). The $\Lambda_{6,-22}$ value depends on metallicity. Since the cooling rate due to metal-line emission is proportional to the metal abundance, it proportionally varies with metallicity for a fixed metal abundance ratio. In this study, we use the cooling function of Sutherland & Dopita (1993). They assumed a solar abundance ratio (Anders & Grevesse 1989) for $\log(Z/Z_{\odot}) > 0.0$, and a primordial abundance ratio (Wheeler et al. 1989; Bessell et al. 1991) for $\log(Z/Z_{\odot}) \leq -1.0$, where $Z_{\odot} = 0.0194$ is the solar metallicity. Here, we fit the cooling function at $T = 10^6 \text{ K}$ as follows:

$$\Lambda_{6,-22}(Z) = \max \left(1.9 - 0.85 \frac{Z}{Z_{\odot}}, 1.05 \right) \frac{Z}{Z_{\odot}} + 10^{-1.33} \quad (10)$$

Combining Eqs. (6) and (10), we obtained the metallicity-dependent shell-formation time.

Multiple SNe—One can estimate the average time interval between the SN explosions in a stellar cluster by multiplying the stellar initial mass function with stellar age, which is approximately evenly spaced (Ferrand & Marcowith 2010). The temporal evolution of the superbubble can be thought of in the same way as that of an SNR formed by a single SN explosion, by assuming SN explosions to occur at regular time intervals with a continuous injection of energy.

The superbubble evolves adiabatically until the cooling effect manifests and a shell forms. Its time evolution is represented by a self-similar solution, where the dimensionless quantity ξ is a combination of the radius r , the energy released in a single SN explosion E_{SN} , the SN explosion interval Δt_{SN} , the density of the ISM ρ , and the time t :

$$\xi = \left(\frac{\rho}{E_{\text{SN}}/\Delta t_{\text{SN}}} \right)^{1/5} \frac{r}{t^{3/5}}. \quad (11)$$

Compared to the case of a single SN explosion, the energy E in the dimensionless quantity of the Sedov–Taylor solution (Eq. A4) is replaced by the energy injection rate $E/\Delta t_{\text{SN}}$, resulting in a difference in the time dependence from $t^{2/5}$ to $t^{3/5}$. The value of ξ at the shock is $\xi_0 = 0.88$, and the ratio of kinetic and thermal energies is $E_k : E_{\text{th}} = 22 : 78$ (Weaver et al. 1977).

The shell-formation time can be estimated by replacing the energy E in Eq. (6) with the total energy injected until time t , $E_{\text{SN}}(t/\Delta t_{\text{SN}})$, and solving for t :

$$t_{\text{sf,m}} = 1.7 \times 10^4 \text{ yr} E_{51}^{0.28} \Delta t_{\text{SN},6}^{-0.28} n_0^{-0.71} \Lambda_{6,-22}^{-0.42}. \quad (12)$$

The radius, velocity, mass, and momentum at this point in time are

$$R_{\text{sf,m}} = 5.3 \text{ pc} E_{51}^{0.37} \Delta t_{\text{SN},6}^{-0.37} n_0^{-0.63} \Lambda_{6,-22}^{-0.25}, \quad (13)$$

$$\begin{aligned} V_{\text{sf,m}} &= \\ &= 1.8 \times 10^2 \text{ km s}^{-1} E_{51}^{0.088} \Delta t_{\text{SN},6}^{-0.088} n_0^{0.084} \Lambda_{6,-22}^{0.17}, \end{aligned} \quad (14)$$

$$M_{\text{sf,m}} = 22 M_{\odot} E_{51}^{1.11} \Delta t_{\text{SN},6}^{-1.11} n_0^{-0.89} \Lambda_{6,-22}^{-0.75}, \quad (15)$$

$$\begin{aligned} p_{\text{sf,m}} &= \\ &= 3.3 \times 10^3 M_{\odot} \text{ km s}^{-1} E_{51}^{1.2} \Delta t_{\text{SN},6}^{-1.2} n_0^{-0.80} \Lambda_{6,-22}^{-0.59} \end{aligned} \quad (16)$$

We use Eqns. (12), (13), and (16) to normalize each physical quantity while examining the time evolution in Fig. 8 & 9.

2.2. Numerical Method

We carried out 3D hydrodynamical simulations with the ATHENA++ code² (Stone et al. 2020) with the

² <https://www.athena-astro.app>

second-order accurate van Leer time integrator, the HLLC solver, and second-order spatial reconstruction. We solved for the equations of continuity, momentum conservation, and energy while incorporating cooling, heating, and thermal conduction:

$$\frac{\partial \rho}{\partial t} + \nabla \cdot (\rho \mathbf{v}) = 0 \quad (17)$$

$$\frac{\partial(\rho \mathbf{v})}{\partial t} + \nabla \cdot (\rho \mathbf{v} \mathbf{v} + P) = 0 \quad (18)$$

$$\begin{aligned} \frac{\partial E}{\partial t} + \nabla \cdot \{ (E + P) \cdot \mathbf{v} \} \\ = \nabla \cdot (\kappa \nabla T) + n_{\text{H}} \Gamma(T) - n_{\text{H}}^2 \Lambda(T), \end{aligned} \quad (19)$$

where E is the energy density. We did not consider self-gravity and magnetic fields in our simulation. Assuming a mean molecular weight of $\mu = 1.4$, the gas temperature is taken at $T = P/(1.1n_{\text{H}}k_{\text{B}})$, where the hydrogen number density is $n_{\text{H}} = \rho/(1.4m_{\text{H}})$. We followed Kim & Ostriker (2015) for the implementation of radiative cooling and heating. For the cooling function $\Lambda(T)$ at low ($T < 10^4$ K) and high ($T > 10^4$ K) temperatures of gas, we adopted the fitting formulae from Koyama & Inutsuka (2002)³ and piecewise power-law fits to the cooling function of Sutherland & Dopita (1993) with collisional ionization equilibrium⁴, respectively, as shown in Fig. 1. Heating was applied, with the following heating function, only at $T < 10^4$ K to model the photoelectric heating of warm/cold ISM:

$$\Gamma(T) = \begin{cases} 10^{-26} \left(\frac{n_{\text{H}}}{1 \text{ cm}^{-3}} \right) \text{ erg s}^{-1} & (T < 10^4 \text{ K}) \quad (20a) \\ 0 \text{ erg s}^{-1} & (T > 10^4 \text{ K}). \quad (20b) \end{cases}$$

We used different cooling functions at $T > 10^4$ K for different metallicities, but we did not take into account the metallicity dependence at $T < 10^4$ K. We did not consider the metallicity dependence of the heating function. At $Z \ll 1$, the low-temperature cooling and heating rates would be quite different due to reduced photoelectric heating and cooling by fine-structure C and O lines when the metal abundance is low. However, these differences do not affect the results of our simulations, because the shell formation time is determined by the cooling time of shock-heated gas at high temperatures. We imposed a temperature floor of 10^3 K.

We followed El-Badry et al. (2019) to implement thermal conduction. For thermal conductivity κ at low

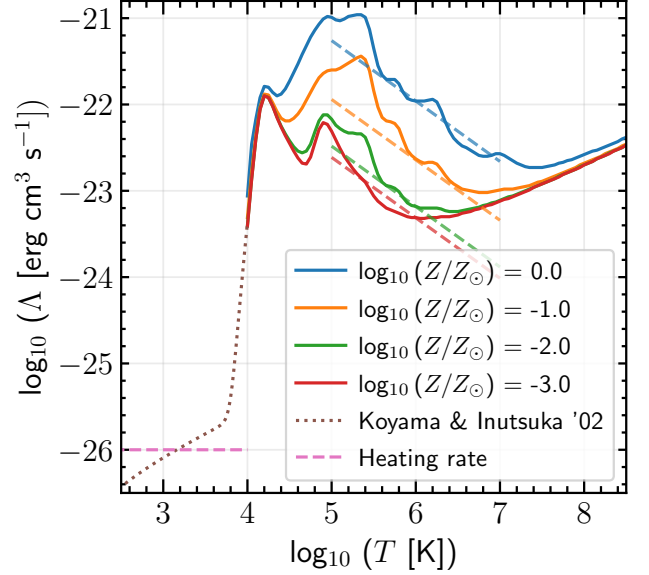


Figure 1. Cooling curves used in this work at different metallicities from Sutherland & Dopita (1993) combined with those of Koyama & Inutsuka (2002). The dashed colored lines show approximations given in Eq. (3) for the same metallicities given in the legend. The horizontal line indicates the constant photoelectric heating function $\Gamma = 1 \times 10^{-26} (n_{\text{H}}/1 \text{ cm}^{-3}) \text{ erg s}^{-1}$ at $T < 10^4$ K.

($T \leq 6.6 \times 10^4 \text{ K}$) and high ($T > 6.6 \times 10^4 \text{ K}$) temperatures of gas, we applied, respectively, the thermal conductivities due to the neutral atomic collision (Parker 1963):

$$\kappa = 2.5 \times 10^5 T_4^{1/2} \text{ erg s}^{-1} \text{ cm}^{-1} \text{ K}^{-1}, \quad (21)$$

where $T_4 = T/10^4 \text{ K}$, and hydrogen plasma (Spitzer 1962):

$$\kappa = \frac{1.7 \times 10^{11} T_7^{5/2}}{1 + 0.029 \ln(T_7 n_{e,-2}^{-1/2})} \text{ erg s}^{-1} \text{ cm}^{-1} \text{ K}^{-1}, \quad (22)$$

where $T_7 = T/10^7 \text{ K}$, $n_{e,-2} = n_e/10^{-2} \text{ cm}^{-3}$ and n_e denotes the electron number density. The conductive heat flux $q = \kappa \nabla T$ is limited by the energy flux that can actually be transported by the electrons $q_{\text{max}} = \frac{3}{2} \rho c_{\text{s,iso}}^3$ (Parker 1963; Cowie & McKee 1977). The effective thermal conductivity κ_{eff} , which includes the saturation resulting from limiting the heat flux, becomes

$$\kappa_{\text{eff}}^{-1} = \kappa^{-1} + \frac{|\nabla T|}{q_{\text{max}}}. \quad (23)$$

To save calculation time, we imposed a ceiling on the thermal conductivity at the following value:

$$\kappa_{\text{ceiling}} = 1.8 \times 10^{12} \left(\frac{n_{\text{H}}}{1 \text{ cm}^{-3}} \right) \text{ erg s}^{-1} \text{ cm}^{-1} \text{ K}^{-1}. \quad (24)$$

³ The cooling function given by Eq. (4) of Koyama & Inutsuka (2002) contains two typographical errors. See Eq. (4) of Vázquez-Semadeni et al. (2007) for the corrected functional form.

⁴ <https://www.mso.anu.edu.au/~ralph/data/cool/>

Table 1. Initial conditions of the ATHENA++ simulations.

Parameters	Their Values
Number density $n_{\text{H}} [\text{cm}^{-3}]$	0.1, 1, 10
Metallicity $Z [Z_{\odot}]$	$10^{-3}, 10^{-2}, 10^{-1}, 1$
Time interval of SN explosions $\Delta t_{\text{SN}} [\text{Myr}]$	0.01, 0.1, 1

This value is sufficiently high and has negligible effects on our results. We note that our resolution is not high enough to resolve the conductive interface.

We ran 36 simulations by varying the initial values of the parameters as listed in Table 1. The spatial resolution was fixed in time and uniform over the simulation box with periodic boundary conditions (we did not use static mesh refinement (SMR) or adaptive mesh refinement (AMR)). The spatial resolutions were $\Delta x = 6, 3,$ and 0.75 pc for number densities of $n_{\text{H}} = 0.1, 1,$ and 10 cm^{-3} , respectively, to satisfy the convergence condition by Kim & Ostriker (2015), $\Delta x < R_{\text{sf}}/10$. To set up a turbulent initial condition, we start from a uniform density field with pressure of $2.0 \times 10^3 (n_{\text{H}}/1 \text{ cm}^{-3}) k_{\text{B}} \text{ K cm}^{-3}$. We then generate the decaying turbulence with only initial forcing and evolve to 1 Myr. The initial forcing field was normalized to a Kolmogorov (1941) power spectrum $E(k) \propto k^{-5/3}$, while the range of driving was set to $2 \leq kL/2\pi \leq 20$. The velocity dispersion in the box was set to $\sigma = 5 \text{ km s}^{-1}$ adopted based on Larson’s law (Larson 1981; Ohlin et al. 2019). We note that this velocity dispersion of 5 km s^{-1} is lower than observed values at the scale of the simulation box, and that the initial evolution of 1 Myr is not long enough for multiphase ISM to develop via thermal instability. As a result, the inhomogeneity in the background is very weak, and the bubble expansion can be much more spherical than in realistic cases, which in turn affects the development of the Kelvin–Helmholtz instabilities that are normally driven by the shear at interfaces.

Thermal energy of 10^{51} erg per SN was injected into cells whose centers were at a distance $< r_{\text{init}}$ from the site of the SN explosion, where r_{init} is the radius within which the mass is $1 M_{\odot}$. When thermal energy was injected, a mass of $1 M_{\odot}$ was also simultaneously injected. We repeated this ten times, at intervals of Δt_{SN} , setting $t = 0$ at the time of the initial energy injection.

To study the time evolution of the physical quantities of the superbubble, we define the bubble radius R_{bub} as the largest radius which satisfies following two criteria: (i) $v_r > 3 \text{ km s}^{-1}$, and (ii) $t_{\text{dens}} < 4t_{\text{sc}}$, where v_r

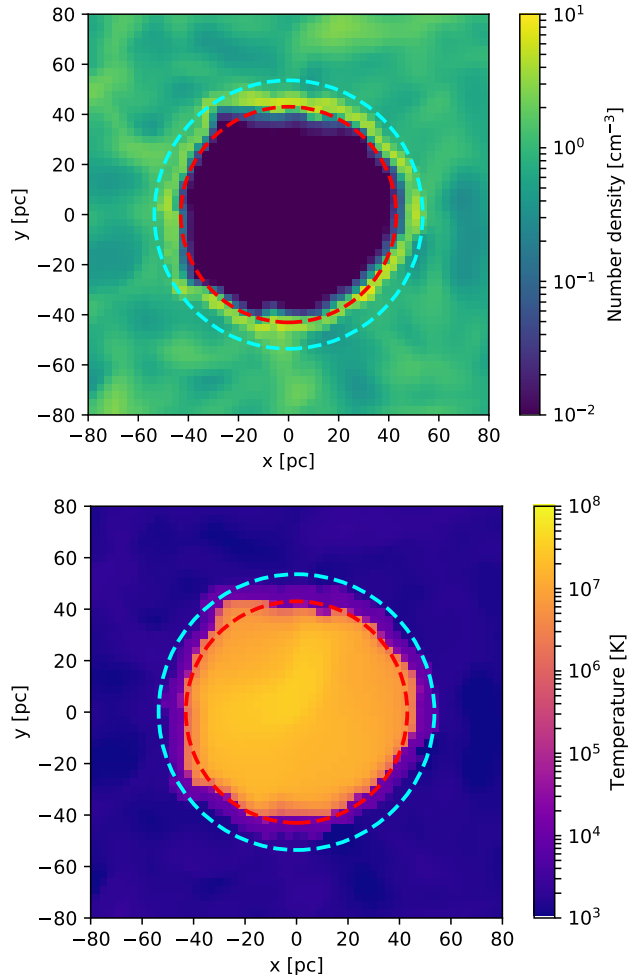


Figure 2. Slice plot of gas number density and temperature distribution at $t = 0.53 \text{ Myr}$ for the case of $n_{\text{H}} = 1 \text{ cm}^{-3}$, $Z = Z_{\odot}$, $\Delta t_{\text{SN}} = 0.1 \text{ Myr}$. The inner red circle shows R_{hot} , while the outer cyan circle shows R_{bub} .

is the radial velocity averaged over a spherical shell of radius r , $t_{\text{dens}} = \rho/\dot{\rho}$ indicates the timescale of the density change, and $t_{\text{sc}} = \Delta x/c_s$ depicts the sound-crossing time. In practice, we compute v_r , t_{dens} , and t_{sc} for each cell, draw averaged radial profiles of these quantities, and then apply the above criteria. We have described the time evolution of total mass, energy, and momentum within R_{bub} in Section 2.3.1.

To discuss the time evolution of the hot bubble, we also define the hot-gas radius as $R_{\text{hot}} = (V_{\text{hot}}/(4/3)\pi)^{1/3}$, where V_{hot} is the region at which $T > 10^4 \text{ K}$. The time evolution of R_{hot} is discussed in Section 2.4.

2.3. Results from Athena++ simulations

2.3.1. Results for $n_{\text{H}} = 1 \text{ cm}^{-3}$, $Z = 1 Z_{\odot}$, $\Delta t_{\text{SN}} = 0.1 \text{ Myr}$

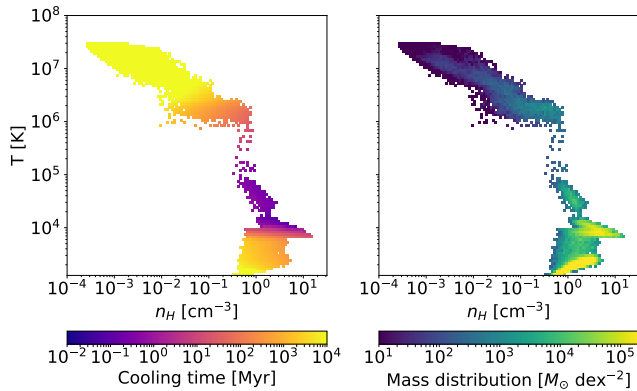


Figure 3. Phase diagram of gas in computational box, weighted for its cooling time (left panel) and mass (right panel), at the same time as in Fig. 2. In the left panel, one can see that the cooling time is short in the shell of $T \sim 10^4$ K and $n_{\text{H}} \sim 10 \text{ cm}^{-3}$.

Figure 2 shows a slice plot of density and temperature at 0.03 Myr after the fifth energy injection for the case of $n_{\text{H}} = 1 \text{ cm}^{-3}$, $Z = Z_{\odot}$, $\Delta t_{\text{SN}} = 0.1 \text{ Myr}$. The collected gas forms a low-temperature, high-density shell, inside which exists a high-temperature, low-density gas. The shell grows almost spherically, but with a slight distortion due to the density fluctuations caused by turbulence. We see that R_{hot} adequately captures the size of the hot bubble inside the shell, with R_{bub} enclosing the shell itself.

Figure 3 shows the phase diagram at this time. The low-temperature ($T < 2 \times 10^3 \text{ K}$) gas at the bottom right corner is the ISM gas. The gas swept up at front of the shell is heated by the shock, but as the temperature rises to $T > 10^4 \text{ K}$, it loses energy due to hydrogen recombination. Since the shock compresses the gas to a high density, its cooling time is shorter than the dynamical time, and a shell of $T \sim 10^4 \text{ K}$, $n_{\text{H}} \sim 10 \text{ cm}^{-3}$ is formed. At the post-shock layer of the shell, the gas can be heated by compression (if a shock propagates through the layer), or by mixing (if hot gas is advected into a cell containing cool gas), or by thermal conduction (if conduction is resolved). In our simulation, the upper left plume of hot gas in Figure 3 is heated by compression and thermal conduction.

Figure 4 shows the time evolution of the superbubble. The shell forms when it grows to a radius of about 20 pc, after which its growth slows down from the adiabatic phase. The subsequent energy injection stirs up the gas inside the shell and reduces its density. However, the density increases again due to the evaporation from the shell to the interior, and the mass is transferred from the cold shell to the hot interior.

2.3.2. Results for $\Delta t_{\text{SN}} = 0.01 \text{ Myr}$

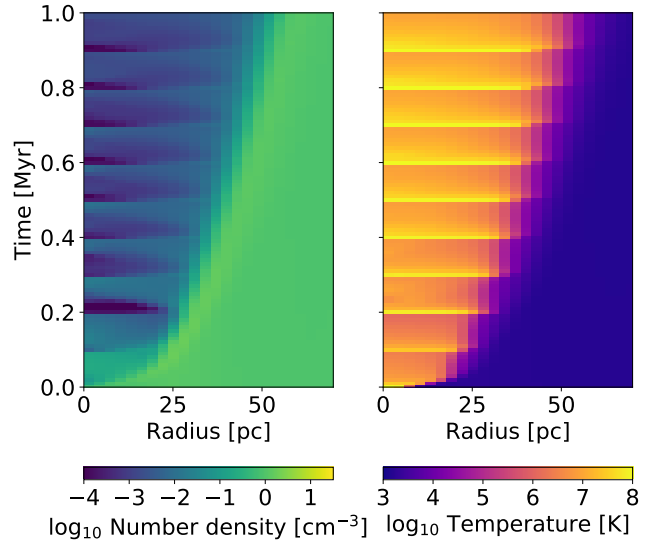


Figure 4. Evolution of superbubble as a function of radius, weighted for gas number density (left panel) and gas temperature (right panel), for the case of $n_{\text{H}} = 1 \text{ cm}^{-3}$, $Z = Z_{\odot}$, $\Delta t_{\text{SN}} = 0.1 \text{ Myr}$. One can see the power-law expansion of the hot bubble. The horizontal features indicate the intermittent SN injection.

The time evolution of mass, energy, and momentum for an SN explosion with a time interval of 0.01 Myr is shown in Figure 5.

For $n_{\text{H}} = 0.1 \text{ cm}^{-3}$, the system evolves adiabatically because the shell-formation time is longer than 0.1 Myr for any metallicity. Since the metallicity affects the shell-formation time but not the system's dynamics, no metallicity dependence is observed in this case. Since the system evolves adiabatically, its total energy after 10 SN explosions is 10^{52} erg . In the case of $n_{\text{H}} = 1 \text{ cm}^{-3}$, the cooling time is shorter due to the higher density, and this cooling effect is seen for $\log(Z/Z_{\odot}) = 0, -1$. The cooling effect is seen earlier for $\log(Z/Z_{\odot}) = 0$ because the larger the metallicity is, the shorter the cooling time is. Shell formation does not immediately get completed and, in the case of $\log(Z/Z_{\odot}) = 0$, the cooling effect begins to appear at $t \sim 0.04 \text{ Myr}$, while shell formation completes at $t \sim 0.1 \text{ Myr}$. During shell formation, the mass of the shell increases while that of the hot gas remains constant because it proceeds from the dense and short cooling time gas gathered in front of the superbubble.

In the case of $n_{\text{H}} = 10 \text{ cm}^{-3}$, the shell-formation time is shorter than 0.1 Myr at all metallicities, and a low-temperature, high-density shell is formed. After shell formation, most of the system's mass is in the shell, and at $t = 0.1 \text{ Myr}$, the mass of the hot gas is about 2% of the total. Comparing the cases of $\log(Z/Z_{\odot}) = -2.0, -3.0$, there is little difference in the time evolution of the

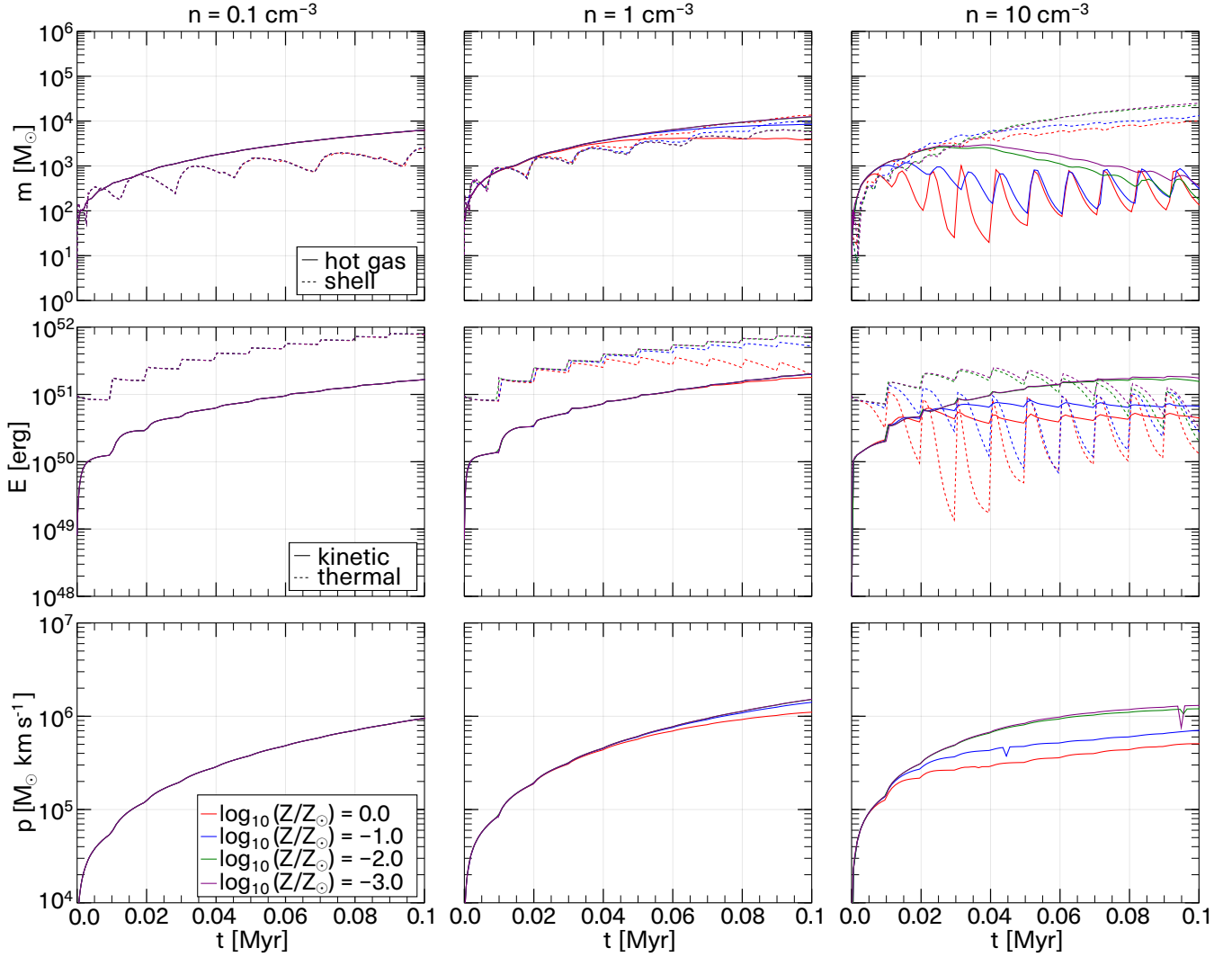


Figure 5. Time evolution of mass (top row), energy (middle row) and momentum (bottom row) of the superbubble for SN injection time intervals of $\Delta t_{\text{SN}} = 0.01$ Myr. For each component, we also show four different metallicities as indicated in the legend. Left column: $n_{\text{H}} = 0.1 \text{ cm}^{-3}$. Middle column: $n_{\text{H}} = 1 \text{ cm}^{-3}$. Right column: $n_{\text{H}} = 10 \text{ cm}^{-3}$. In the top panels for mass, the solid lines are for the hot gas inside the superbubble while dotted lines are for the shell. In the middle panels for energy, the solid lines are for kinetic energy while the dotted lines are for the thermal energy of superbubble gas including the shell. In the left column, the lines for the four metallicities overlap because of low density and long shell-formation time, which prolongs the adiabatic phase with little metal-cooling. In the right column, the effect of intermittent SN injection is visible.

physical quantities. In the low-metallicity environment, bremsstrahlung is a more dominant cooling mechanism than metal line emission at $T > 10^6$ K, and hence the difference in metallicity becomes less apparent.

2.3.3. Results for $\Delta t_{\text{SN}} = 0.1$ Myr

The time evolution of mass, energy, and momentum of a superbubble in the cases of $\Delta t_{\text{SN}} = 0.1$ Myr is shown in Fig. 6. In this case, the shell-formation time is shorter due to the lower energy injection rate than $\Delta t_{\text{SN}} = 0.01$ Myr.

In cases of $n_{\text{H}} = 0.1 \text{ cm}^{-3}$ and $\log(Z/Z_{\odot}) = 0.0, -1.0$, the shell formation is completed within the simulation

time, after which the kinetic energy becomes roughly constant as shown by the red solid line in the left middle panel of the Fig. 6.

In cases of $n_{\text{H}} = 1 \text{ cm}^{-3}$, the shell formation completes before the second SN explosion. Each SN explosion injects 10^{51} erg of thermal energy; some of it is converted to kinetic energy by PdV work on the shell, and the rest is dissipated by cooling so that most of the thermal energy is lost within 0.1 Myr following energy injection. From the phase diagram at $t = 0.53$ Myr for $\log(Z/Z_{\odot}) = 0.0$ (Fig. 3), the cooling time of the gas inside the shell is longer than 1 Myr. However, heat is transported to the shell by gas mixing at its rear surface

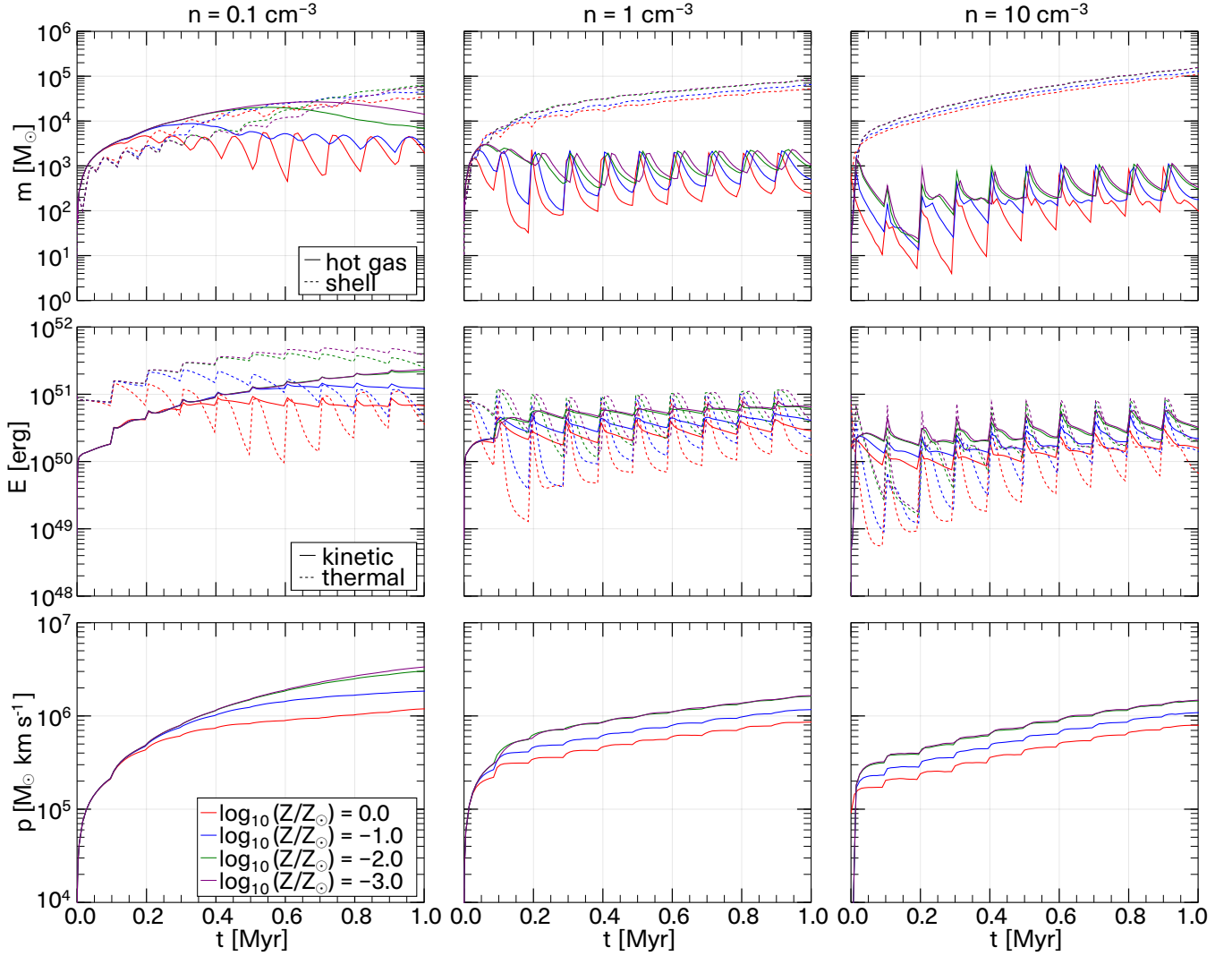


Figure 6. Same as Figure 5, but for SN injection time interval $\Delta t_{\text{SN}} = 0.1$ Myr. Note that the time range in the abscissa is different from that in Figure 5.

and then radiated away (El-Badry et al. 2019; Fielding et al. 2020; Lancaster et al. 2021a,b), resulting in the loss of thermal energy within a duration shorter than 1 Myr. We note that our resolution is not high enough to resolve the conductive interfaces, and some of the thermal energy could be lost due to numerical diffusion. As shown in the top middle panel of Fig. 6, the shell grows in mass while conserving momentum after each SN injection. At the same time, the kinetic energy decreases as shown in the central panel of Fig. 6.

2.3.4. Results for $\Delta t_{\text{SN}} = 1$ Myr

The time evolution of superbubble mass, energy, and momentum in the case of $\Delta t_{\text{SN}} = 1$ Myr is shown in Fig. 7. In this case, the shell is formed before the second SN explosion occurs in all cases; therefore the time evolution is similar to that for $\Delta t_{\text{SN}} = 0.1$ Myr, $n_{\text{H}} =$

1, 10 cm^{-3} . At $t > 4$ Myr, thermal energy exceeds kinetic energy. At this time, most of the mass is in the shell with its interior being cooled. Therefore, the gas in the shell contains most of the thermal energy of the superbubble. As shell mass increases while conserving momentum, its kinetic energy decreases. Let the velocity, temperature, and density of the shell be v_{shell} , T_{shell} , and ρ_{shell} , respectively. When the kinetic energy decreases to $(1/2)\rho_{\text{shell}}v_{\text{shell}}^2 < (3/2)(\rho_{\text{shell}}/\mu m_{\text{H}})k_{\text{B}}T_{\text{shell}}$, the thermal energy becomes larger. If the temperature of the shell is around the ISM temperature $T_{\text{ISM}} \sim 2 \times 10^3$ K, then the thermal energy exceeds kinetic energy when $v_{\text{shell}} < 7 \text{ km s}^{-1}$. When $n_{\text{H}} = 10 \text{ cm}^{-3}$, the mass and momentum appear to be decreasing when t is large. This is because the shell velocity has fallen below 3 km s^{-1} , whereby we can no longer follow its time evolution. In

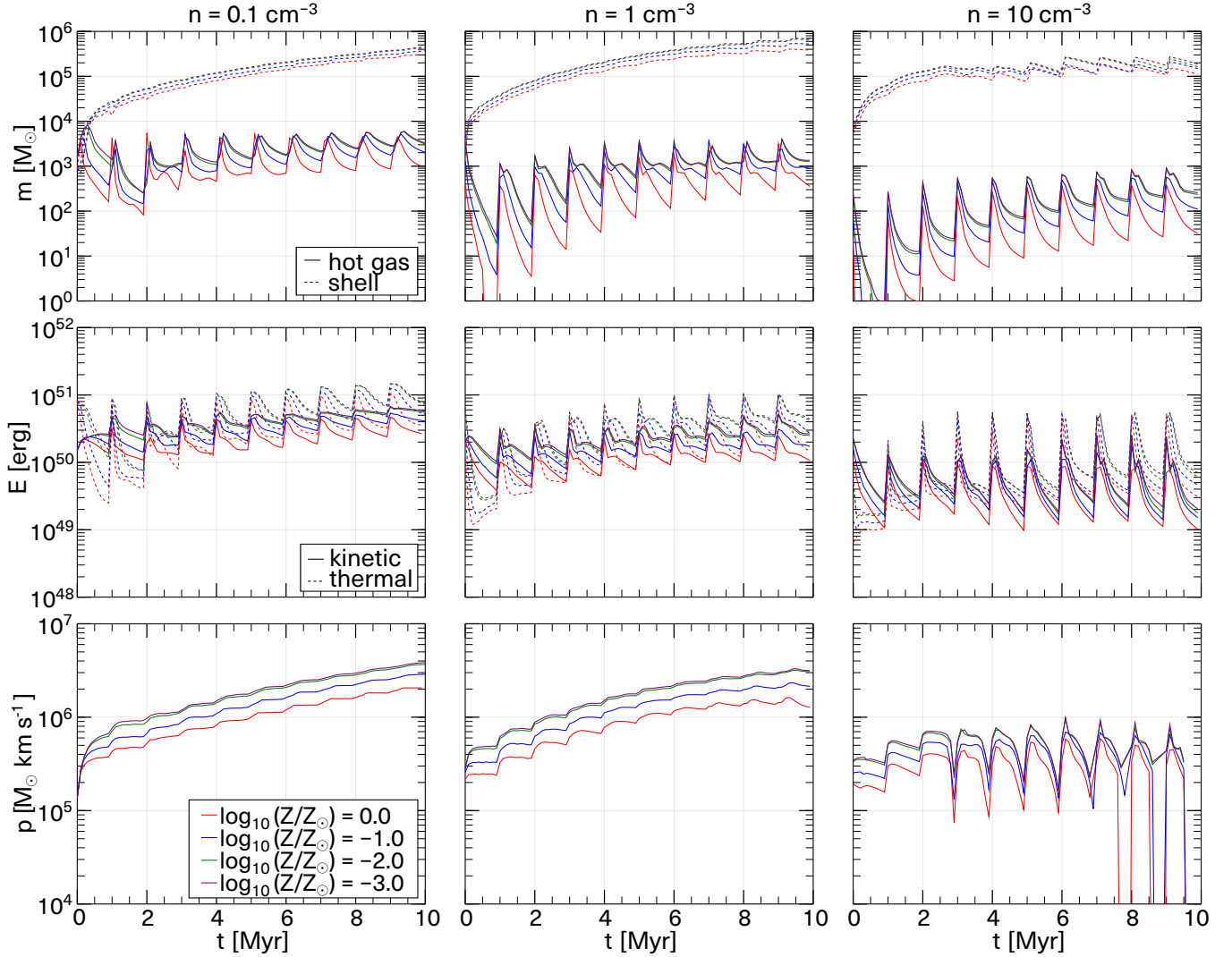


Figure 7. Same as Figure 5, but for SN injection time interval $\Delta t_{\text{SN}} = 1$ Myr. Note that the time range in the abscissa is different from that in Figure 5.

such a case, the shell is expected to gradually mix with the ISM.

2.4. Application to SN feedback model in galaxy simulations

In this section, we derive the scaling relations for the time evolution of superbubble momentum and radius for the application to the SN feedback model in galaxy simulations.

To discuss the environmental dependence of the superbubble in a unified manner, we normalize each physical quantity by its value at the shell-formation time. The same was done for single SN explosion simulations by Kim & Ostriker (2015), and also by Kim et al. (2017) for only the time variable for multiple SN explosion simulations.

Figure 8 shows the time evolution of the radius, normalized by its value at the shell-formation time. The time evolution of the radius shows some deviations, but in all cases, we can see that the radius evolves according to

$$\frac{R_{\text{hot}}}{R_{\text{sf,m}}} = \left(\frac{t}{t_{\text{sf,m}}} \right)^{0.5}, \quad (25)$$

as was also found by Kim et al. (2017). When $t < t_{\text{sf,m}}$, the superbubble is in an adiabatic period and expected to evolve with $R \propto t^{3/5}$ (Eq. 11). The good fit of the straight line with a slope of 0.5 can be attributed to the fact that the energy injection is discrete rather than continuous, resulting in an intermediate time evolution with the Sedov–Taylor solution $R \propto t^{2/5}$ (Eq. A4). The asymptote of the fitting line is due to the transition from the Sedov–Taylor solution to the adiabatic solution of the superbubble. Time evolution after shell-formation

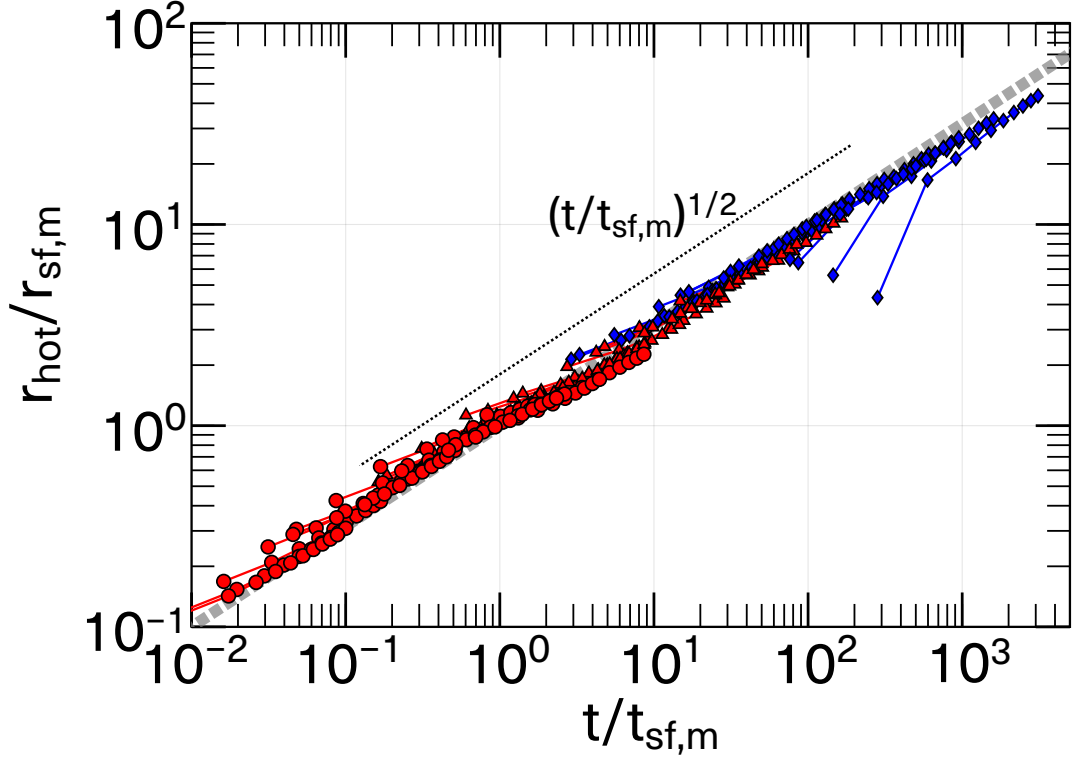


Figure 8. Evolution of R_{hot} normalized by $R_{\text{sf,m}}$, versus time normalized by $t_{\text{sf,m}}$. Red and blue points depict the runs with $\Delta t_{\text{SN}} < 0.1 t_{\text{PDS}}$ and $\Delta t_{\text{SN}} > 0.1 t_{\text{PDS}}$, respectively. Different symbols connected by line correspond to runs at different SN intervals: $\Delta t_{\text{SN}} = 0.01 \text{ Myr}$ (circle), $\Delta t_{\text{SN}} = 0.1 \text{ Myr}$ (triangle), $\Delta t_{\text{SN}} = 1 \text{ Myr}$ (diamond). The thick black dotted line shows the power-law of Eq. (25).

can also be approximated by a straight line with a slope of 0.5. The asymptotic behavior of the blue lines from the bottom is because the hot-gas radius R_{hot} could not correctly follow the radius of the inside of the shell when it was cooled down to $T < 2 \times 10^4 \text{ K}$. The scaling relation $R \propto t^{1/2}$ agrees with the prediction from the momentum-driven model and not with that from the pressure-driven model (Appendix B). Substituting the values of $R_{\text{sf,m}}$, $t_{\text{sf,m}}$ (Eqs. (13), (12)), the time evolution of radius and velocity are obtained as

$$R = 40 \text{ pc } t_6^{1/2} E_{51}^{0.23} \Delta t_{\text{SN},6}^{-0.23} n_0^{-0.28} \Lambda_{6,-22}^{-0.040}, \quad (26)$$

$$V = 20 \text{ km s}^{-1} t_6^{-1/2} E_{51}^{0.23} \Delta t_{\text{SN},6}^{-0.23} n_0^{-0.28} \Lambda_{6,-22}^{-0.040} \quad (27)$$

Next, we show the time evolution of momentum in Figure 9. It shows two different trends after the shell-formation time. If the interval between SN explosions is longer than the duration of the pressure-driven snowplow (PDS) phase of a single SN explosion, t_{PDS} (Eq. A15), energy injection is considered to be discrete and the superbubble is expected to display an evolution over time that is different from the continuous case. Since thermal transfer to the shell was not considered in the derivation of t_{PDS} , the actual duration of the PDS phase will be shorter than t_{PDS} .

Here we find that the following fitting functions can describe the two separate regimes continuously as shown in Fig. 9:

$$\frac{p}{p_{\text{sf,m}}} = \begin{cases} \tau^{7/5} & (t < t_{\text{sf,m}}) \\ \frac{1}{2} (\tau + \tau^{-1/5}) & (t > t_{\text{sf,m}} \ \& \ \frac{\Delta t_{\text{SN}}}{t_{\text{PDS}}} < 0.1) \\ \tau & (t > t_{\text{sf,m}} \ \& \ \frac{\Delta t_{\text{SN}}}{t_{\text{PDS}}} > 0.1), \end{cases} \quad (28a) \quad (28b) \quad (28c)$$

where $\tau = t/t_{\text{sf,m}}$. Since the momentum can be estimated as $p = (4/3)\pi R^3 \rho \dot{R}$, when the time evolution of the radius is expressed as $R \propto t^\alpha$, $p \propto t^{4\alpha-1}$. Before shell formation, the superbubble grows adiabatically, and the time evolution of its radius is $R \propto t^{3/5}$; thus, the time evolution of momentum is $p \propto t^{7/5}$.

When $t \gg t_{\text{sf,m}}$, there occurs a deviation from the fitting line. This was also seen when $\Delta t_{\text{SN}} = 1 \text{ Myr}$, $n_{\text{H}} = 10 \text{ cm}^{-3}$ (Fig. 7), because the shell velocity dropped below 3 km s^{-1} and its time evolution could not be followed.

In passing, we note that El-Badry et al. (2019) derived a criterion to distinguish discrete energy injection versus continuous limit in their Eq. (53). They derived this criteria only by considering the blast waves from individual SNe before reaching the shell, and their simulation

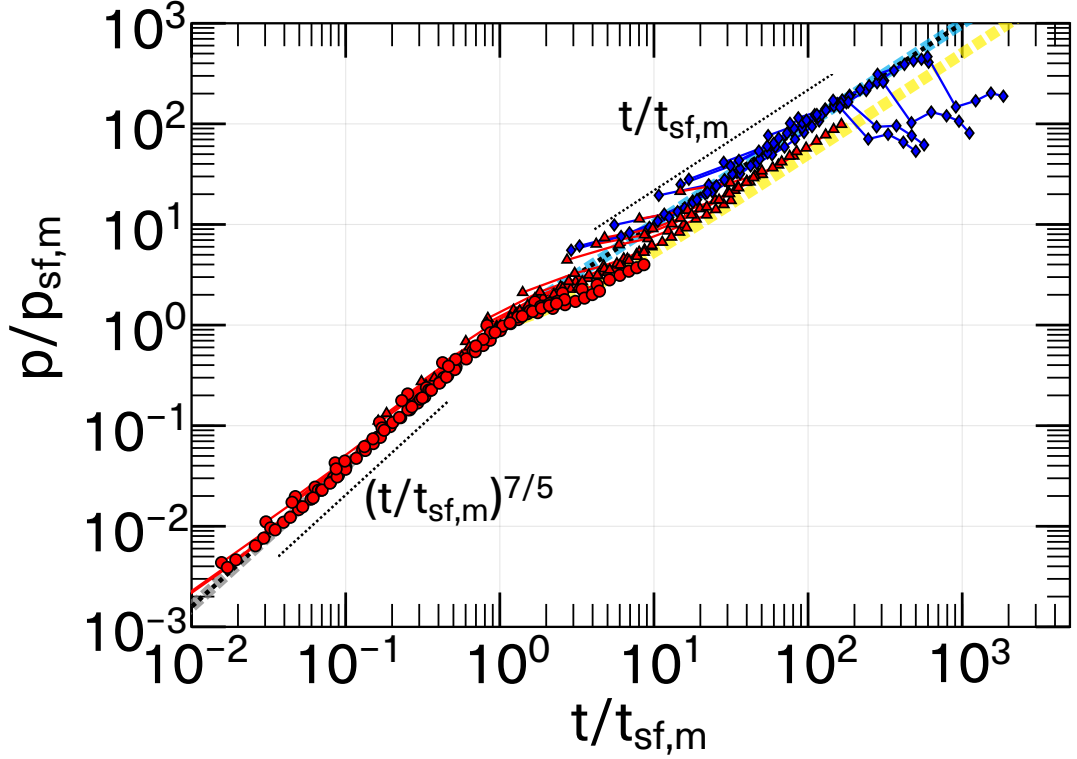


Figure 9. Evolution of momentum p normalized by $p_{\text{sf},m}$, versus time normalized by $t_{\text{sf},m}$. Red and blue points depict the runs with $\Delta t_{\text{SN}} < 0.1 t_{\text{PDS}}$ and $\Delta t_{\text{SN}} > 0.1 t_{\text{PDS}}$, respectively. Different symbols connected by line correspond to runs at different SN intervals: $\Delta t_{\text{SN}} = 0.01$ Myr (circle), $\Delta t_{\text{SN}} = 0.1$ Myr (triangle), $\Delta t_{\text{SN}} = 1$ Myr (diamond). The black dotted lines indicate the $(p/p_{\text{sf},m}) \propto (t/t_{\text{sf},m})^{7/5}$ and $(p/p_{\text{sf},m}) \propto (t/t_{\text{sf},m})$ power-law, respectively. The thick gray, yellow and cyan dotted lines indicate the fitting functions of Eq. (28a), (28b), and (28c), respectively.

results asymptote to their modified energy-driven solution with cooling at $t > t_{\text{subsonic}}$. We only simulated ten SN explosions, while El-Badry et al. (2019) examined the evolution all the way to the continuous energy injection limit (although with 1-D simulation); therefore our time-scale shown in Fig. 9 is somewhat of shorter time range than that of El-Badry et al. (2019)’s work (see their Fig. 6). The subsonic timescale t_{subsonic} in Eq. (53) of El-Badry et al. (2019) is much longer than our t_{PDS} , and therefore it is not straightforward to compare our results using their criteria based on t_{subsonic} .

3. CONSTRUCTION OF SN FEEDBACK MODEL

In this section, we describe the construction of our SN feedback model for galaxy simulations. Here we assume using the model in SPH simulation. Our model is based on the results from the previous section and on existing works on high-resolution small-box simulations.

3.1. Averaged momentum per SN for a stellar population

From the fitting function in Sec. 2.4, we derive the expression for momentum of a superbubble per SN, averaged over an initial stellar cluster mass function (ICMF).

We assume the ICMF to be described by the power-law $dN/dM_c \propto M_c^{-2}$ with high-mass cutoff, where M_c is the mass of the stellar cluster (Krumholz et al. 2019) and stellar initial mass function (IMF) is fixed. We also assume SNe occurs at a constant rate. The ICMF can be translated to an SN number function (probability distribution function of the number of SN explosions occurring in a stellar cluster)

$$\frac{dN}{dN_{\text{SN}}} = AN_{\text{SN}}^{-2}, \quad (29)$$

where N_{SN} is the number of SN explosions occurring in a stellar cluster and A is the normalization factor. The range of the number of SN explosions is assumed as $N_{\text{SN}} = N_{\text{SN},\text{min}} - N_{\text{SN},\text{max}}$, where we adopt the range of $(N_{\text{SN},\text{min}}, N_{\text{SN},\text{max}}) = (1, 500)$, and the normalization factor is $A = 1/\ln 500$. The value of $N_{\text{SN},\text{max}} = 500$ is the number of SN explosions expected to happen in the largest young massive star clusters (YMCs) in the Milky way with a mass of $M = 5 \times 10^4 M_{\odot}$ (Portegies Zwart et al. 2010). The choice of high-mass cutoff has little effect on the result since such high-mass YMCs are rare objects. The SNe interval is obtained

by dividing their duration by their number, $\Delta t_{\text{SN}} = (t_{\text{SN,end}} - t_{\text{SN,start}})/N_{\text{SN}}$, where $t_{\text{SN,start}}$, $t_{\text{SN,end}}$ are the times at the first and the last Type II SN after the formation of the stellar cluster, i.e., the minimum and the maximum lifetimes of stars causes Type II SNe. The lifetimes of stars depend on their mass and metallicity. We calculate SNe duration using CELIB⁵ (Saitoh 2017), which compute it using the metallicity-dependent stellar lifetime table by Portinari et al. (1998). We assume the mass range of the progenitors of Type II SNe to be 13–40 M_{\odot} . In the range of $Z = 10^{-6}$ – 10^{-2} , SNe duration is

$$t_{\text{SN,end}} - t_{\text{SN,start}} \sim 1.2 \times 10^7 \text{ yr}. \quad (30)$$

Single SN explosion energy is set to 10^{51} erg. The averaged momentum per SN is

$$\hat{p}(n_0, Z) = \int_{N_{\text{SN,min}}}^{N_{\text{SN,max}}} p(n_0, Z, \Delta t_{\text{SN}}(N'_{\text{SN}})) \frac{dN}{dN'_{\text{SN}}} dN'_{\text{SN}}. \quad (31)$$

The final integral is well-fitted by the following function:

$$\hat{p}(n_0, Z) = 1.75 \times 10^5 M_{\odot} \text{ km s}^{-1} n_0^{-0.05} \Lambda_{6,-22}^{-0.17}, \quad (32)$$

and the momentum input by \mathcal{N}_{SN} SNe (superbubble momentum, p_{SB}) is estimated as

$$p_{\text{SB}}(\mathcal{N}_{\text{SN}}, n_0, Z) = \mathcal{N}_{\text{SN}} \hat{p}(n_0, Z). \quad (33)$$

Here we used a slightly different font of \mathcal{N}_{SN} for the total number of SNe for a star particle in the simulation (i.e., a collection of stellar clusters, rather than a population of stars in a single stellar cluster).

3.2. Shock radius for a star particle

We similarly calculate the shock radius of SN feedback of a star particle. Assuming that stellar clusters follow the power-law ICMF, we determine the shock radius of the SN feedback as the radius of a sphere whose volume is the sum of those of the superbubbles. We first consider the averaged volume shocked by SN feedback *per SN* considering the variation of superbubbles created by a range of star clusters:

$$\hat{V}(n_0, Z) = \int_{N_{\text{SN,min}}}^{N_{\text{SN,max}}} \frac{4}{3} \pi R(n_0, Z, \Delta t_{\text{SN}}(N'_{\text{SN}}))^3 \frac{dN}{dN'_{\text{SN}}} dN'_{\text{SN}}. \quad (34)$$

Then the effective radius is obtained as

$$\hat{R}(n_0, Z) = \left(\frac{3\hat{V}}{4\pi} \right)^{1/3} = 61 \text{ pc } n_0^{-0.22} \Lambda_{6,-22}^{-0.04}, \quad (35)$$

⁵ <https://bitbucket.org/tsaitoh/ceelib>

and the shock radius by \mathcal{N}_{SN} SNe is calculated as

$$R(\mathcal{N}_{\text{SN}}, n_0, Z) = \mathcal{N}_{\text{SN}}^{1/3} \hat{R}(n_0, Z). \quad (36)$$

Here, \mathcal{N}_{SN} is meant to be the number of SNe occurring in the stellar population of a star particle. Since Eq. (34) gives the averaged superbubble volume *per SN*, the effective volume for \mathcal{N}_{SN} SNe for a star particle would be $\mathcal{N}_{\text{SN}} \hat{V}$ and the effective radius would be $\mathcal{N}_{\text{SN}}^{1/3} \hat{R}$ as given in Eq. (36).

Another way to determine the shock radius is to use the radius of a single superbubble described in Eq. (26) at

$$t = N_{\text{SN}} \Delta t_{\text{SN}}, \quad (37)$$

assuming that the percolated superbubbles from multiple star clusters can be approximated well as a single superbubble. Then, inserting Eq. (37) into Eq. (26) and using Eq. (30) with $E_{51} = 1$ yields the shock radius

$$R'(\mathcal{N}_{\text{SN}}, n_0, Z) = 78 \text{ pc } \mathcal{N}_{\text{SN}}^{0.23} n_0^{-0.28} \Lambda_{6,-22}^{-0.04}(Z). \quad (38)$$

Similarly to the above, one can interpret Eq. (36) as the shock radius of a single superbubble formed by \mathcal{N}_{SN} SNe at the age of $t = 4.8 \text{ Myr } \mathcal{N}_{\text{SN}}^{0.38} n_0^{0.22}$, which can be obtained by equating Eq. (26) and (36). In other words, the above two different methods of computing the effective shock radius can be interpreted as single superbubble radius at different times.

In the following, we use Eq. (36) together with Eq. (10) and Eq. (33) for our SN feedback model described in the next section, but the choice of either Eq. (36) or (38) is unlikely to affect our final results.

3.3. Spherical superbubble model

A schematic description of the ‘Spherical superbubble model’ developed in this paper is illustrated in Fig. 10. When the SN event occurs, we first calculate the density and metallicity at the SN site. An iterative solver is used to find a smoothing length for the stellar particle that satisfies

$$h_{\text{sml},i} = \left(\frac{3N_{\text{ngb}}}{4\pi \sum_j W(r_{ij}, h_{\text{sml},i})} \right)^{1/3}, \quad (39)$$

where r_{ij} is the distance from the i -th stellar particle to the j -th gas particle, N_{ngb} is the number of neighboring SPH particles, and W is the kernel function adopted in the SPH simulation. We then compute the shock radius R_{shock} using local density and metallicity, using equation (36). We search for the gas particles within the shock radius and project them from the position of the star onto a sphere centered at the star with radius R_{shock} . Then,

we construct a Voronoi polyhedron using STRIPACK⁶ (Renka 1997), which is an algorithm that constructs a Voronoi diagram of a set of points on the surface of a sphere. After constructing the Voronoi polyhedron on the spherical surface, we calculate Ω , which is the solid angle of the corresponding face on the Voronoi polyhedron from the star. We distribute physical quantities from the SN to neighboring gas particles weighted by Ω . The mass and metal deposited on the i -th gas particle are

$$\Delta m_i = m_{\text{SN}} \left(\frac{\Omega_i}{4\pi} \right), \quad (40)$$

$$\Delta m_{Z,i} = m_{Z,\text{SN}} \left(\frac{\Omega_i}{4\pi} \right), \quad (41)$$

where m_{SN} and $m_{Z,\text{SN}}$ are the mass and metal inputs from feedback and Ω_i is the solid angle of the corresponding face on the Voronoi polyhedron from the star. If the number of gas particles inside the shock radius is less than four, the Voronoi polyhedron cannot be constructed. In that case, we search for at least two nearest gas particles and equally assign mass and metals to them. Note that our method is similar to, but different in detail from, that of Hopkins et al. (2018).

3.4. Mechanical feedback

Using the superbubble momentum p_{SB} computed in Eq. (33), we deposit the following momentum on the i -th gas particle:

$$\Delta \mathbf{p}_i = p_{\text{SB}} \frac{\Omega_i}{4\pi} \mathbf{n}_i, \quad (42)$$

where \mathbf{n}_i is the normal vector of the face on the Voronoi polyhedron. When the number of neighboring gas particles falls below four (which prevents the construction of a Voronoi polyhedron), we inject the same amount of momentum and determine \mathbf{n}_i so that the total momentum is conserved. The total momentum of the surrounding gas should be conserved before and after the SN event. For this, we compute the total momentum input as:

$$\Delta \mathbf{p}_{\text{tot}} = \sum_i \Delta \mathbf{p}_i, \quad (43)$$

and modify momentum input to i -th gas particle to

$$\Delta \mathbf{p}'_i = \Delta \mathbf{p}_i - \frac{\Omega_i}{4\pi} \Delta \mathbf{p}_{\text{tot}}. \quad (44)$$

The kinetic energy input by momentum kick may exceed the SN energy input due to particle distribution.

Thus, we limit the momentum input to each neighboring particle based on the Sedov–Taylor solution. The resulting momentum input is:

$$\Delta \mathbf{p}''_i = \frac{\Delta \mathbf{p}'_i}{|\Delta \mathbf{p}'_i|} \min \left(|\Delta \mathbf{p}'_i|, \sqrt{2(m_i + \Delta m_i) \Delta E_{\text{kin},i}} \right), \quad (45)$$

where m_i is the mass of the i -th gas particle and $\Delta E_{\text{kin},i}$ is the solid-angle-weighted kinetic energy from SN feedback. $\Delta E_{\text{kin},i}$ is given as

$$\Delta E_{\text{kin},i} = \epsilon_{\text{kin}} E_{\text{SN}} \frac{\Omega_i}{4\pi}, \quad (46)$$

where ϵ_{kin} is a fraction of the SN energy deposited as kinetic energy, and we adopt $\epsilon_{\text{kin}} = 0.3$ as the default value (S19). Equation (45) essentially corresponds to equation (A1) in Kimm & Cen (2014) and equation (32) in Hopkins et al. (2018).

The momentum input above is calculated with respect to the frame moving with the star particle. To ensure exact conservation, we require a term accounting for the relative motion between the gas and the star (Hopkins et al. 2018). Finally, the momentum input boosted back to the simulation frame is

$$\Delta \mathbf{p}'''_i = \Delta \mathbf{p}''_i + \Delta m_i \mathbf{v}_{\text{star}}, \quad (47)$$

where \mathbf{v}_{star} is the star velocity.

In summary, we first compute $\Delta \mathbf{p}_i$ for the momentum that we want to assign the neighboring gas particles with. Then $\Delta \mathbf{p}'_i$ makes it isotropic and we ensure energy conservation by $\Delta \mathbf{p}''_i$. Finally, $\Delta \mathbf{p}'''_i$ takes care of the motion of the originating stellar particle. By giving $\Delta \mathbf{p}'''_i$, the momentum feedback is basically guaranteed to be isotropic, energy-conserving, and momentum-conserving.

To be more specific, it is possible that momentum conservation could be broken when the second term in the RHS of Eq. (45) is chosen. However, such a situation does not arise very often because we do not have sufficient to resolve the Sedov–Taylor phase. In fact, we have checked our isolated galaxy simulations performed in Section 4, the second term was chosen only $3.4 \times 10^{-5} \%$ of the cases for the Fiducial run, and $1.1 \times 10^{-4} \%$ for the High-reso run.

3.5. Thermal feedback

Several groups have studied the SN-driven outflow using high-resolution small-box simulations. Hu (2019) investigated SN-driven outflow of a dwarf galaxy. They showed the entropy $S \equiv k_{\text{B}} T n^{1-\gamma}$ of the hot outflow to be $10^8 - 10^9 k_{\text{B}} \text{K cm}^2$, and it is almost constant after being launched from the galaxy. Although their result

⁶ https://people.sc.fsu.edu/~jburkardt/f_src/stripack/stripack.html

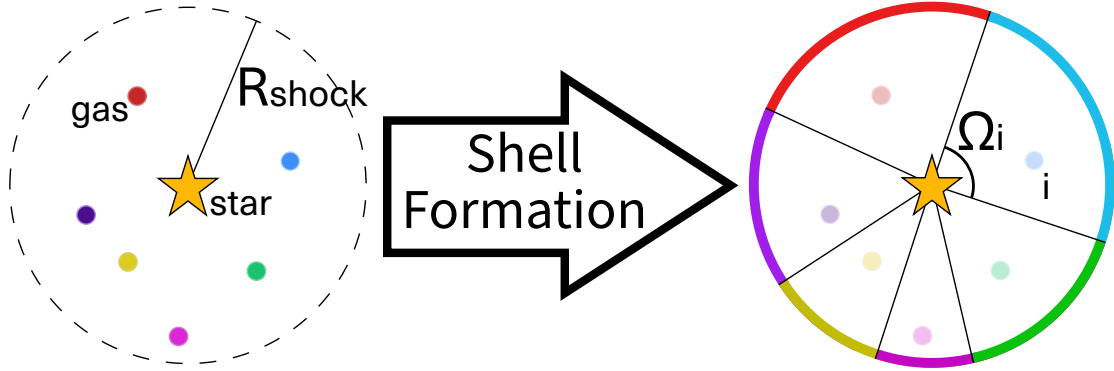


Figure 10. Schematic description of the spherical superbubble feedback model developed in this paper. The left hand side shows the particle distribution of gas and star particles when the supernova explosions begin, whereas the right hand side shows the superbubble shell formation, and how we split the shell using Voronoi tessellation based on the gas particle distribution inside the bubble.

is on a dwarf galaxy, the energy loading factor and specific energy of the hot outflow by Hu (2019) are similar to those of a Milky-way-mass galaxy (Li et al. 2017; Armillotta et al. 2019; Kim & Ostriker 2018; Kim et al. 2020a), according to Li & Bryan (2020).

It is suggested that the hot outflow is driven by buoyancy and its entropy is its fundamental physical quantity; if the entropy of the hot bubble is higher than that of the surrounding CGM, the hot bubble becomes buoyant and drives the outflow (Bower et al. 2017). Keller et al. (2020) analytically calculated the entropy of superbubbles and the virialized Milky-way-mass halos to be about $10^8 k_B \text{ K cm}^2$. The buoyancy-driven outflow framework is supported by the MUGS2 simulations (Keller et al. 2015, 2016), and the framework may explain the ineffectiveness of SN feedback in halos more massive than $10^{12} M_\odot$ (Keller et al. 2020).

In this work, we update the stochastic thermal feedback model (Dalla Vecchia & Schaye 2012) by using the entropy of hot outflow S_{OF} as a free parameter, setting $S_{\text{OF}} = 10^8 k_B \text{ K cm}^2$ as the default value. When SN feedback occurs, thermal energy is stochastically injected to heat neighboring particles to target entropy, S_{OF} . The thermal energy required to heat the i -th gas particle is

$$\Delta E_{\text{req},i} = \frac{1}{\gamma - 1} \frac{m_i}{\mu m_H} n_i^{2/3} S_{\text{OF}}, \quad (48)$$

where n_i is the number density of the i -th gas particle. The probability of injecting thermal energy is the ratio between the solid-angle-weighted thermal energy from SN feedback (Section 3.3),

$$\Delta E_{\text{th},i} = \epsilon_{\text{th}} E_{\text{SN}} \frac{\Omega_i}{4\pi}, \quad (49)$$

and the required thermal energy:

$$P_i = \frac{\Delta E_{\text{th},i}}{\Delta E_{\text{req},i}}, \quad (50)$$

where $\epsilon_{\text{th}} = 1 - \epsilon_{\text{kin}}$ is a fraction of the SN energy deposited as thermal energy, and we adopt $\epsilon_{\text{th}} = 0.7$ as the default value (S19). We draw a random number $0 < \theta_i < 1$ for each gas particle, and inject thermal energy $\Delta E_{\text{req},i}$ to i -th gas particle if $\theta_i < P_i$. When $P_i > 1$, we simply inject a thermal energy of $\Delta E_{\text{th},i}$ to the i -th gas particle.

The original stochastic thermal feedback model by Dalla Vecchia & Schaye (2012) uses temperature increase ΔT as a free parameter and stochastically heats gas that magnitude. Their default value $\Delta T = 10^{7.5} \text{ K}$ was set for a numerical reason; the expectation value for the number of heated gas particles per SN is about 1. If this value is much smaller than 1, most SN feedback events do not inject energy into their surroundings, leading to poor sampling of the SN feedback cycle (Schaye et al. 2015). Although they provide a good reason to use ΔT as a parameter for their stochastic feedback model, the outflow properties depend on ΔT (Dalla Vecchia & Schaye 2012) and a better parameter choice is desired. In this work, we use outflow entropy as a free parameter, motivated by the high-resolution simulations (Hu 2019) and buoyancy-driven outflow framework (Bower et al. 2017; Keller et al. 2020).

4. ISOLATED GALAXY SIMULATION WITH GADGET3-OSAKA

In this section, we implement the SN feedback model based on the high-resolution ATHENA++ simulations described in the earlier sections, and demonstrate its effect on star formation and galactic outflow in an isolated galaxy simulation.

4.1. Simulation Setup

We use the GADGET3-OSAKA cosmological smoothed particle hydrodynamics (SPH) code (Aoyama et al. 2017; Shimizu et al. 2019), which is a modified

version of GADGET-3 (originally described in [Springel 2005](#), as GADGET-2⁷). We solve the SPH equation of motion, following the entropy-conserving, density-independent SPH formulation ([Hopkins 2013](#); [Saitoh & Makino 2013](#)):

$$\frac{d\mathbf{v}_i}{dt} = - \sum_j m_j (S_i S_j)^{1/\gamma} \times \left[\frac{f_{ij} \bar{P}_i}{\bar{P}_i^{2/\gamma}} \nabla_i W(r_{ij}, h_{\text{sml},i}) + \frac{f_{ji} \bar{P}_j}{\bar{P}_j^{2/\gamma}} \nabla_j W(r_{ij}, h_{\text{sml},j}) \right], \quad (51)$$

$$f_{ij} = 1 - \frac{h_{\text{sml},i}}{3S_j^{1/\gamma} \rho_i} \frac{\partial \bar{P}_i^{1/\gamma}}{\partial h_{\text{sml},i}} \left(1 + \frac{h_{\text{sml},i}}{3\rho_i} \frac{\partial \rho_i}{\partial h_{\text{sml},i}} \right)^{-1}, \quad (52)$$

where m_i , \mathbf{v}_i , S_i , $h_{\text{sml},i}$, and \bar{P}_i denote the mass, velocity, entropy (defined as $S \equiv \bar{P}/\rho^\gamma$), smoothing length, and smoothed pressure defined as

$$\bar{P}_i = \left[\sum_j m_j S_j^{1/\gamma} W(r_{ij}, h_{\text{sml},i}) \right], \quad (53)$$

of the i -th gas particle, respectively. In this formulation, the thermal energy of a particle is computed from its entropy and smoothed pressure. When thermal feedback injects energy, updating entropy assuming fixed pressure leads to the wrong result because the smoothed pressure field itself depends on the entropy. Therefore, we use an iterative method to calculate entropy change by energy injection from feedback and energy dissipation by radiative cooling ([Schaye et al. 2015](#); [Borrow et al. 2021](#)). The self-gravity of SPH and collisionless particles are also considered. We adopt the quintic B-spline kernel ([Schoenberg 1946](#); [Morris 1996](#)), and set the number of neighboring particles for each SPH particle to $N_{\text{ngb}} = 128 \pm 8$. Our code includes the time-step limiter ([Saitoh & Makino 2009](#); [Durier & Dalla Vecchia 2012](#)).

Radiative cooling is calculated using the GRACKLE-3 chemistry and cooling library⁸ ([Smith et al. 2017](#)), which solves non-equilibrium primordial chemistry and cooling for the H, D, and He species, including molecular H₂ and HD. The library also includes tabulated

rates of metal cooling calculated with the photoionization code CLOUDY ([Ferland et al. 2013](#)) and photoheating and photoionization from the ultraviolet background (UVB) radiation, and we adopt the UVB value at $z = 0$ by [Haardt & Madau \(2012\)](#). We applied a nonthermal Jeans pressure floor that forces the local Jeans length to be resolved to avoid artificial numerical fragmentation ([Hopkins et al. 2011](#); [Kim et al. 2016](#)):

$$P_{\text{Jeans}} = \frac{1}{\gamma\pi} N_{\text{Jeans}}^2 G \rho_{\text{gas}}^2 \Delta x^2, \quad (54)$$

where $\gamma = 5/3$ is the adiabatic index, $N_{\text{Jeans}} = 4$ is the Jeans number adopted from [Truelove et al. \(1997\)](#), G is the gravitational constant, and ρ_{gas} is the gas density. Δx is chosen from the larger one of either the gravitational softening length of an SPH particle or the spatial resolution of hydrodynamics ($m_{\text{gas}}/\rho_{\text{gas}}$)^{1/3}, where m_{gas} is the mass of the gas particle.

We used an initial condition taken from the AGORA project⁹ ([Kim et al. 2016](#)). The galaxy has properties characteristic of Milky Way-mass galaxies at redshift $z \sim 1$. The galaxy is composed of the following components: a dark matter halo with $M_{\text{DM}} = 1.25 \times 10^{12} M_\odot$, a stellar disk with $M_{\text{disc}} = 4.30 \times 10^9 M_\odot$, a stellar bulge with $M_{\text{bulge}} = 3.44 \times 10^{10} M_\odot$, and a gas disk with $M_{\text{gas}} = 8.59 \times 10^9 M_\odot$. The total mass of the galaxy is $1.3 \times 10^{12} M_\odot$. In the fiducial run, we employed 10^5 dark matter particles, 10^5 gas (SPH) particles, and 10^5 and 1.25×10^4 collisionless particles representing the stars in the disk and the bulge, respectively. We also added a hot gaseous halo following [Shin et al. \(2021\)](#). We randomly sampled 4×10^4 dark matter particles and added gas particles with the same mass as that of originally existing gas particles at the same position as those sampled dark matter particles. We adopt a fixed gravitational softening length of $\epsilon_{\text{grav}} = 80$ pc. We allowed the minimum gas smoothing length to reach 10 percent of the spline size of gravitational softening $2.8\epsilon_{\text{grav}}$.¹⁰ We first

⁹ <http://www.AGORAsimulations.org>

¹⁰ We use the definitions of the smoothing length and the gravitational softening length in GADGET-2 code ([Springel 2005](#)) in this paper; the gravitational softening length is equivalent to the Plummer softening length, while the smoothing length is the kernel size beyond which kernel value vanishes (see also Appendix C in [Kim et al. 2016](#)). We define the SPH spatial resolution as the smoothing length widely used in literature, $\Delta x = \eta(m/\rho)^{1/3}$ (see e.g., [Rosswog 2009](#), for review). The parameter η is usually set to $\eta \sim 1.3$, but we set it to $\eta = 1$ for simplicity. In our GADGET3-OSAKA simulation, we adopt the quintic spline kernel and $N_{\text{ngb}} = 128$. If we consider the quintic spline kernel to truncate at $3h$ as in [Price \(2012\)](#) (see also [Dehnen & Aly 2012](#), for another definition of the smoothing length in terms of the smoothing kernel), we set to $\eta = 1.04$ in our simulation, effectively.

⁷ <https://wwwmpa.mpa-garching.mpg.de/gadget/>

⁸ <https://grackle.readthedocs.io>

The default solar metallicity in GRACKLE-3 is $Z_\odot = 0.0134$. This value is smaller than the value of Z_\odot that was used in Eq. (10) by a factor of 1.45. This difference will affect the calculation of terminal momentum in Eq. (16), however the power index on $\Lambda_{6,-22}$ term is small so that the impact on the value of $p_{\text{sf,m}}$ is negligible.

evolve the system to 0.5 Gyr adiabatically for relaxation to set up the initial condition, and then evolve it to 1 Gyr with the sub-grid physics including cooling, UVB heating, star formation, and stellar feedback.

4.2. Star formation and Stellar feedback

4.2.1. Star formation

We assume star formation to occur when the gas number density $n > 10 \text{ cm}^{-3}$ and temperature $T < 10^4 \text{ K}$. We use the same star formation prescription as S19, a Schmidt-type star formation law (Schmidt 1959). The star formation rate (SFR) density is (Cen & Ostriker 1992; Katz 1992; Nagamine et al. 2001; Springel & Hernquist 2003; Stinson et al. 2006; Kim et al. 2014, 2016)

$$\dot{\rho}_* = \epsilon_* \frac{\rho_{\text{gas}}}{t_{\text{ff}}}, \quad (55)$$

where ϵ_* is the star formation efficiency, ρ_{gas} is the gas density, and $t_{\text{ff}} = \sqrt{3\pi/(32G\rho_{\text{gas}})}$ is the local free-fall time. We adopt $\epsilon_* = 0.05$. The star particles are stochastically spawned from gas particles to follow the SFR density. Each gas particle can spawn a maximum of n_{spawn} star particles. The initial mass of the star particle is defined as $m_* = m_{\text{gas}}/n_{\text{spawn}}$, where m_{gas} is the mass of the gas particle. We have adopted $n_{\text{spawn}} = 2$ throughout this paper, using a simple stellar population (SSP) approximation and assuming each star particle to consist of a cluster of stars whose mass function follows the Chabrier IMF (Chabrier 2003) with a mass range of 0.1-100 M_{\odot} .

4.2.2. Stellar feedback

We consider stellar wind from massive stars, Type II SNe, Type Ia SNe, and stellar wind from the asymptotic giant branch (AGB) stars as stellar feedback, while distributing the physical quantities from them using the spherical superbubble model. We use CELIB to calculate time and metallicity-dependent mass, metal, and energy input from Type II SNe, Type Ia SNe, and AGB stars (see S19, figure 1). To deposit energy and metals gradually rather than at a single instant, we divide each feedback from the star particle into n_{fb} events and adopt $n_{\text{fb}} = 8$ throughout this paper (S19).

Type II SN feedback—We assume the range of the progenitor mass to be 13 – 40 M_{\odot} and the hypernova fraction to be $f_{\text{HN}} = 0.05$. In the case of solar metallicity, the specific energy of Type II SNe is $\epsilon_{\text{SNII}} = 7.19 \times 10^{48} \text{ erg } M_{\odot}^{-1}$. We assume the SN energy to be 10^{51} erg and estimate shock radius and momentum input from SN feedback using equations (36) and (33). When SN feedback occurs at a low-density void formed by previous feedback events, we may overestimate the shock

radius. Thus, we set an upper limit on the mass enclosed inside the shock radius $M(R_{\text{max}}) = 2 \times 10^3 m_*/n_{\text{fb}}$. This limit comes from a rough estimate of the SNR mass at fadeaway under an assumption that the terminal momentum per SN is $p \sim 2 \times 10^5 M_{\odot} \text{ km s}^{-1}$, the sound speed of star-forming cloud is $c_s \sim 1 \text{ km s}^{-1}$, and the SN rate is $N_{\text{SN}} \sim m_*/(100 M_{\odot})$.

Type Ia SN feedback—We adopted the delay-time distribution function with a power law of t^{-1} for Type Ia SNe event rate (e.g., Totani et al. 2008; Maoz & Mannucci 2012), using equations (36) and (33) to estimate shock radius and momentum input, although Type Ia SN explosions are intermittent. One can estimate the momentum input from a single Type Ia SN using equation (9), assuming the SNR formed by a single SN to acquire about 77 % of its terminal momentum by the shell-formation time (Kim & Ostriker 2015). For Type Ia SN feedback, we ignore thermal feedback because the formation of a hot bubble by stochastic thermal feedback represents superbubble formation by clustered Type II SNe. We used the same upper limit as Type II SN feedback on the shock radius.

Stellar wind from OB stars—For stellar wind feedback from OB stars, we consider only mechanical feedback. We calculated the energy of the stellar wind from OB star using STARBURST99¹¹ (Leitherer et al. 1999; Vázquez & Leitherer 2005; Leitherer et al. 2010, 2014) and set the specific energy of stellar wind to $\epsilon_{\text{SW}} = 1.5 \times 10^{48} \text{ erg } M_{\odot}^{-1}$. Assuming 30 % of the energy turns into kinetic energy, we estimate the shock radius and momentum input using the equation (36) and (33) by setting $N_{\text{SN}} = m_* \epsilon_{\text{SW}} / (10^{51} \text{ erg})$. Here we choose to use the equation of superbubble momentum because the specific luminosity of stellar wind and Type II SNe are similar (e.g., Agertz et al. 2013). We set an upper limit on the mass enclosed inside the shock radius $M(R_{\text{max}}) = 2 \times 10^2 m_*/n_{\text{fb}}$. This limit is one order smaller than that of SN feedback because the amount of energy injected by stellar winds is about one order smaller than that injected by SNe. The adopted numbers above translates to a specific momentum injection rate of $\dot{p}/M \sim 100 \text{ km/s/Myr}$. However, Lancaster et al. (2021b) have shown that the wind specific momentum injection rate from O star winds in a cluster is $\dot{p}/M \sim 10 \text{ km/s/Myr}$ due to fractal mixing boundary layer. Our model here can be regarded as an upper limit of O star winds.

¹¹ <https://www.stsci.edu/science/starburst99/docs/default.htm>

We do not use our stochastic thermal feedback model for OB stars because ionization heating is limited to 2×10^4 K by hydrogen recombination, and heating to higher temperature is unphysical. Just heating to 2×10^4 K is ineffective due to overcooling. In reality, radiation pressure and ionization heating form low-density H II bubbles, but we don't have a reasonable subgrid model for the bubble formation process.

AGB feedback—For stellar wind from AGB stars, we only consider mass and metal input. We cannot resolve the circumstellar envelope of an AGB star at $R \lesssim 1$ pc (e.g., Höfner & Olofsson 2018). In our simulations, a star particle represents a star cluster; however, in reality, stars are dispersed. To account for this, we consider the star particle to be representative of stars in the surrounding gas with a mass of $100m_*$ assuming the star formation efficiency to be $\epsilon_* \sim 0.01$. Thus, we set the mass enclosed inside the shock radius of the AGB feedback to $M(R_{\text{shock}}) = 100m_*$ and distribute the mass and metals to gas particles inside the shock radius. We do not consider the mechanical feedback from stellar winds because it is slower ($\sim 10 \text{ km s}^{-1}$) than (and negligible in comparison to) SN feedback. However, we add a boost-back momentum for momentum conservation. If the relative velocity between the star and gas particles is large, the boost-back momentum can have a significant impact (Hopkins et al. 2018; Su et al. 2019).

4.3. Results from GADGET3-OSAKA simulations

To explore the thermal and mechanical feedback effects, we ran five simulations with different feedback (FB) settings, as summarized in Table 2. We retained the amount of mass and metals ejected by SNe and AGB stars and changed only the energy and momentum injection models. When a FB is turned off, the energy for the FB is reduced. All simulations have AGB feedback.

4.3.1. Projection Maps

Figures 11, 12, and 13 show the density-weighted projection plots of density, temperature, and metallicity of the simulated galaxies at $t \simeq 1$ Gyr. Galaxies are centered at the density-weighted center of gas mass,

$$\mathbf{r}_{\text{center}} = \frac{\sum_i \rho_i m_i \mathbf{r}_i}{\sum_i \rho_i m_i}. \quad (56)$$

In Figure 11, one can see that the density structure in the presence of mechanical feedback differs from that in its absence. The gas disk is maintained for 1 Gyr in three runs with Type II SN mechanical feedback (Fiducial, Non-stochastic, and SNII-kinetic) while the gas disks

become clumpy in the other two runs. This result suggests that the galactic disk is supported against gravity by the turbulence driven by mechanical feedback. Comparing the Fiducial and Non-stochastic runs, the effect of stochastic thermal feedback is not clearly seen in the density distribution.

Figure 12 shows the density-weighted temperature. One can see the hot bubbles formed by the stochastic thermal feedback inside the gas disks in the Fiducial and SNII-thermal runs, which escape from the galactic disk to produce the hot outflow. This feature is observed in X-ray by Nakashima et al. (2018), who suggested that the hot, gaseous halo of the Milky Way is formed by the hot outflow resulting from stellar feedback. The low-density regions created by mechanical feedback or gas depletion are shown as $\sim 10^6$ K because we set the initial temperature of the halo to 10^6 K.

The density-weighted metallicity is depicted in Figure 13. It should be noted that we did not change the metal injection model, and that these five runs are different at the models of energy and momentum injection. The metal distribution above the galactic disks in the presence of stochastic thermal feedback differs from that in its absence. We also indicate the distribution of metals on the virial radius (205 kpc) scale in Figure 14. Metal outflows were not observed in the Non-stochastic run. This result is consistent with those of Shin et al. (2021), who demonstrated that metal outflow is suppressed by ram pressure from the hot gaseous halo using GADGET2 code with a simple thermal dump SN feedback model. On the other hand, the Fiducial run shows the metal outflows beyond the virial radius. We will further compare our work with that of Shin et al. (2021) in Section 4.3.5.

4.3.2. Phase Diagrams

Fig. 15 shows the phase diagrams of simulated galaxies at $t = 1$ Gyr. The dense, cold gas ($T < 5 \times 10^3$ K) in the galactic disk is visible on the lower right corner. In three runs with mechanical SN feedback (Fiducial, Non-stochastic, and SNII-kinetic), two-phase ISM of the warm ($T \sim 2 \times 10^3$ K) and cold ($T \sim 3 \times 10^2$ K) phases were observed. Compared with them, the warm phase is less visible and the cold gas is more condensed at a lower temperature ($T < 10^2$ K) in SNII-thermal and No-FB runs. The hot, tenuous gas heated by thermal feedback adiabatically cools and joins the hot gaseous halo in the upper left region with $T \sim 10^6$ K. We do not see a difference in the upper left gas distributions of the Non-stochastic and No-FB runs, which indicates ineffective thermal feedback in the Non-stochastic run. The hot component is most visible in the SNII-thermal

Table 2. List of isolated galaxy simulations used in this paper.

Run Name	Feedback Type				Note
	Type II SN	Type II SN	Stochastic	Type Ia & OB star	
	mechanical FB	thermal FB	thermal FB	mechanical FB	
Fiducial	✓	✓	✓	✓	Fiducial run with all feedback models
Non-stochastic	✓	✓		✓	Fiducial but thermal energy is distributed without stochastic treatment
SNII-kinetic	✓				Type II SN mechanical feedback only
SNII-thermal		✓	✓		Type II SN thermal feedback only
No-FB					No feedback

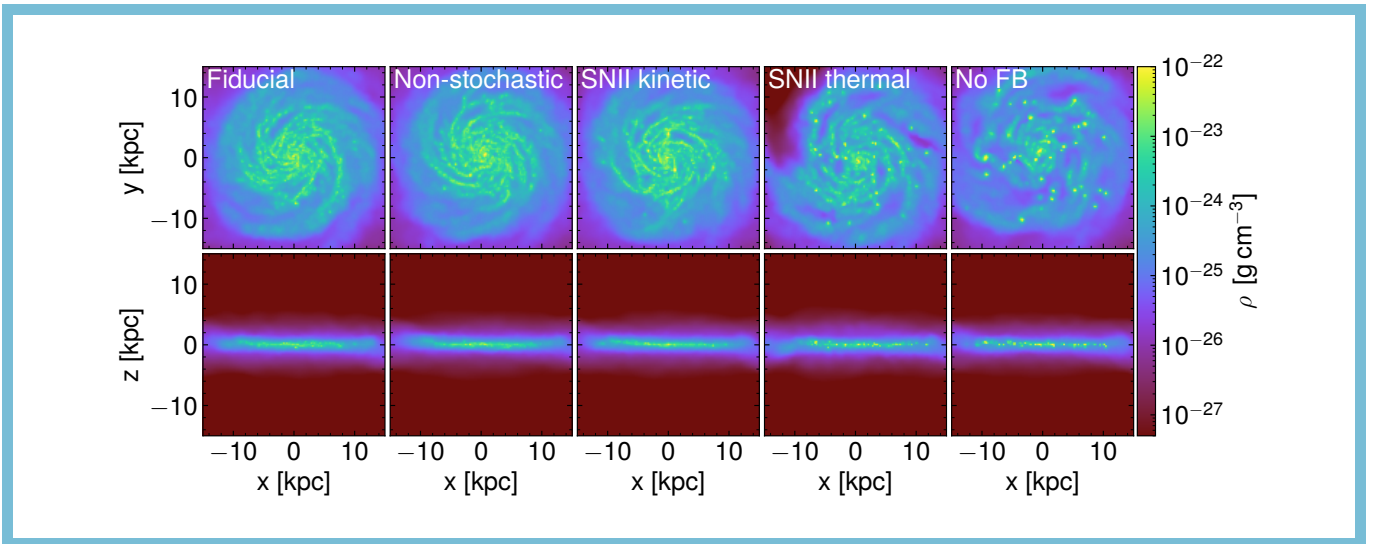


Figure 11. Projected gas density plots of the isolated galaxies in given Table 2 at $t \simeq 1$ Gyr in $30 \text{ kpc} \times 30 \text{ kpc}$ images. The top and bottom rows depict face-on and edge-on images, respectively. Here, we plot $\sum \rho^2 / \sum \rho$ to enhance the contrast and to use the same density-weighted method for both temperature and metallicity. An animated version of this figure, showing the evolution of these panels during $t = 0\text{--}1$ Gyr, is available in the HTML version of this article.

run due to its higher star formation rate and subsequent thermal feedback.

4.3.3. Star Formation Histories

Figure 16 depicts the star formation history of the simulated galaxy. Star formation is suppressed in all the runs with feedback compared to the No-FB run. The thermal feedback suppresses star formation, and the mechanical feedback suppresses it further. Star formation rate in the Fiducial and Non-stochastic runs are slightly lower than that in the SNII-kinetic run because the mechanical feedback from Type Ia SNe and OB stars are not considered in the SNII-kinetic run. In our previous work (S19), we observed an ‘initial star burst’ which occurs just after the beginning of the simulations due to the collapse of gas without feedback. This phenomenon

is weakened in this work because we first adiabatically evolve the initial condition to 0.5 Gyr for relaxation and then plot the star formation history with an interval of 5 Myr, which is approximately equal to the lifespan of a massive star.

4.3.4. Kennicutt–Schmidt Relation

Figure 17 shows the Kennicutt–Schmidt relations of the simulated galaxies given in Table 2 at $t = 1$ Gyr calculated with $500 \text{ pc} \times 500 \text{ pc}$ patches up to the galactic radius of $R = 10 \text{ kpc}$. The results from our simulations agree with the observed range by Bigiel et al. (2008); Schrubba et al. (2011) with a similar slope and normalization, which is encouraging. The three runs with mechanical feedback (Fiducial, Non-stochastic, and SNII-kinetic) show similar results, and their star formation

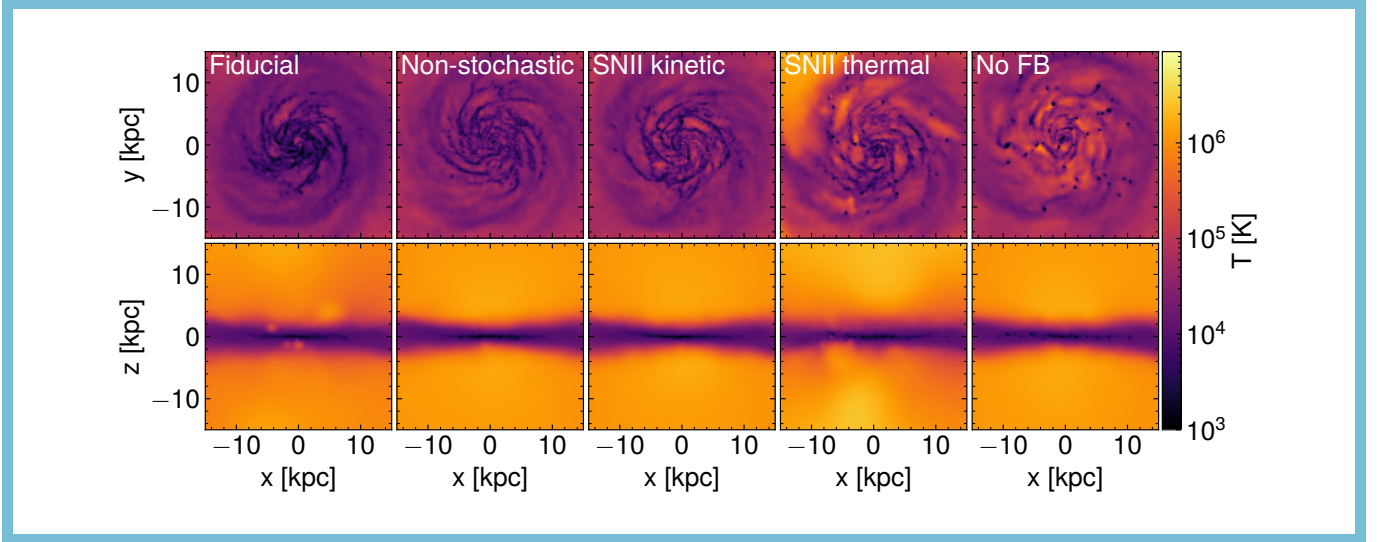


Figure 12. Projected temperature (density-weighted) of the isolated galaxies given in Table 2 at $t \simeq 1$ Gyr. The top and bottom rows depict face-on and edge-on images. The hot gas above the disk in the No-FB run is due to the galactic halo gas with $T = 10^6$ K implemented in the initial condition. An animated version of this figure, showing the evolution of these panels during $t = 0$ –1 Gyr, is available in the HTML version of this article.

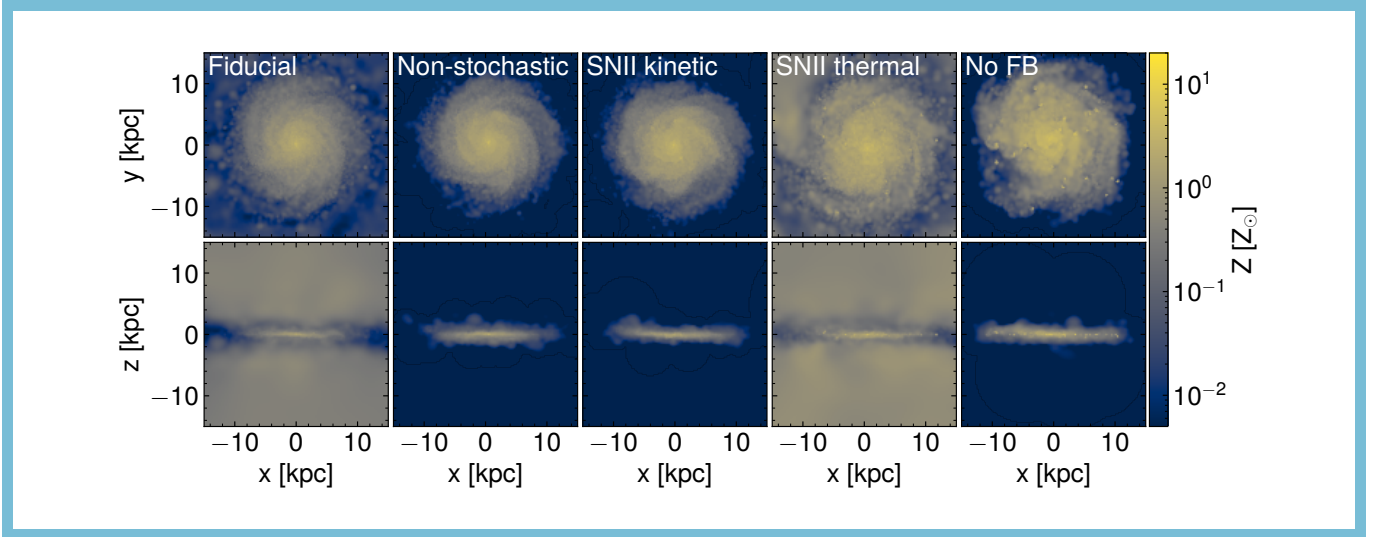


Figure 13. Projected metallicity (density-weighted) of the isolated galaxies given in Table 2 at $t \simeq 1$ Gyr. The top and bottom rows depict face-on and edge-on images. Metals carried by the outflows are visible above and below the disk. An animated version of this figure, showing the evolution of these panels during $t = 0$ –1 Gyr, is available in the HTML version of this article.

rate density is lower by a factor of 2–3 than that of No-FB run. The SNII-thermal run is inbetween No-FB and other runs consistently with Fig. 16. The simulated data fluctuates as a function of time but on average stays within the observed range. The Fiducial and Non-stochastic runs have the lowest Σ_{SFR} among all runs due to low SFR, as shown in Fig. 16.

The simulation data point corresponding to the highest gas column density is above the observed data; at this point, it is unclear if our results will turn over at

higher column densities due to limitations in our resolution. The cut-off at the lower end of the simulation data is determined by mass resolution and by how well we can track star formation in a low-density region, which will be explored in future works.

4.3.5. Outflow Profiles of Mass, Energy, Velocity, and Metals

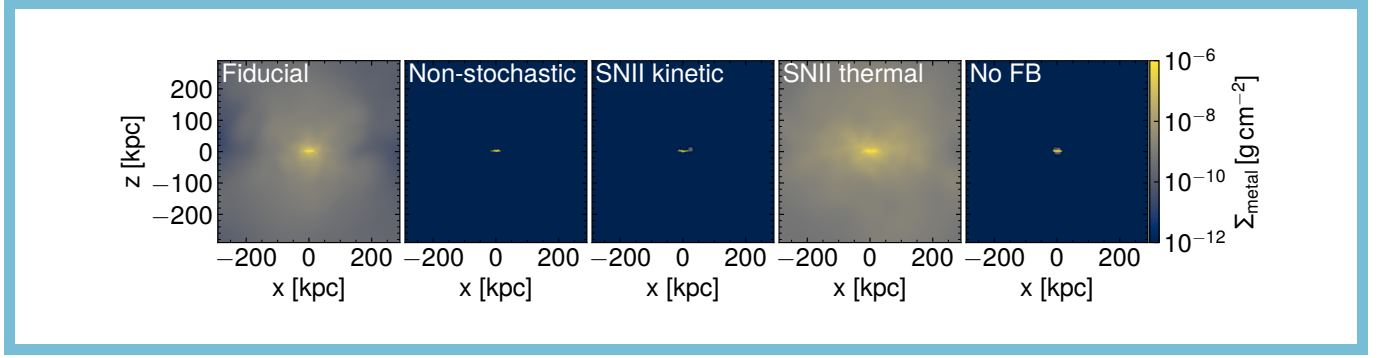


Figure 14. Large-scale, edge-on view of metal column density at $t \simeq 1$ Gyr. It is clear that the metals are carried over large distances in the Fiducial and SNII-thermal runs. An animated version of this figure, showing the evolution of these panels during $t = 0$ –1 Gyr, is available in the HTML version of this article.

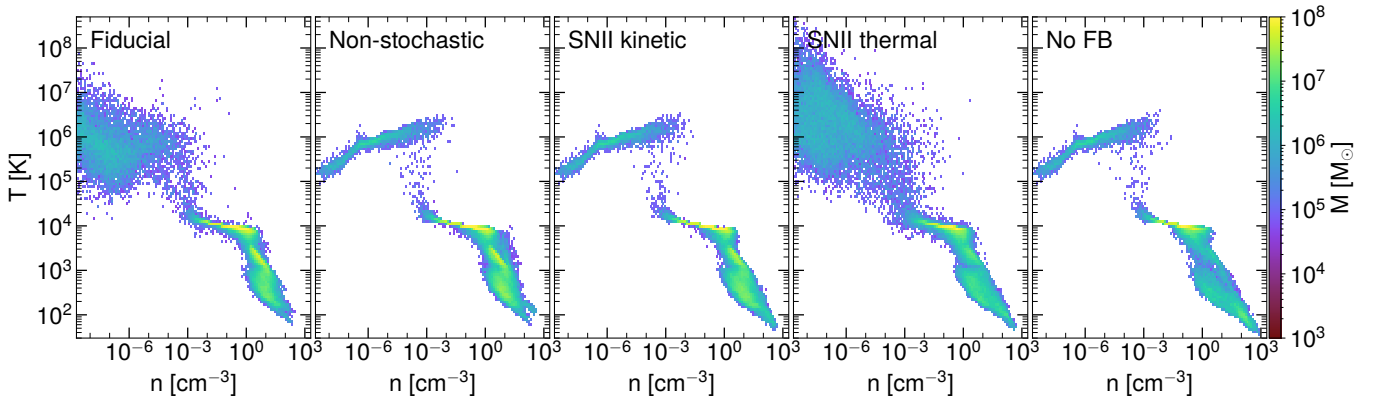


Figure 15. Phase diagram of the gas in the isolated galaxies given in Table 2 at $t \simeq 1$ Gyr. The dense, cold gas ($T < 10^3$ K) in the galactic disk is visible on the lower right corner. The hot, tenuous gas heated by feedback adiabatically cools and then joins the hot gaseous halo in the upper left region with $T \sim 10^6$ K. The hot component is most visible in the SNII-thermal run due to the highest star formation rate and subsequent strong thermal feedback. The hot gas seen in the No-FB run is due to the hot halo implemented in the initial condition.

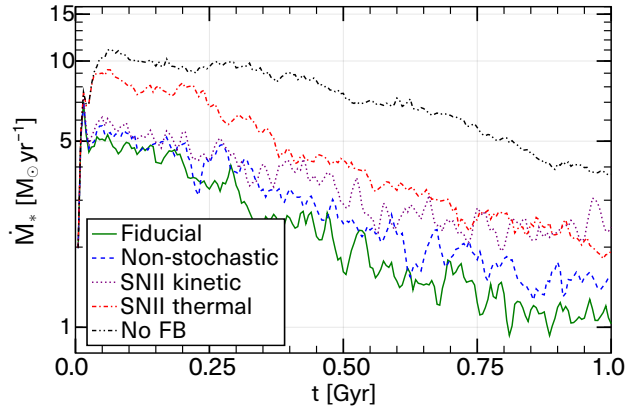


Figure 16. Star formation rate as a function of time for the isolated galaxy simulations given in Table 2. The No-FB run has the highest SFR, and the SNII-thermal run shows weak suppression of SFR. In other runs, SFR is suppressed by the mechanical SN feedback efficiently.

The outflow rate of physical value X at a height H above the galactic plane is

$$\begin{aligned} \dot{X}_{\text{out}}(H) &= \int \rho_X v_z dS_H \\ &= \int_{S_H} \sum_i X_i v_{i,z} W(r_{ij}, h_{\text{sml},i}) d\mathbf{r}_j, \quad (57) \end{aligned}$$

where S_H , ρ_X , and v_z denote the plane at height H , the density of X , and velocity in the z -direction, while W indicates the kernel function used in the simulation. Other symbols, such as r_{ij} , $v_{i,z}$, and $h_{\text{sml},i}$ denote the distance from the i -th gas particle to \mathbf{r}_j , the z -direction outflow velocity, and the smoothing length of the i -th gas particle, respectively. We rewrite this equation as follows, to compute the outflow rate from simulation

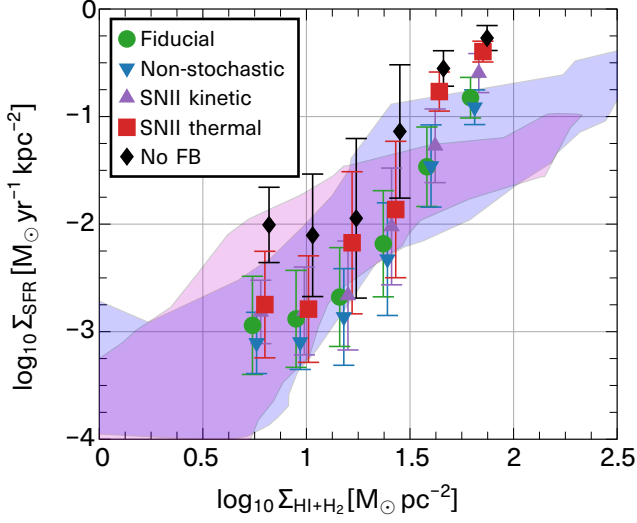


Figure 17. The Kennicutt–Schmidt relation of the simulated galaxies given in Table 2 at $t \simeq 1$ Gyr, calculated with $500 \text{ pc} \times 500 \text{ pc}$ patches. Coloured regions depict the observational data of nearby spiral galaxies (blue: Schrubla et al. 2011; magenta: Bigiel et al. 2008).

snapshots (Shimizu et al. 2020):

$$\begin{aligned} \dot{X}_{\text{out}}(H) = & \\ \sum_i X_i v_{i,z} \int_0^{\sqrt{h_{\text{sml},i}^2 - \zeta_i^2}} 2\pi\xi W\left(\sqrt{\zeta_i^2 + \xi^2}, h_{\text{sml},i}\right) d\xi, & \end{aligned} \quad (58)$$

where $\zeta_i = |z_i - H|$ and z_i is the z coordinate of i -th particle.¹² To evaluate the intrinsic outflow, we take the summation over those outflowing gas particles that have non-zero metallicity. Since the metallicity is initially zero and metal mixing between gas particles is not considered, such particles are considered as metal-enriched outflows.

¹² We used the quintic B-spline kernel function in our simulations. In this case, the integral accounting for the cross-section of the SPH particle and the plane of height H can be analytically calculated as

$$\begin{aligned} \int_0^{\sqrt{h^2 - \zeta^2}} 2\pi\xi W\left(\sqrt{\zeta^2 + \xi^2}, h\right) d\xi \\ = f_{\frac{1}{3},1}(\zeta, h) + f_{-2,\frac{2}{3}}(\zeta, h) + f_{5,\frac{1}{3}}(\zeta, h), \end{aligned} \quad (59)$$

where

$$f_{a,b}(\zeta, h) = \frac{3^9 a}{359 h^2} \left(b - \frac{\zeta}{h}\right)_+^6 \left(\zeta + \frac{h}{7} \left(b - \frac{\zeta}{h}\right)_+\right). \quad (60)$$

Here, $(\cdot)_+ \equiv \max(0, \cdot)$.

We depict the outflow profiles of mass, energy, and metal loading factor

$$\eta_m = \frac{\dot{M}_{\text{out}}}{\dot{M}_*}, \quad (61)$$

$$\eta_e = \frac{\dot{E}_{\text{out}}}{\epsilon_{\text{SNII}} \dot{M}_*}, \quad (62)$$

$$\eta_Z = \frac{\dot{M}_{Z,\text{out}}}{\mu_{Z,\text{SN}} \dot{M}_*}, \quad (63)$$

averaged over $t = 0.5 - 1.0$ Gyr, in Fig. 18. Here, \dot{M}_{out} , \dot{E}_{out} , and $\dot{M}_{Z,\text{out}}$ are the outflow rates of mass, energy, and metals, while \dot{M}_* is the star formation rate and $\mu_{Z,\text{SN}} = 0.01$ is the specific metal mass released by Type II SNe. We also compute density-weighted, average outflow velocity,

$$\begin{aligned} V_{\text{out}}(H) = \frac{\int \rho v_z dS_H}{\int \rho dS_H} = \\ \frac{\sum_i m_i v_{i,z} \int_0^{\sqrt{h_{\text{sml},i}^2 - \zeta_i^2}} 2\pi\xi W\left(\sqrt{\zeta_i^2 + \xi^2}, h_{\text{sml},i}\right) d\xi}{\sum_i m_i \int_0^{\sqrt{h_{\text{sml},i}^2 - \zeta_i^2}} 2\pi\xi W\left(\sqrt{\zeta_i^2 + \xi^2}, h_{\text{sml},i}\right) d\xi}, \end{aligned} \quad (64)$$

where m_i is the mass of the i -th gas particle. The profiles of the total mass and the metal loading factor are high at low altitudes, decrease rapidly to $H \sim 1.0$ kpc, and become flatter at $H \gtrsim 1.0$ kpc.

At $H \lesssim 1.0$ kpc, the cool ($T < 2 \times 10^4$ K) component dominates mass outflow (higher η_m in the top middle panel of Fig. 18), which is slow ($V \lesssim 30 \text{ km s}^{-1}$) and falls back to the galaxy. We see that the mass loading factor of cool outflow in the runs with feedback is greater by ~ 0.8 dex over that of No-FB run.

At $H \gtrsim 2.5$ kpc, the hot ($T > 2 \times 10^4$ K) component dominates outflow. We see that the mass loading factor of hot outflow in runs with stochastic thermal feedback (Fiducial and SNII-thermal) is much higher than that of others, which indicates that stochastic thermal feedback launches hot outflow. Non-stochastic and SNII-kinetic runs shows much weaker hot outflow, demonstrating that simply distributing thermal energy from SN feedback is ineffective in launching hot outflow. The outflow profile of Fiducial run is qualitatively consistent with high-resolution shearing box simulations by Kim et al. (2020a).

Figure 19 shows the outflow profiles up to 200 kpc. We calculate the outflow rates at the surface of a sphere with a radius R centered at the galactic center, and show the loading factors and outflow velocity of all components. The hot component dominates at $R > 10$ kpc with cool component disappearing at large R . We see the outflow is accelerated towards large R and reaches $\gtrsim 560 \text{ km s}^{-1}$ at $R = 200$ kpc. The mass loading factor of Fiducial run

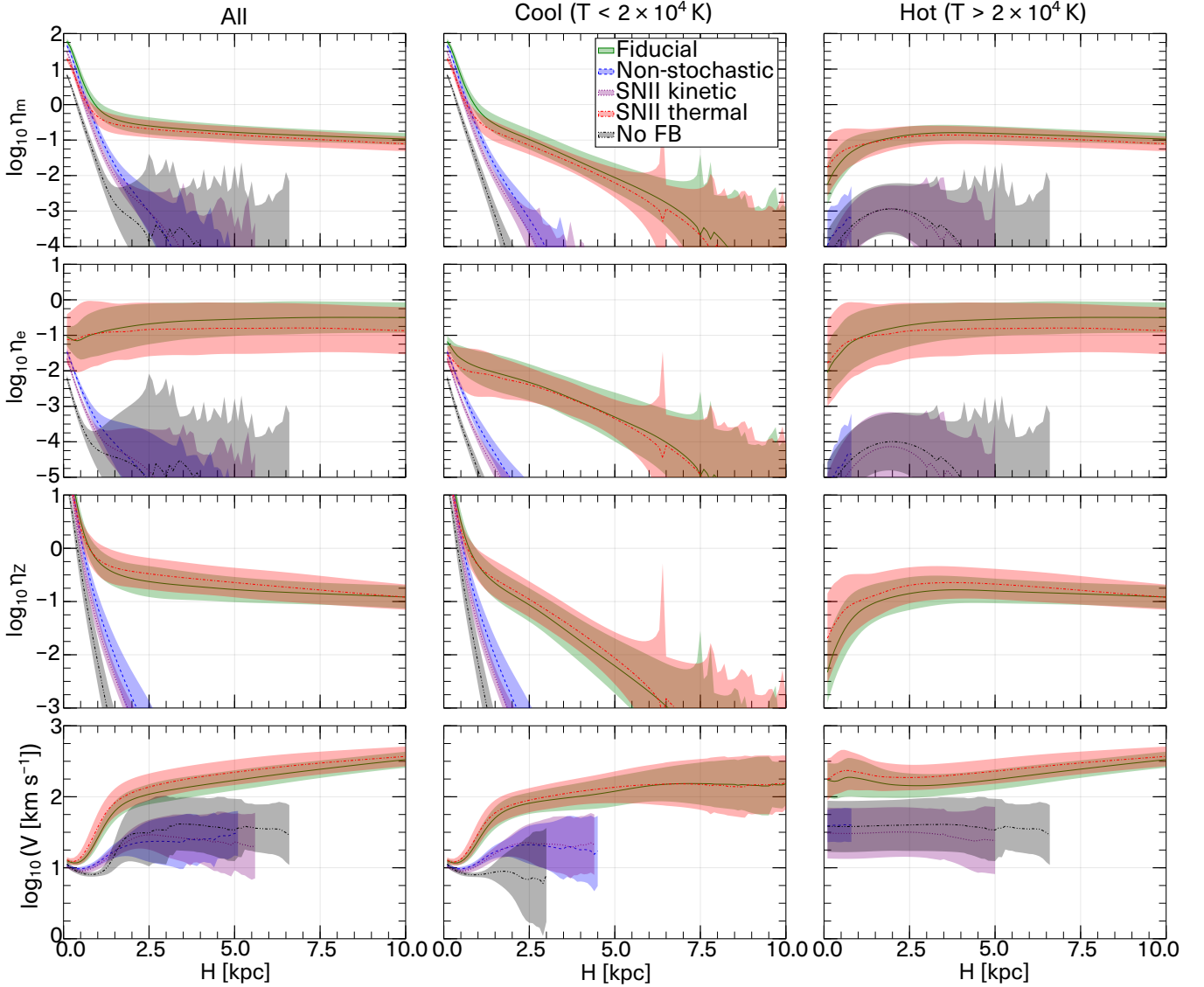


Figure 18. Mass (top row), energy (second row), and metal (third row) loading factors vs. the height above the galactic plane. The fourth row depicts outflow velocity vs. the height above the galactic plane. All quantities are measured using cylinders of different heights and a 10 kpc radius and averaged over $t = 0.5 - 1.0$ Gyr. The lines indicate the average values during this time period, with $\pm 1\sigma$ shade for time variation.

at $R = 200$ kpc is $\eta_m \sim 0.3$. In all the panels the SNII-thermal model shows somewhat higher loading factors and outflow velocity than the Fiducial run, which is due to higher SFR in the former model as was shown in Fig. 16.

For the presented isolated galaxy test, we followed Shin et al. (2021) in adding a gaseous halo to the initial condition. As shown in Fig. 18, metals are transported via the hot outflow driven by thermal feedback, while the cool outflow cannot transport metals beyond $H = 5$ kpc. This is because the hot outflow driven by thermal feedback is not impeded by the ram pressure of the gaseous halo $P_{\text{ram}} = \rho v^2$ due to its higher thermal

pressure. On the other hand, the cool outflow is decelerated by the ram pressure of the gaseous halo because it is not accelerated after its initial launch by momentum feedback.

Our stochastic thermal feedback model heats the gas particles up to a higher temperature than simple thermal dump models do, driving hot outflow without increasing the total SN feedback energy by hand. The discrepancy in metal outflow between mesh-based (ENZO) and particle-based (GADGET-2 and GIZMO) simulations reported by Shin et al. (2021) could be due to the difference in mass resolution; particle-based simulations fix the mass resolution, but mesh-based simulations do not

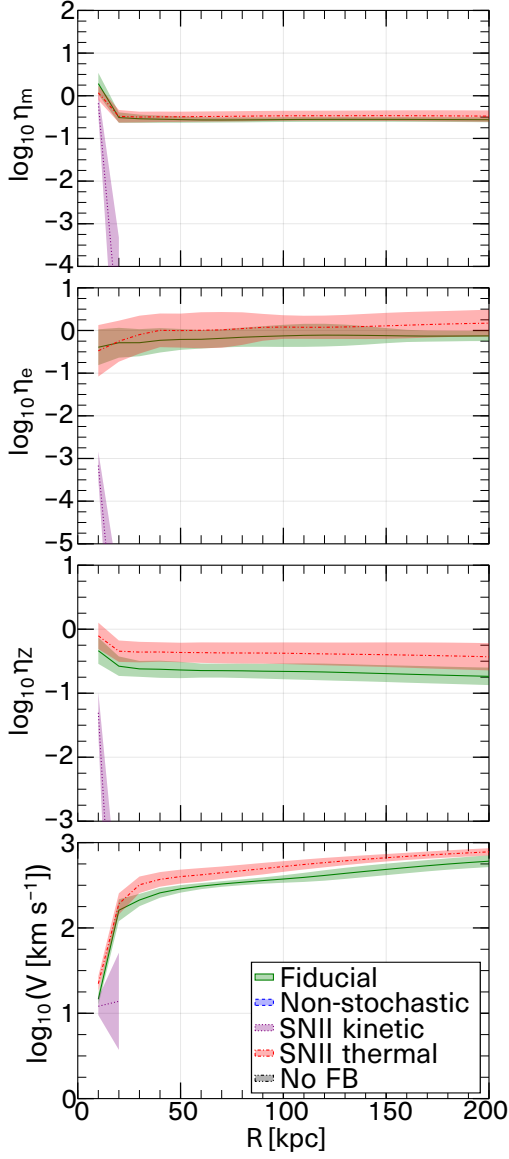


Figure 19. Same as Figure 18 but measured with spheres of different radii up to 200 kpc, centered at the galactic center and averaged between $t = 0.5 - 1.0$ Gyr. The lines show the average during this time period with $\pm 1\sigma$ shade for the time variation.

fix it and can effectively heat gas cells at low-density voids created by previous SN feedback events.

5. DISCUSSION

5.1. On the momentum of superbubble

Pressure-driven versus Momentum-driven—When $\Delta t_{\text{SN}} < 0.1 t_{\text{PDS}}$, the gas inside the shell is expected to be hot even after shell formation; thus, we expect a pressure-driven evolution, $p \propto t^{7/5}$ (Eq. B23), but we observe $p \propto t$. There could be three reasons for this.

First is that the deceleration due to ram pressure is ignored in the pressure-driven model, as explained below. The ram pressure and the pressure of the hot gas immediately after shell formation are

$$\begin{aligned} P_{\text{ram}} &= \rho V_{\text{sf,m}}^2 \\ &= 5.5 \times 10^6 k_{\text{B}} \text{ K cm}^{-3} E_{51}^{0.18} \Delta t_{\text{SN},6}^{-0.18} n_0^{1.2} \Lambda_{6,-22}^{0.34} \end{aligned} \quad (65)$$

$$\begin{aligned} P_{\text{hot}} &= (\gamma - 1) \frac{(1/2) f_{\text{th}} E_{\text{SN}} (t_{\text{sf,m}} / \Delta t_{\text{SN}})}{(4/3) \pi R_{\text{sf,m}}^3} \\ &= 1.7 \times 10^6 k_{\text{B}} \text{ K cm}^{-3} E_{51}^{0.18} \Delta t_{\text{SN},6}^{-0.18} n_0^{1.2} \Lambda_{6,-22}^{0.34}, \end{aligned} \quad (66)$$

where $R_{\text{sf,m}}$ and $V_{\text{sf,m}}$ are the radius and velocity at shell formation from Eqs. (13) and (14), respectively, $E_{\text{SN}} = 1 \times 10^{51}$ erg is the SN energy, $f_{\text{th}} = 0.78$ is the fraction of thermal energy in superbubble energy (Weaver et al. 1977), and factor 1/2 is for energy dissipation at shell formation (Eq. A11). Since $P_{\text{ram}} > P_{\text{hot}}$, the ram pressure cannot be neglected immediately after shell formation. Therefore, even if the gas inside is hot, the superbubble is not expected to obey the pressure-driven model.

The second reason is that the timescale of our simulations is not long enough, therefore continuous luminosity approximation does not apply. El-Badry et al. (2019) discussed the timescale t_{subsonic} , at which an SN blast becomes subsonic before reaching the outer shell. Our simulation timescale is shorter than t_{subsonic} . In supersonic case ($t < t_{\text{subsonic}}$), each SN deposits momentum impulsively, and superbubble is driven by the momentum injection. El-Badry et al. (2019) performed long-term 1D simulations, and showed that the superbubble makes a transition from momentum-driven to pressure-driven after t_{subsonic} . It will be our future work to run long-term 3D simulations to investigate whether the transition is observed also in 3D simulations.

The third reason is that the pressure of the hot gas decreases as the heat is transported to the shell at the mixing layer. Yadav et al. (2017) performed 3D simulations of the superbubble and showed that about 90% of the injected energy is lost by radiation after the energy is transported into the shell. Lancaster et al. (2021a) pointed out that the energy losses are greater in 3D than in 1D simulations due to the fractal area of the interface originating from inhomogeneous ISM, and it would be necessary to use a turbulent diffusion coefficient depending on the bubble size as in Eq. (37) of Lancaster et al. (2021a) to capture this.

As the turbulence develops through various instabilities such as Kelvin–Helmholtz (Thompson 1871;

Helmholtz 1868; Heitsch et al. 2006; Fielding et al. 2020), Rayleigh–Taylor (Rayleigh 1882; Taylor 1950; Bucciantini et al. 2004; Badjin et al. 2016), Richtmyer–Meshkov (Richtmyer 1960; Meshkov 1972; Inoue et al. 2013), or Vishniac instabilities (Vishniac 1983; Krause et al. 2013; Minière et al. 2018), the area of turbulent contact surface with the hot gas increases, which in turn increases the energy loss. Therefore, the time dependence becomes shallower than the pressure-driven model, $p \propto t^{7/5}$.

Multiple SN explosions and mixing—In our ATHENA++ calculations, the momentum per SN explosion is about a few $\times 10^5 M_{\odot} \text{ km s}^{-1}$. This is comparable to the results of previous studies of the momentum per isolated SN explosion (Kim & Ostriker 2015; Martizzi et al. 2015), and does not show an increase in momentum due to multiple SN explosions, contrary to Gentry et al. (2017). The results for the superbubble momentum depend on whether the mixing of the shell and hot gas is considered (Gentry et al. 2019; El-Badry et al. 2019). When the mixing of the hot bubble-shell boundary is considered, the hot bubble is efficiently cooled at the bubble-shell boundary. In our 3D Eulerian ATHENA++ simulations, the mixing between the shell and the hot gas is considered, and thus the momentum enhancement is not observed, which is consistent with the findings of Kim et al. (2017) for multiple SNe.

Thermal conduction and turbulence—In this study, we also added the setup of Kim et al. (2017) to account for thermal conduction and turbulence, and the superbubble momentum was comparable to their results. El-Badry et al. (2019) showed that this is because mixing is more dominant than heat conduction in energy transport at the bubble–shell boundary, and the energy conducted to the shell is returned to the hot bubble by evaporation. Therefore, we do not see significant differences in momentum when heat conduction is accounted for, as was shown by Kim et al. (2017). The resolution of our simulation is not as high as that of El-Badry et al. (2019) and conduction is probably not captured so well, but we do observe the transfer of mass from cold shell to the hot interior as we saw in Fig. 4.

The turbulence considered in this study corresponds to a Mach number of $\mathcal{M} \sim 1$. If the turbulence is much stronger with $\mathcal{M} > 10$, the momentum could be reduced by about 30 % (Martizzi et al. 2015) due to increased radiative cooling caused by mixing between cold gas clouds and hot bubbles in the ISM.

Comments on Δt_{SN} , t_{sf} , and caveat on non-equilibrium cooling effect—The time evolution of the superbubble momentum can be modeled in a unified manner using

Eq. (28) under different metallicity, density, and Δt_{SN} by normalizing the time and momentum by those at the shell-formation time (Fig. 9), which is useful to estimate the momentum of superbubble for the application to the subgrid model of galaxy simulations. Therefore, the accurate determination of the shell-formation time is important.

When the superbubble momentum is translated to momentum per single SN, it sensitively depends on Δt_{SN} as was also shown by Kim et al. (2017). Because the time interval of SN explosions depends on the mass of the stellar cluster, the initial stellar cluster mass function will be important for the discussion of SN feedback in the context of galaxy formation.

We assumed collisional ionization equilibrium in this study because the shell-formation time remains unchanged even after accounting for non-equilibrium cooling, radiation transport, and heat conduction (Sarkar et al. 2021) in the case of an isolated supernova explosion. As for the temperature, the timescale where the ion and electron temperatures balance in an isolated supernova explosion is 10^4 yr (Itoh 1978), which is shorter than the shell-formation time, so the different temperatures between ions and electrons do not affect the shell-formation time significantly. However, these assumptions need to be checked for intermittent SN explosions in the future.

5.2. On the SN feedback model

In our model, we assume that the superbubbles spread isotropically. However, when the ISM is highly non-uniform, the superbubbles spread selectively towards the low-density channel (Ohlin et al. 2019). In particular, when the superbubbles break out, the kinetic feedback to the local star formation may be weaker, as the energy flows out of the galaxy before the superbubbles gain momentum (Fielding et al. 2018). Although our feedback model considers the non-uniformity of the ISM via anisotropic particle distribution, the impact of non-uniform ISM needs to be examined in the future with a more realistic setup and a higher resolution. For example, an analytical model considering the effect of superbubble breakout could be incorporated to construct a more realistic feedback model (Orr et al. 2021a).

There are several different weighting schemes to distribute mechanical feedback in particle simulation such as Hopkins et al. (2018); Hu (2019); Marinacci et al. (2019). However, the detailed distribution of particles on sub-resolution scales is somewhat random, and the exact weighting scheme does not matter very much in the final outcome as long as it is isotropic.

The models of [Kimm & Cen \(2014\)](#) and [Hopkins et al. \(2018\)](#) estimated the momentum by scaling that of isolated supernova explosions. However, the superbubble momentum also depends on the time interval of supernova explosions as we show in this work. Here we develop a more realistic model by using a universal scaling relation for the superbubble terminal momentum and radius, and this is where our model is different from [Kimm & Cen \(2014\)](#) and [Hopkins et al. \(2018\)](#).

In addition to momentum feedback, thermal feedback was also considered by [Kimm & Cen \(2014\)](#) and [Hopkins et al. \(2018\)](#), where they simply injected thermal energy. However, thermal feedback will not work if the model is not constructed to avoid overcooling ([Hu 2019](#)). Therefore, in our model, we adopt a stochastic thermal feedback model. In the isolated galaxy test, we show that the thermal outflow is driven by the stochastic model.

[Dalla Vecchia & Schaye \(2012\)](#) constructed a stochastic thermal feedback model with temperature rise, ΔT , as a free parameter. However, the temperature is not constant during the evolution of high-temperature bubbles formed by supernova explosions. Therefore, a parameter survey is necessary to determine ΔT , and using temperature as a model parameter is not so ideal as we discuss in Section 3.5. Instead, we use entropy as a parameter in our model. Since the high-temperature outflow gas expands adiabatically, the entropy is constant and its value can be determined based on high-resolution simulations.

In our model, we also provide momentum feedback in addition to thermal feedback. As shown in the isolated galaxy test, thermal feedback can only suppress star formation weakly. This is because the spatial resolution required to solve for the time evolution of SNR is more stringent than the mass resolution required to resolve for hot SN bubbles.

Our thermal feedback model heats gas particles up to a fixed entropy, which means denser gas particles are heated to higher temperatures. In high- z galaxies where the gas density is higher than in the local ones, our thermal feedback would become stronger. [Arata et al. \(2020\)](#) performed cosmological galaxy simulations using the stochastic thermal feedback model by [Dalla Vecchia & Schaye \(2012\)](#), with $\Delta T = 10^{7.5}$ K and studied metal-emission lines from high- z galaxies. They showed that the radial profile of [C II] surface brightness of simulated galaxies is lower at outer radius than observation. This discrepancy could be resolved by our stronger thermal feedback. In future works, we will investigate the impact of our SN feedback model in a cosmological context.

Our SN feedback model injects both terminal momentum and thermal energy from SNe, which may overesti-

mate the feedback effect. In reality, some SN energy is used to drive a superbubble and the other is used to accelerate outflows after the break-out of the superbubble. [Orr et al. \(2021a\)](#) developed an analytic model for clustered SNe in a galactic disk, and their model predicts that the superbubble is more likely to break out in an environment with rich gas and short dynamical times, which is consistent with observations and simulations ([Orr et al. 2021b](#)). Their model could be incorporated into our SN feedback model in the future.

6. CONCLUSIONS

In the first part of this paper, we performed idealized superbubble simulations using ATHENA++ to study the dependency of its momentum on the density, metallicity, and interval of SN explosions. Our ATHENA++ simulations included cooling, heating, thermal conduction, and turbulence. We injected thermal SN energy $E_{\text{SN}} = 10^{51}$ erg into the turbulent medium 10 times with fixed time intervals of $\Delta t_{\text{SN}} = 0.01, 0.1, 1$ Myr. We find that superbubble momentum at metallicity $Z = 10^{-3} Z_{\odot}$ is larger by a factor of two than that at $Z = 1 Z_{\odot}$ owing to a long Sedov-Taylor phase caused by later shell-formation time.

To interpret the simulation results, we extend the analytic solution of the SNR shell-formation time by [Kim & Ostriker \(2015\)](#) to include the effect of metallicity (Eq. 6), and obtained the analytic solution of the superbubble shell-formation time in Eq. (12). We normalized the time evolution of superbubble momentum in the simulation by the analytic time and momentum at shell formation and find that the normalized time evolution is universal (Fig. 9) as previously shown and described as “congruent” by [Kim & Ostriker \(2015\)](#). We note that [Kim et al. \(2017\)](#) normalized only the time variable by $t_{\text{sf,m}}$ for the multiple SN explosion simulation, however we also do the same for the momentum and derived the fitting function. From the universal time evolution model of superbubble momentum (Eq. 28), we derived a momentum per SN, averaged over the initial stellar cluster mass function (Eq. 33), which is useful for the application to the subgrid model of galaxy simulations.

In Appendix C, we outline the physical conditions for effective thermal/kinetic feedback and the necessity of subgrid feedback models. Therefore, in the second part of this paper (Sec 3), we developed mechanical and thermal SN feedback models. We distribute ejecta mass, metal, momentum, and energy from the SN feedback to neighboring gas particles based on the solid angle of a face on a Voronoi polyhedron, obtained by utilizing the STRIPACK algorithm with projected particle distribution on a sphere (Fig. 10), guaranteeing isotropy, energy-

and momentum-conservation. Note that our method is similar to, but different in detail from that of Hopkins et al. (2018) (See Section 3.3). We estimate the momentum input from SN feedback using Eq. (33) considering the effect of multiple SN explosions rather than just using a formula for a single SN. We also developed a stochastic thermal feedback model to reproduce hot outflow driven by SNe, as described in Section 3.5. Our thermal feedback model uses entropy as a controlling parameter rather than temperature.

In the third part of this paper, we implemented the above models into isolated galaxy simulation using GADGET3-OSAKA code. We find that mechanical feedback maintains the galactic disk against gravitational collapse (Fig. 11) and suppresses star formation, while stochastic thermal feedback can only suppress star formation weakly. (Fig. 16). The mechanical feedback is more efficient in driving cool outflow than the thermal feedback model by about a factor of two as shown in the middle column of Fig. 18. We also find that the stochastic thermal feedback drives hot outflow while non-stochastic thermal feedback does not (Figs. 18, 19). Our result is consistent with that of Hu (2019).

As we discussed in Section 1, there are various methods to overcome the overcooling problem. In this work, we adopted stochastic injection and avoided the delayed cooling model since it is unphysical. The multiphase ISM model becomes effectively similar to the delayed cooling model when thermal energy is stored in the hot phase, and here we did not consider this model. In the case of our stochastic thermal feedback model, we adopted a sufficiently high value of target entropy (S_{OF}) as the controlling parameter, which allowed us to alleviate the overcooling problem and eject metals out of

the galactic plane. However, thermal feedback can only suppress star formation weakly (Figs. 16, 17), and mechanical feedback is also necessary as we formulated in Section 3.4.

Our next step will be to perform zoom-in and full-box cosmological simulations using our SN feedback models developed in this paper and compare them with observations such as star formation histories and mass-metallicity relations of galaxies. Further comparisons against recent CGM metal line observations (both absorption and emission) such as the Keck Baryonic Structure Survey (KBSS; Rudie et al. 2012; Steidel et al. 2014) and the Muse GAs FLOW and Wind (MEGAFLOW) survey (Schroetter et al. 2016, 2019, 2021; Zabl et al. 2019, 2020, 2021; Wendt et al. 2021; Freundlich et al. 2021), can be more discriminatory tests of different models (Turner et al. 2017; Fujimoto et al. 2019; Chen et al. 2020; Nagamine et al. 2021; DeFelippis et al. 2021).

ACKNOWLEDGEMENTS

We are grateful to Volker Springel for providing the original version of GADGET-3, on which the GADGET3-OSAKA code is based. Our numerical simulations and analyses were carried out on the XC50 systems at the Center for Computational Astrophysics (CfCA) of the National Astronomical Observatory of Japan (NAOJ), OCTOPUS at the Cybermedia Center, Osaka University, and Oakforest-PACS at the University of Tokyo as part of the HPCI System Research Project (hp200041, hp210090). This work is supported by the JSPS KAKENHI Grant Number 21J20930 (YO), 16H05998, 18H05440, 21H04487 (KT), JP17H01111, 19H05810, 20H00180 (KN). KN acknowledges the travel support from the Kavli IPMU, World Premier Research Center Initiative (WPI), where part of this work was conducted.

APPENDIX

A. ANALYTIC THEORY OF SINGLE SNR

In the following section, the number density ratio of hydrogen to helium atoms in the interstellar medium (ISM) is assumed to be 10:1 unless otherwise specified. Other heavy elements are not considered. We also assume the ISM to be unionized. In this case, the mean molecular weight is $\mu = \rho/(m_{\text{H}}n) = 1.4$ and the specific heat ratio is $\gamma = 5/3$.

In the initial stage of SNR time evolution, the mass ejected by the SN explosion expands with velocity

$$v_{\text{ej}} = \sqrt{\frac{2E_{\text{SN}}}{M_{\text{ej}}}} = 7 \times 10^3 \text{ km s}^{-1} \left(\frac{E_{\text{SN}}}{10^{51} \text{ erg}} \right)^{1/2} \left(\frac{M_{\text{ej}}}{2 M_{\odot}} \right)^{-1/2} \quad (\text{A1})$$

while conserving kinetic energy and momentum, where E_{SN} is the kinetic energy of the SN ejecta and M_{ej} is the ejecta mass. This is called the free expansion phase.

When the SNR sweeps up the surrounding gas and the collected mass increases to approximately that of the ejecta, the mass gain of the swept-up gas can no longer be ignored, and the SNR enters the Sedov–Taylor phase.

The radius and time at this point are:

$$R_{\text{free}} = \left(\frac{2 M_{\text{ej}}}{(4/3)\pi\rho} \right)^{1/3} = 3 \text{ pc} \left(\frac{M_{\text{ej}}}{2 M_{\odot}} \right)^{1/3} n_0^{-1/3}, \quad (\text{A2})$$

$$t_{\text{free}} = \frac{R_{\text{free}}}{v_{\text{ej}}} = 4 \text{ kyr} \left(\frac{M_{\text{ej}}}{2 M_{\odot}} \right)^{5/6} n_0^{1/3}. \quad (\text{A3})$$

In the Sedov–Taylor phase, the SNR is hot, and the cooling effect is negligible until the cooling time. Therefore, the SNR grows while conserving energy, and its momentum increases as it sweeps up the surrounding gas and increases its mass. Its time evolution is represented by the Sedov–Taylor self-similar solution. The dimensionless quantity ξ of the self-similar solution is created from the radius r , energy E , density ρ of the ISM, and time t ;

$$\xi = \left(\frac{\rho}{E} \right)^{1/5} \frac{r}{t^{2/5}}. \quad (\text{A4})$$

The value of the dimensionless quantity at the shock surface is $\xi_0 \sim 1.15$ (Draine 2011).

Here, we estimate the thermal energy of the hot gas inside the shell at the shell-formation to calculate the SNR evolution after shell formation. We have the Rankine–Hugoniot relations for a strong shock ($\mathcal{M} \gg 1$, where \mathcal{M} is the Mach number):

$$\rho_{\text{shell}} = 4\rho_{\text{ISM}}, \quad (\text{A5})$$

$$v_{\text{shell}} = \frac{3}{4}\dot{R}, \quad (\text{A6})$$

$$P_{\text{shell}} = \frac{3}{4}\rho_{\text{ISM}}\dot{R}^2, \quad (\text{A7})$$

where ρ_{shell} , v_{shell} , and P_{shell} are the shell density, velocity, and pressure, respectively. We assume that the shell has a uniform density at the Sedov–Taylor phase. From the Rankine–Hugoniot relation and the mass conservation,

$$\rho_{\text{ISM}} \frac{4}{3}\pi R^3 = \rho_{\text{shell}} 4\pi R^2 \Delta R, \quad (\text{A8})$$

we obtain the thickness of the shell $\Delta R = (1/12)R$.

From the equation of motion,

$$\frac{d}{dt} \left(\rho_{\text{ISM}} \frac{4}{3}\pi R^3 v_{\text{shell}} \right) = 4\pi R^2 P_{\text{in}}, \quad (\text{A9})$$

we obtain the averaged pressure of the SNR,

$$P_{\text{in}} = (3/8)\rho_{\text{ISM}}\dot{R}^2. \quad (\text{A10})$$

The ratio of the thermal energy of the entire SNR, E_{tot} , to that of the shell, E_{shell} , is

$$\frac{E_{\text{shell}}}{E_{\text{tot}}} = \frac{\frac{3}{2}P_{\text{shell}}4\pi R^2 \Delta R}{\frac{3}{2}P_{\text{in}}\frac{4}{3}\pi R^3} = \frac{1}{2}. \quad (\text{A11})$$

This means that one half of the thermal energy of the SNR is in the shell, while the other is in the gas inside

the shell. When a low-temperature, high-density shell is formed, its thermal energy is radiated out. In the Sedov–Taylor phase, 72% of the total energy is thermal energy (Cioffi et al. 1988). During the formation of the low-temperature high-density shell, half of the thermal energy, or 36% of the total energy, will be radiated.

In the PDS phase, we assume that there is hot gas inside the low-temperature, high-density shell, and that the shell is driven by the adiabatic expansion of the hot gas. The SNR time evolution is obtained from Poisson’s equation and the equation of motion of the shell,

$$P \left(\frac{4}{3}\pi R^3 \right)^{5/3} = \text{const.} \quad (\text{A12})$$

$$\frac{d}{dt} \left(\frac{4}{3}\pi R^3 \rho \dot{R} \right) = 4\pi r^2 P, \quad (\text{A13})$$

and by assuming a solution of the form $R \propto t^\alpha$, we obtain $R \propto t^{2/7}$. Thus, $P t^{10/7} = \text{const.}$. Since the pressure inside the shell after shell formation is

$$\begin{aligned} P_{\text{st}} &= \frac{(\gamma - 1)0.36E_{51}}{(4/3)\pi R_{\text{sf}}^3} \\ &= 1.2 \times 10^6 k_{\text{B}} \text{ K cm}^{-3} E_{51}^{0.14} n_0^{1.3} \Lambda_{6,-22}^{0.39}, \end{aligned} \quad (\text{A14})$$

the time t_{PDS} at which the pressure inside the shell and the pressure in the ISM P_{ISM} are equal is estimated to be

$$t_{\text{PDS}} = 5.0 \times 10^6 \text{ yr } T_{\text{ISM},3}^{-0.7} E_{51}^{0.32} n_0^{-0.36} \Lambda_{6,-22}^{-0.053}, \quad (\text{A15})$$

where $T_{\text{ISM},3} = T_{\text{ISM}}/(10^3 \text{ K})$ is the temperature of the ISM. The radius and velocity at this time are

$$R_{\text{PDS}} = 89 \text{ pc } T_{\text{ISM},3}^{-0.2} E_{51}^{0.32} n_0^{-0.37} \Lambda_{6,-22}^{-0.053}, \quad (\text{A16})$$

$$V_{\text{PDS}} = 5.0 \text{ km s}^{-1} T_{\text{ISM},3}^{0.5}. \quad (\text{A17})$$

Since the speed of sound in the ISM is

$$c_s = \sqrt{\gamma \frac{P}{\rho}} = 3.1 T_3^{0.5} [\text{km s}^{-1}], \quad (\text{A18})$$

V_{PDS} is greater than the sound speed. In reality, the duration of the pressure-driven snowplow phase is shorter than the value of t_{PDS} derived here because of the loss of thermal energy of the hot gas inside the shell, which in turn is a result of the mixing between the shell and the gas, which was left unaccounted for here (Kim & Ostriker 2015).

When the pressure inside the shell drops to about the pressure of the ISM, the pressure-driven snowplow phase ends and transitions to the momentum-conserving snowplow phase. The time evolution is expressed in terms of momentum conservation,

$$\frac{d}{dt} \left(\frac{4}{3}\pi R^3 \rho \dot{R} \right) = 0, \quad (\text{A19})$$

and $R \propto t^{1/4}$. As the velocity of the SNR decreases to about the speed of sound, the SNR mixes with the ISM.

B. ANALYTIC THEORY OF SUPERBUBBLES AFTER SHELL FORMATION

Here, we briefly review two classical analytic models to describe the time evolution of a superbubble after shell formation: the pressure-driven and momentum-driven models. These models are distinguished by whether or not the pressure inside the shell is high enough to accelerate the shell.

B.1. Pressure-driven model

The shell is considered to be driven by gas pressure while the gas interior to the shell is overpressured against ISM (Weaver et al. 1977). Its time evolution is described by the equation of motion,

$$\frac{d}{dt} \left(\frac{4}{3} \pi R^3 \rho \dot{R} \right) = 4\pi R^2 P, \quad (\text{B20})$$

and the equation of the time evolution of energy inside the shell

$$\frac{d}{dt} \left(\frac{3}{2} P \left(\frac{4}{3} \pi R^3 \right) \right) = \frac{E_{\text{SN}}}{\Delta t_{\text{SN}}} - 4\pi R^2 P \dot{R}, \quad (\text{B21})$$

where the first term in the rhs is the energy injection rate from SN and the second term is the energy loss rate due to PdV work. Assuming a solution of the form $R = At^\alpha$, we obtain

$$R = \left(\frac{125}{154\pi} \right)^{1/5} E^{1/5} \Delta t_{\text{SN}}^{-1/5} \rho^{-1/5} t^{3/5}. \quad (\text{B22})$$

The momentum evolves in time with the following equation:

$$p = \frac{4}{3} \pi R^3 \dot{R} \propto t^{7/5}. \quad (\text{B23})$$

B.2. Momentum-driven model

After the pressure of the gas interior to the shell becomes comparable to that of ISM, the SNR gives momentum to drive the expanding shell (Avedisova 1972). The time evolution of the shell is

$$\frac{d}{dt} \left(\frac{4}{3} \pi R^3 \rho \dot{R} \right) = \frac{p_{\text{SNR}}}{\Delta t_{\text{SN}}}, \quad (\text{B24})$$

where p_{SNR} is the momentum given by the SNR of SN explosion inside the shell. Assuming that p_{SNR} is constant, the radius and momentum evolve in time with $R \propto t^{1/2}$, $p \propto t$, respectively.

C. RESOLUTION REQUIREMENT FOR THERMAL AND KINETIC FEEDBACK

Here, we analytically calculate the mass resolution requirement for thermal and kinetic feedback. Dalla Vecchia & Schaye (2012) estimated the resolution required for effective thermal feedback by comparing the sound-crossing time, t_s , with the cooling time, t_c . The sound-crossing time across a scale of spatial resolution $\Delta x = (m_{\text{gas}}/\rho)^{1/3}$ is

$$t_s = \frac{\Delta x}{c_s} = \left(\frac{\mu m_{\text{H}}}{\gamma k_{\text{B}} T} \right)^{1/2} \left(\frac{m_{\text{gas}}}{\rho} \right)^{1/3} = 1.0 \times 10^5 \text{ yr} \\ \times \left(\frac{\mu}{0.59} \right)^{1/6} \left(\frac{T}{10^{7.5} \text{ K}} \right)^{-1/2} \left(\frac{m_{\text{gas}}}{10^4 M_{\odot}} \right)^{1/3} \left(\frac{n_{\text{H}}}{1 \text{ cm}^{-3}} \right)^{-1/3}, \quad (\text{C25})$$

where c_s is the local sound speed. The cooling time is

$$t_c = \frac{nk_{\text{B}}T}{(\gamma-1)\Lambda_{ff}}, \quad (\text{C26})$$

where Λ_{ff} is the cooling rate by bremsstrahlung. Here, we consider the cooling time of gas with $T > 10^7 \text{ K}$, where bremsstrahlung is the dominant cooling process. Note that the cooling time we consider here is not that corresponding to a point explosion, i.e., the shell-formation time for SNR. We compare the cooling time for a gas particle with fixed density to the sound-crossing time to see if the heated gas particle is cooled down within the simulation time step or not. We can avoid overcooling if the cooling time is longer than the simulation time step, however, avoiding overcooling does not ensure that we resolve the Sedov–Taylor phase as we will discuss later in this section. The cooling rate by bremsstrahlung is (Draine 2011)

$$\Lambda_{ff} = 1.14 \times 10^{-23} \text{ erg cm}^{-3} \text{ s}^{-1} \left(\frac{n_{\text{H}}}{1 \text{ cm}^{-3}} \right)^2 \left(\frac{T}{10^{7.5} \text{ K}} \right)^{1/2}, \quad (\text{C27})$$

where we have assumed that the ratio of number density of hydrogen to helium is 10:1, the plasma is fully ionized, and the gaunt factor is 1.19. Combining Eq. (C26) and (C27), we obtain the cooling time as:

$$t_c = 4.2 \times 10^7 \text{ yr} \left(\frac{n_{\text{H}}}{1 \text{ cm}^{-3}} \right)^{-1} \left(\frac{T}{10^{7.5} \text{ K}} \right)^{1/2}. \quad (\text{C28})$$

The ratio between the sound-crossing and cooling times is:

$$\frac{t_c}{t_s} = 4.2 \times 10^2 \\ \times \left(\frac{\mu}{0.59} \right)^{-1/6} \left(\frac{n_{\text{H}}}{1 \text{ cm}^{-3}} \right)^{-2/3} \left(\frac{T}{10^{7.5} \text{ K}} \right) \left(\frac{m_{\text{gas}}}{10^4 M_{\odot}} \right)^{-1/3}. \quad (\text{C29})$$

The thermal feedback is effective when the cooling time is sufficiently longer than to the sound-crossing time, $t_c/t_s > 10$, which translates to

$$T > 7.5 \times 10^5 \text{ K} \left(\frac{\mu}{0.59} \right)^{1/6} \left(\frac{n_{\text{H}}}{1 \text{ cm}^{-3}} \right)^{2/3} \left(\frac{m_{\text{gas}}}{10^4 M_{\odot}} \right)^{1/3}. \quad (\text{C30})$$

The criterion temperature $T = 7.5 \times 10^5 \text{ K}$ is lower than the temperature where metal line radiative cooling dominates over bremsstrahlung (Fig. 1), therefore thermal feedback is effective when a gas particle is heated up to $T > 10^{7.5} \text{ K}$.

The conditions for kinetic feedback to be effective are more challenging than those for thermal feedback. Kim & Ostriker (2015) studied the resolution dependence of the terminal momentum of SNRs in 3D simulations using the ATHENA code, and showed that the criterion for convergence within 25% of the terminal momentum is $\Delta x/R_{\text{sf}} < 1/3$, where Δx is the spatial resolution, and R_{sf} is the shell-formation radius (Eq. 7). In order to satisfy this requirement in SPH, the following is necessary:

$$\frac{(m_{\text{gas}}/\rho)^{1/3}}{23E_{51}^{0.29}n_0^{-0.42}\Lambda_{6,-22}^{-0.13}\text{pc}} < \frac{1}{3}, \quad (\text{C31})$$

where m_{gas} is the SPH particle mass. Solving this equation for m_{gas} , we obtain

$$m_{\text{gas}} < 6.6 M_{\odot} \left(\frac{\mu}{0.59} \right) n_0^{-0.26} E_{51}^{0.87} \Lambda_{6,-22}^{-0.39}. \quad (\text{C32})$$

Hu (2019) investigated the resolution dependence of SNR terminal momentum with $E_{\text{SN}} = 10^{51} \text{ erg}$ in a uniform medium of $n_{\text{H}} = 1 \text{ cm}^{-3}$ at four mass resolutions, $m_{\text{gas}} = 0.1, 1, 10, \text{ and } 100 M_{\odot}$ using their modified version of GADGET-3 SPH code. They show that the terminal momentum converges in the cases of $m_{\text{gas}} = 0.1, \text{ and } 1 M_{\odot}$, and that the terminal momentum in the case of $m_{\text{gas}} = 10 M_{\odot}$ is about 15% smaller than that for $m_{\text{gas}} = 0.1, \text{ and } 1 M_{\odot}$, which is roughly consistent with the criterion in Eq. (C32). The reason why the terminal momentum converges within 15% even in the case of $m_{\text{gas}} = 10 M_{\odot}$ might be because the spatial resolution of SPH becomes better in a dense shell. The terminal momentum in the case of $m_{\text{gas}} = 100 M_{\odot}$ is underestimated by a factor of 3 due to overcooling (Hu 2019).

We can also solve Eq. (C31) for $E (= E_{51} \times 10^{51} \text{ erg})$ to find the injection energy when the shell-formation radius becomes large enough to be resolved well with the given mass resolution m_{gas} :

$$E > 4.5 \times 10^{54} \text{ erg} \left(\frac{\mu}{0.59} \right)^{-1.2} \left(\frac{m_{\text{gas}}}{10^4 M_{\odot}} \right)^{1.2} n_0^{0.30} \Lambda_{6,-22}^{0.45}, \quad (\text{C33})$$

and obtain the temperature at which the criterion, $\Delta x/R_{\text{sf}} < 1/3$, is satisfied:

$$T = \frac{\mu m_{\text{H}}}{(\gamma - 1) m_{\text{gas}} k_{\text{B}}} \frac{E}{m_{\text{gas}} k_{\text{B}}} > 1.6 \times 10^9 \text{ K} \left(\frac{\mu}{0.59} \right)^{-0.2} \left(\frac{m_{\text{gas}}}{10^4 M_{\odot}} \right)^{0.2} n_0^{0.3} \Lambda_{6,-22}^{0.45}. \quad (\text{C34})$$

This temperature is much higher than the one for the thermal feedback to become effective (Eq. C30), which means that the condition for kinetic feedback is more stringent and difficult to be realized in actual simulations. Therefore, kinetic feedback needs to be implemented as a subgrid model in current hydrodynamic simulations.

D. RESOLUTION TEST OF SN FEEDBACK MODEL IN AN ISOLATED GALAXY SIMULATION

In this section, we perform a higher-resolution isolated galaxy simulation to test its dependence on resolution. In the ‘High-reso’ run, ten times more particles are employed, so the mass resolution is ten times better. We adopt a fixed gravitational softening length of $\epsilon_{\text{grav}} = 40 \text{ pc}$ for the High-reso run. We use the same input parameters with the Fiducial run.

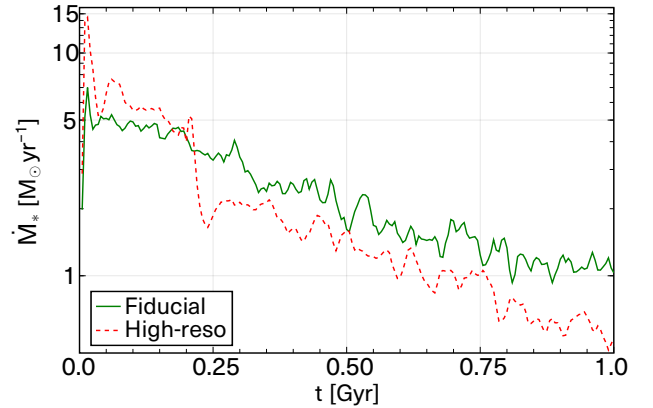


Figure 20. Star formation rate as a function of time for the Fiducial and High-reso runs.

Fig. 20 shows the SFR history of the Fiducial and High-reso runs. The SFR in the High-reso run is higher than that in the Fiducial run up to $t \sim 0.2 \text{ Gyr}$, after which the SFR declines rapidly due to local instability and a bursty star formation event. The discrepancy in SF history was also observed by Hopkins et al. (2018), who performed cosmological zoom-in simulations using GIZMO with their mechanical feedback model with different mass resolutions, and they demonstrate that the

SF history converges at $m_{\text{gas}} < 100 M_{\odot}$. Lupi (2019) performed isolated galaxy simulations using GIZMO with a similar but slightly modified SN feedback model by Hopkins et al. (2018), and an SF recipe considering log-normal density distribution in sub-grid turbulent ISM (Federrath & Klessen 2012; Semenov et al. 2017). They show that the SF history converges at the same resolution with our Fiducial and High-reso runs. Thus, the discrepancy we see in Fig. 20 could be reduced with different SF recipes.

Fig. 21 shows the outflow profiles of the Fiducial and High-reso runs up to 10 kpc above the galactic plane. The mass, energy, and metal loading factors of the hot component for the High-reso run is about a factor of two higher than those of the Fiducial run.

Fig. 22 shows the outflow profiles of the Fiducial and High-reso runs up to 200 kpc in spherical radius. We

see that the High-reso run has higher mass, energy, and metal loading factors than the Fiducial run due to its higher SFR during the first ~ 0.2 Gyr.

These two figures (Figs. 21 & 22) show that the perfect convergence is still difficult to achieve even with the implementation of subgrid kinetic feedback model, given the very stringent resolution requirement described in Appendix C as well as the impact of fluctuating star formation rate when the resolution is changed. In particular, the initial starburst at $t < 0.1$ Gyr has a significant impact in the later SF history as we see in Fig. 20, such as the sharp drop in SFR of High-reso run at $t \simeq 0.2$ Gyr. In order to understand the differences we see in Fig. 21 we would need to understand the origin of hot and cold outflow component in more detail, but this is beyond the scope of current paper and we will study these issues in our future work.

REFERENCES

- Agertz, O., Kravtsov, A. V., Leitner, S. N., & Gnedin, N. Y. 2013, *ApJ*, 770, 25, doi: [10.1088/0004-637X/770/1/25](https://doi.org/10.1088/0004-637X/770/1/25)
- Agertz, O., Pontzen, A., Read, J. I., et al. 2020, *MNRAS*, 491, 1656, doi: [10.1093/mnras/stz3053](https://doi.org/10.1093/mnras/stz3053)
- Anders, E., & Grevesse, N. 1989, *GeoCoA*, 53, 197, doi: [10.1016/0016-7037\(89\)90286-X](https://doi.org/10.1016/0016-7037(89)90286-X)
- Aoyama, S., Hou, K.-C., Shimizu, I., et al. 2017, *MNRAS*, 466, 105, doi: [10.1093/mnras/stw3061](https://doi.org/10.1093/mnras/stw3061)
- Arata, S., Yajima, H., Nagamine, K., Abe, M., & Khochfar, S. 2020, *MNRAS*, 498, 5541, doi: [10.1093/mnras/staa2809](https://doi.org/10.1093/mnras/staa2809)
- Armillotta, L., Krumholz, M. R., Di Teodoro, E. M., & McClure-Griffiths, N. M. 2019, *MNRAS*, 490, 4401, doi: [10.1093/mnras/stz2880](https://doi.org/10.1093/mnras/stz2880)
- Avedisova, V. S. 1972, *Soviet Ast.*, 15, 708
- Badjin, D. A., Glazyrin, S. I., Manukovskiy, K. V., & Blinnikov, S. I. 2016, *MNRAS*, 459, 2188, doi: [10.1093/mnras/stw790](https://doi.org/10.1093/mnras/stw790)
- Bessell, M. S., Sutherland, R. S., & Ruan, K. 1991, *ApJL*, 383, L71, doi: [10.1086/186244](https://doi.org/10.1086/186244)
- Bigiel, F., Leroy, A., Walter, F., et al. 2008, *AJ*, 136, 2846, doi: [10.1088/0004-6256/136/6/2846](https://doi.org/10.1088/0004-6256/136/6/2846)
- Blondin, J. M., Wright, E. B., Borkowski, K. J., & Reynolds, S. P. 1998, *ApJ*, 500, 342, doi: [10.1086/305708](https://doi.org/10.1086/305708)
- Blumenthal, G. R., Faber, S. M., Primack, J. R., & Rees, M. J. 1984, *Nature*, 311, 517, doi: [10.1038/311517a0](https://doi.org/10.1038/311517a0)
- Borrow, J., Schaller, M., & Bower, R. G. 2021, *MNRAS*, 505, 2316, doi: [10.1093/mnras/stab1423](https://doi.org/10.1093/mnras/stab1423)
- Bower, R. G., Schaye, J., Frenk, C. S., et al. 2017, *MNRAS*, 465, 32, doi: [10.1093/mnras/stw2735](https://doi.org/10.1093/mnras/stw2735)
- Bucciantini, N., Amato, E., Bandiera, R., Blondin, J. M., & Del Zanna, L. 2004, *A&A*, 423, 253, doi: [10.1051/0004-6361:20040360](https://doi.org/10.1051/0004-6361:20040360)
- Cen, R., & Ostriker, J. P. 1992, *ApJL*, 399, L113, doi: [10.1086/186620](https://doi.org/10.1086/186620)
- . 1999, *ApJ*, 514, 1, doi: [10.1086/306949](https://doi.org/10.1086/306949)
- Chabrier, G. 2003, *PASP*, 115, 763, doi: [10.1086/376392](https://doi.org/10.1086/376392)
- Chen, Y., Steidel, C. C., Hummels, C. B., et al. 2020, *MNRAS*, 499, 1721, doi: [10.1093/mnras/staa2808](https://doi.org/10.1093/mnras/staa2808)
- Chevalier, R. A. 1974, *ApJ*, 188, 501, doi: [10.1086/152740](https://doi.org/10.1086/152740)
- Chevalier, R. A., & Clegg, A. W. 1985, *Nature*, 317, 44, doi: [10.1038/317044a0](https://doi.org/10.1038/317044a0)
- Cioffi, D. F., McKee, C. F., & Bertschinger, E. 1988, *ApJ*, 334, 252, doi: [10.1086/166834](https://doi.org/10.1086/166834)
- Cowie, L. L., & McKee, C. F. 1977, *ApJ*, 211, 135, doi: [10.1086/154911](https://doi.org/10.1086/154911)
- Cox, D. P. 1986, *ApJ*, 304, 771, doi: [10.1086/164214](https://doi.org/10.1086/164214)
- Cox, D. P., & Anderson, P. R. 1982, *ApJ*, 253, 268, doi: [10.1086/159632](https://doi.org/10.1086/159632)
- Dalla Vecchia, C., & Schaye, J. 2012, *MNRAS*, 426, 140, doi: [10.1111/j.1365-2966.2012.21704.x](https://doi.org/10.1111/j.1365-2966.2012.21704.x)
- Dalton, G., Trager, S. C., Abrams, D. C., et al. 2012, in *Society of Photo-Optical Instrumentation Engineers (SPIE) Conference Series*, Vol. 8446, *Ground-based and Airborne Instrumentation for Astronomy IV*, ed. I. S. McLean, S. K. Ramsay, & H. Takami, 84460P, doi: [10.1117/12.925950](https://doi.org/10.1117/12.925950)
- DeFelippis, D., Bouché, N. F., Genel, S., et al. 2021, *ApJ*, 923, 56, doi: [10.3847/1538-4357/ac2cbf](https://doi.org/10.3847/1538-4357/ac2cbf)
- Dehnen, W., & Aly, H. 2012, *MNRAS*, 425, 1068, doi: [10.1111/j.1365-2966.2012.21439.x](https://doi.org/10.1111/j.1365-2966.2012.21439.x)

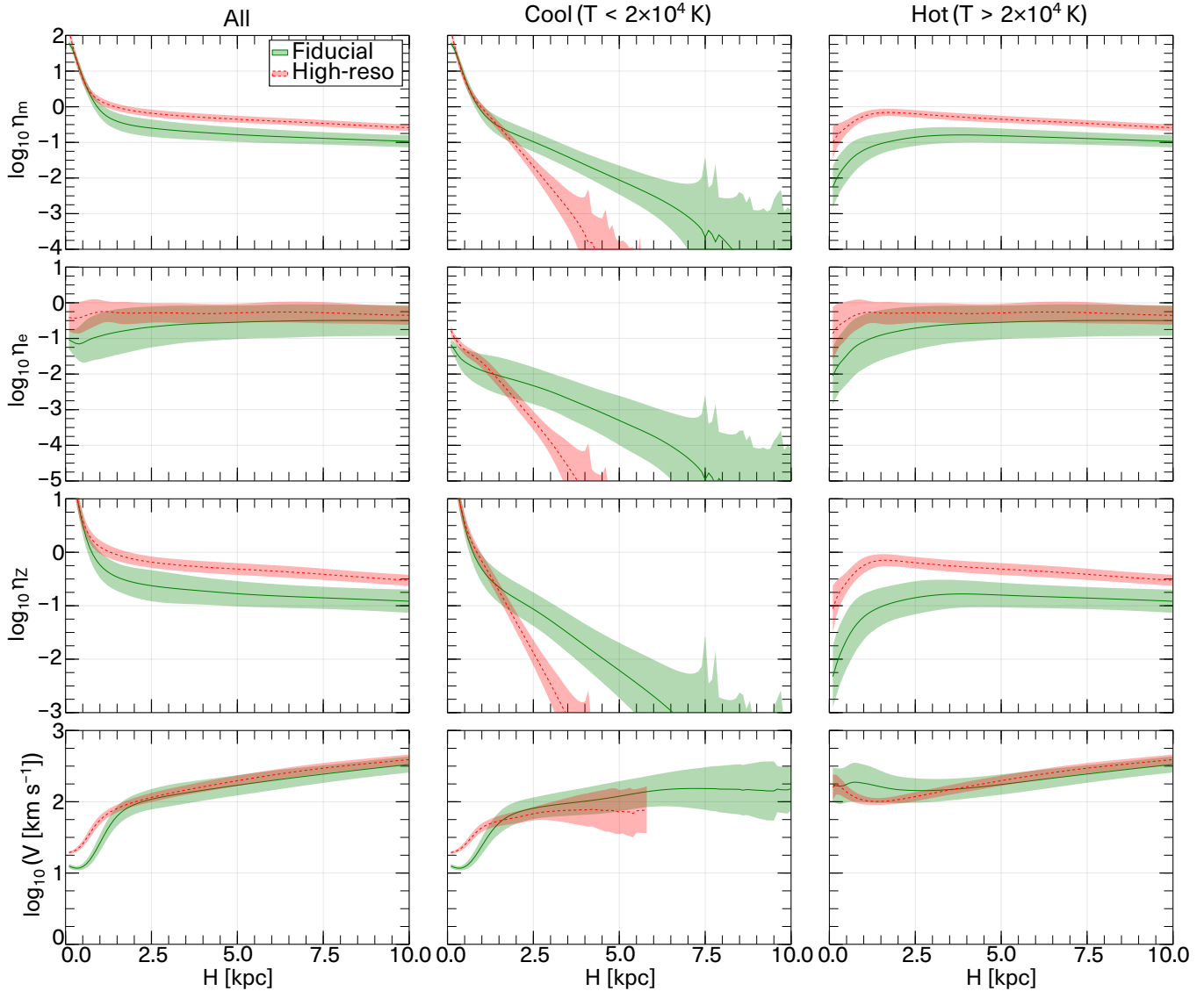


Figure 21. Same as Figure 18 but for the Fiducial and High-reso runs.

Dekel, A., Sarkar, K. C., Jiang, F., et al. 2019, MNRAS, 488, 4753, doi: [10.1093/mnras/stz1919](https://doi.org/10.1093/mnras/stz1919)

Dekel, A., & Silk, J. 1986, ApJ, 303, 39, doi: [10.1086/164050](https://doi.org/10.1086/164050)

Draine, B. T. 2011, Physics of the Interstellar and Intergalactic Medium

Durier, F., & Dalla Vecchia, C. 2012, MNRAS, 419, 465, doi: [10.1111/j.1365-2966.2011.19712.x](https://doi.org/10.1111/j.1365-2966.2011.19712.x)

El-Badry, K., Ostriker, E. C., Kim, C.-G., Quataert, E., & Weisz, D. R. 2019, MNRAS, 490, 1961, doi: [10.1093/mnras/stz2773](https://doi.org/10.1093/mnras/stz2773)

Federrath, C., & Klessen, R. S. 2012, ApJ, 761, 156, doi: [10.1088/0004-637X/761/2/156](https://doi.org/10.1088/0004-637X/761/2/156)

Ferland, G. J., Porter, R. L., van Hoof, P. A. M., et al. 2013, RMxAA, 49, 137. <https://arxiv.org/abs/1302.4485>

Ferrand, G., & Marcowith, A. 2010, A&A, 510, A101, doi: [10.1051/0004-6361/200913520](https://doi.org/10.1051/0004-6361/200913520)

Fielding, D., Quataert, E., & Martizzi, D. 2018, MNRAS, 481, 3325, doi: [10.1093/mnras/sty2466](https://doi.org/10.1093/mnras/sty2466)

Fielding, D. B., Ostriker, E. C., Bryan, G. L., & Jermyn, A. S. 2020, ApJL, 894, L24, doi: [10.3847/2041-8213/ab8d2c](https://doi.org/10.3847/2041-8213/ab8d2c)

Freundlich, J., Bouché, N. F., Contini, T., et al. 2021, MNRAS, 501, 1900, doi: [10.1093/mnras/staa3818](https://doi.org/10.1093/mnras/staa3818)

Fujimoto, S., Ouchi, M., Ferrara, A., et al. 2019, ApJ, 887, 107, doi: [10.3847/1538-4357/ab480f](https://doi.org/10.3847/1538-4357/ab480f)

Gatto, A., Walch, S., Low, M. M. M., et al. 2015, MNRAS, 449, 1057, doi: [10.1093/mnras/stv324](https://doi.org/10.1093/mnras/stv324)

Gentry, E. S., Krumholz, M. R., Dekel, A., & Madau, P. 2017, MNRAS, 465, 2471, doi: [10.1093/mnras/stw2746](https://doi.org/10.1093/mnras/stw2746)

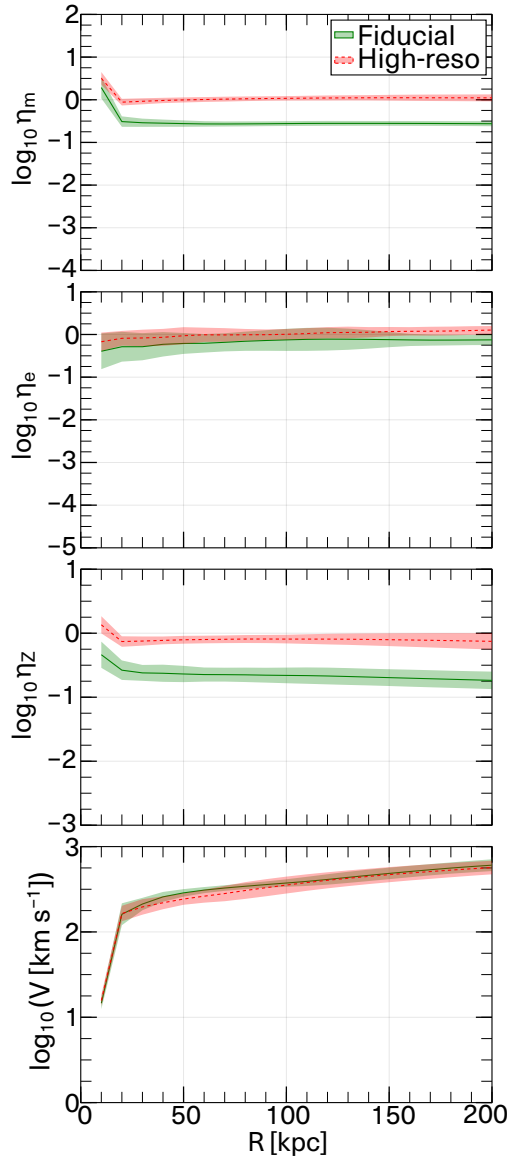


Figure 22. Same as Figure 19 but for the Fiducial and High-reso runs.

Gentry, E. S., Krumholz, M. R., Madau, P., & Lupi, A.

2019, MNRAS, 483, 3647, doi: [10.1093/mnras/sty3319](https://doi.org/10.1093/mnras/sty3319)

Gutcke, T. A., Pakmor, R., Naab, T., & Springel, V. 2021,

MNRAS, 501, 5597, doi: [10.1093/mnras/staa3875](https://doi.org/10.1093/mnras/staa3875)

Haardt, F., & Madau, P. 2012, ApJ, 746, 125,

doi: [10.1088/0004-637X/746/2/125](https://doi.org/10.1088/0004-637X/746/2/125)

Heitsch, F., Slyz, A. D., Devriendt, J. E. G., Hartmann,

L. W., & Burkert, A. 2006, ApJ, 648, 1052,

doi: [10.1086/505931](https://doi.org/10.1086/505931)

Helmholtz, H. v. 1868, Phil. Mag, 36, 337

Hennebelle, P., & Iffrig, O. 2014, A&A, 570, A81,

doi: [10.1051/0004-6361/201423392](https://doi.org/10.1051/0004-6361/201423392)

Hirai, Y., Fujii, M. S., & Saitoh, T. R. 2021, PASJ, 73, 1036, doi: [10.1093/pasj/psab038](https://doi.org/10.1093/pasj/psab038)

Höfner, S., & Olofsson, H. 2018, A&A Rv, 26, 1, doi: [10.1007/s00159-017-0106-5](https://doi.org/10.1007/s00159-017-0106-5)

Hopkins, P. F. 2013, MNRAS, 428, 2840, doi: [10.1093/mnras/sts210](https://doi.org/10.1093/mnras/sts210)

Hopkins, P. F., Quataert, E., & Murray, N. 2011, MNRAS, 417, 950, doi: [10.1111/j.1365-2966.2011.19306.x](https://doi.org/10.1111/j.1365-2966.2011.19306.x)

Hopkins, P. F., Wetzel, A., Kereš, D., et al. 2018, MNRAS, 477, 1578, doi: [10.1093/mnras/sty674](https://doi.org/10.1093/mnras/sty674)

Hu, C.-Y. 2019, MNRAS, 483, 3363, doi: [10.1093/mnras/sty3252](https://doi.org/10.1093/mnras/sty3252)

Inoue, T., Shimoda, J., Ohira, Y., & Yamazaki, R. 2013, ApJL, 772, L20, doi: [10.1088/2041-8205/772/2/L20](https://doi.org/10.1088/2041-8205/772/2/L20)

Itoh, H. 1978, PASJ, 30, 489

Karpov, P. I., Martizzi, D., Macias, P., et al. 2020, ApJ, 896, 66, doi: [10.3847/1538-4357/ab8f23](https://doi.org/10.3847/1538-4357/ab8f23)

Katz, N. 1992, ApJ, 391, 502, doi: [10.1086/171366](https://doi.org/10.1086/171366)

Katz, N., Weinberg, D. H., & Hernquist, L. 1996, ApJS, 105, 19, doi: [10.1086/192305](https://doi.org/10.1086/192305)

Kay, S. T., Thomas, P. A., & Theuns, T. 2003, MNRAS, 343, 608, doi: [10.1046/j.1365-8711.2003.06711.x](https://doi.org/10.1046/j.1365-8711.2003.06711.x)

Keller, B. W., Kruijssen, J. M. D., & Wadsley, J. W. 2020, MNRAS, 493, 2149, doi: [10.1093/mnras/staa380](https://doi.org/10.1093/mnras/staa380)

Keller, B. W., Wadsley, J., Benincasa, S. M., & Couchman, H. M. P. 2014, MNRAS, 442, 3013, doi: [10.1093/mnras/stu1058](https://doi.org/10.1093/mnras/stu1058)

Keller, B. W., Wadsley, J., & Couchman, H. M. P. 2015, MNRAS, 453, 3499, doi: [10.1093/mnras/stv1789](https://doi.org/10.1093/mnras/stv1789)

—. 2016, MNRAS, 463, 1431, doi: [10.1093/mnras/stw2029](https://doi.org/10.1093/mnras/stw2029)

Kim, C.-G., & Ostriker, E. C. 2015, ApJ, 802, 99, doi: [10.1088/0004-637X/802/2/99](https://doi.org/10.1088/0004-637X/802/2/99)

—. 2017, ApJ, 846, 133, doi: [10.3847/1538-4357/aa8599](https://doi.org/10.3847/1538-4357/aa8599)

—. 2018, ApJ, 853, 173, doi: [10.3847/1538-4357/aaa5ff](https://doi.org/10.3847/1538-4357/aaa5ff)

Kim, C.-G., Ostriker, E. C., & Raileanu, R. 2017, ApJ, 834, 25, doi: [10.3847/1538-4357/834/1/25](https://doi.org/10.3847/1538-4357/834/1/25)

Kim, C.-G., Ostriker, E. C., Somerville, R. S., et al. 2020a, ApJ, 900, 61, doi: [10.3847/1538-4357/aba962](https://doi.org/10.3847/1538-4357/aba962)

Kim, C.-G., Ostriker, E. C., Fielding, D. B., et al. 2020b, ApJL, 903, L34, doi: [10.3847/2041-8213/abc252](https://doi.org/10.3847/2041-8213/abc252)

Kim, J.-h., Abel, T., Agertz, O., et al. 2014, ApJS, 210, 14, doi: [10.1088/0067-0049/210/1/14](https://doi.org/10.1088/0067-0049/210/1/14)

Kim, J.-h., Agertz, O., Teyssier, R., et al. 2016, ApJ, 833, 202, doi: [10.3847/1538-4357/833/2/202](https://doi.org/10.3847/1538-4357/833/2/202)

Kimm, T., & Cen, R. 2014, ApJ, 788, 121, doi: [10.1088/0004-637X/788/2/121](https://doi.org/10.1088/0004-637X/788/2/121)

Kimm, T., Cen, R., Devriendt, J., Dubois, Y., & Slyz, A. 2015, MNRAS, 451, 2900, doi: [10.1093/mnras/stv1211](https://doi.org/10.1093/mnras/stv1211)

Kimm, T., Cen, R., Rosdahl, J., & Yi, S. K. 2016, ApJ, 823, 52, doi: [10.3847/0004-637X/823/1/52](https://doi.org/10.3847/0004-637X/823/1/52)

- Kolmogorov, A. 1941, *Akademiia Nauk SSSR Doklady*, 30, 301
- Koyama, H., & Inutsuka, S.-i. 2002, *ApJL*, 564, L97, doi: [10.1086/338978](https://doi.org/10.1086/338978)
- Krause, M., Fierlinger, K., Diehl, R., et al. 2013, *A&A*, 550, A49, doi: [10.1051/0004-6361/201220060](https://doi.org/10.1051/0004-6361/201220060)
- Krumholz, M. R., McKee, C. F., & Bland-Hawthorn, J. 2019, *ARA&A*, 57, 227, doi: [10.1146/annurev-astro-091918-104430](https://doi.org/10.1146/annurev-astro-091918-104430)
- Lancaster, L., Ostriker, E. C., Kim, J.-G., & Kim, C.-G. 2021a, *ApJ*, 914, 89, doi: [10.3847/1538-4357/abf8ab](https://doi.org/10.3847/1538-4357/abf8ab)
- . 2021b, *ApJ*, 914, 90, doi: [10.3847/1538-4357/abf8ac](https://doi.org/10.3847/1538-4357/abf8ac)
- Larson, R. B. 1974, *MNRAS*, 169, 229, doi: [10.1093/mnras/169.2.229](https://doi.org/10.1093/mnras/169.2.229)
- . 1981, *MNRAS*, 194, 809, doi: [10.1093/mnras/194.4.809](https://doi.org/10.1093/mnras/194.4.809)
- Laureijs, R., Amiaux, J., Arduini, S., et al. 2011, arXiv e-prints, arXiv:1110.3193. <https://arxiv.org/abs/1110.3193>
- Leitherer, C., Ekström, S., Meynet, G., et al. 2014, *ApJS*, 212, 14, doi: [10.1088/0067-0049/212/1/14](https://doi.org/10.1088/0067-0049/212/1/14)
- Leitherer, C., Ortiz Otálvaro, P. A., Bresolin, F., et al. 2010, *ApJS*, 189, 309, doi: [10.1088/0067-0049/189/2/309](https://doi.org/10.1088/0067-0049/189/2/309)
- Leitherer, C., Schaerer, D., Goldader, J. D., et al. 1999, *ApJS*, 123, 3, doi: [10.1086/313233](https://doi.org/10.1086/313233)
- Levi, M., Bebek, C., Beers, T., et al. 2013, arXiv e-prints, arXiv:1308.0847. <https://arxiv.org/abs/1308.0847>
- Li, M., & Bryan, G. L. 2020, *ApJL*, 890, L30, doi: [10.3847/2041-8213/ab7304](https://doi.org/10.3847/2041-8213/ab7304)
- Li, M., Bryan, G. L., & Ostriker, J. P. 2017, *ApJ*, 841, 101, doi: [10.3847/1538-4357/aa7263](https://doi.org/10.3847/1538-4357/aa7263)
- Lupi, A. 2019, *MNRAS*, 484, 1687, doi: [10.1093/mnras/stz100](https://doi.org/10.1093/mnras/stz100)
- Maoz, D., & Mannucci, F. 2012, *PASA*, 29, 447, doi: [10.1071/AS11052](https://doi.org/10.1071/AS11052)
- Marinacci, F., Sales, L. V., Vogelsberger, M., Torrey, P., & Springel, V. 2019, *MNRAS*, 489, 4233, doi: [10.1093/mnras/stz2391](https://doi.org/10.1093/mnras/stz2391)
- Martizzi, D., Faucher-Giguère, C.-A., & Quataert, E. 2015, *MNRAS*, 450, 504, doi: [10.1093/mnras/stv562](https://doi.org/10.1093/mnras/stv562)
- McKee, C. F., & Ostriker, J. P. 1977, *ApJ*, 218, 148, doi: [10.1086/155667](https://doi.org/10.1086/155667)
- Meshkov, E. E. 1972, *Fluid Dynamics*, 4, 101, doi: [10.1007/BF01015969](https://doi.org/10.1007/BF01015969)
- Minière, J., Bouquet, S. E., Michaut, C., Sanz, J., & Mancini, M. 2018, *A&A*, 617, A133, doi: [10.1051/0004-6361/201832663](https://doi.org/10.1051/0004-6361/201832663)
- Morris, J. P. 1996, *PASA*, 13, 97
- Nagamine, K., Fukugita, M., Cen, R., & Ostriker, J. P. 2001, *ApJ*, 558, 497, doi: [10.1086/322293](https://doi.org/10.1086/322293)
- Nagamine, K., Shimizu, I., Fujita, K., et al. 2021, *ApJ*, 914, 66, doi: [10.3847/1538-4357/abfa16](https://doi.org/10.3847/1538-4357/abfa16)
- Nakashima, S., Inoue, Y., Yamasaki, N., et al. 2018, *ApJ*, 862, 34, doi: [10.3847/1538-4357/aacceb](https://doi.org/10.3847/1538-4357/aacceb)
- Navarro, J. F., & White, S. D. M. 1993, *MNRAS*, 265, 271, doi: [10.1093/mnras/265.2.271](https://doi.org/10.1093/mnras/265.2.271)
- Ohlin, L., Renaud, F., & Agertz, O. 2019, *MNRAS*, 485, 3887, doi: [10.1093/mnras/stz705](https://doi.org/10.1093/mnras/stz705)
- Orr, M. E., Fielding, D. B., Hayward, C. C., & Burkhart, B. 2021a, arXiv e-prints, arXiv:2109.14656. <https://arxiv.org/abs/2109.14656>
- . 2021b, arXiv e-prints, arXiv:2109.14626. <https://arxiv.org/abs/2109.14626>
- Ostriker, E. C., & Shetty, R. 2011, *ApJ*, 731, 41, doi: [10.1088/0004-637X/731/1/41](https://doi.org/10.1088/0004-637X/731/1/41)
- Ostriker, J. P., & McKee, C. F. 1988, *Reviews of Modern Physics*, 60, 1, doi: [10.1103/RevModPhys.60.1](https://doi.org/10.1103/RevModPhys.60.1)
- Parker, E. N. 1963, *Interplanetary dynamical processes*.
- Portegies Zwart, S. F., McMillan, S. L. W., & Gieles, M. 2010, *ARA&A*, 48, 431, doi: [10.1146/annurev-astro-081309-130834](https://doi.org/10.1146/annurev-astro-081309-130834)
- Portinari, L., Chiosi, C., & Bressan, A. 1998, *A&A*, 334, 505. <https://arxiv.org/abs/astro-ph/9711337>
- Price, D. J. 2012, *Journal of Computational Physics*, 231, 759, doi: [10.1016/j.jcp.2010.12.011](https://doi.org/10.1016/j.jcp.2010.12.011)
- Rayleigh. 1882, *Proceedings of the London Mathematical Society*, s1-14, 170, doi: <https://doi.org/10.1112/plms/s1-14.1.170>
- Renka, R. J. 1997, *ACM Transactions on Mathematical Software (TOMS)*, 23, 416
- Richtmyer, R. 1960
- Rosdahl, J., Schaye, J., Dubois, Y., Kimm, T., & Teyssier, R. 2017, *MNRAS*, 466, 11, doi: [10.1093/mnras/stw3034](https://doi.org/10.1093/mnras/stw3034)
- Rosswog, S. 2009, *NewAR*, 53, 78, doi: [10.1016/j.newar.2009.08.007](https://doi.org/10.1016/j.newar.2009.08.007)
- Rudie, G. C., Steidel, C. C., Trainor, R. F., et al. 2012, *ApJ*, 750, 67, doi: [10.1088/0004-637X/750/1/67](https://doi.org/10.1088/0004-637X/750/1/67)
- Saitoh, T. R. 2017, *AJ*, 153, 85, doi: [10.3847/1538-3881/153/2/85](https://doi.org/10.3847/1538-3881/153/2/85)
- Saitoh, T. R., & Makino, J. 2009, *ApJL*, 697, L99, doi: [10.1088/0004-637X/697/2/L99](https://doi.org/10.1088/0004-637X/697/2/L99)
- . 2013, *ApJ*, 768, 44, doi: [10.1088/0004-637X/768/1/44](https://doi.org/10.1088/0004-637X/768/1/44)
- Sarkar, K. C., Gnat, O., & Sternberg, A. 2021, *MNRAS*, 504, 583, doi: [10.1093/mnras/stab582](https://doi.org/10.1093/mnras/stab582)
- Schaye, J., Crain, R. A., Bower, R. G., et al. 2015, *MNRAS*, 446, 521, doi: [10.1093/mnras/stu2058](https://doi.org/10.1093/mnras/stu2058)
- Schmidt, M. 1959, *ApJ*, 129, 243, doi: [10.1086/146614](https://doi.org/10.1086/146614)
- Schoenberg, I. J. 1946, *Quarterly of Applied Mathematics*, 4, 45

- Schroetter, I., Bouché, N., Wendt, M., et al. 2016, *ApJ*, 833, 39, doi: [10.3847/1538-4357/833/1/39](https://doi.org/10.3847/1538-4357/833/1/39)
- Schroetter, I., Bouché, N. F., Zabl, J., et al. 2019, *MNRAS*, 490, 4368, doi: [10.1093/mnras/stz2822](https://doi.org/10.1093/mnras/stz2822)
- . 2021, *MNRAS*, 506, 1355, doi: [10.1093/mnras/stab1447](https://doi.org/10.1093/mnras/stab1447)
- Schruba, A., Leroy, A. K., Walter, F., et al. 2011, *AJ*, 142, 37, doi: [10.1088/0004-6256/142/2/37](https://doi.org/10.1088/0004-6256/142/2/37)
- Semenov, V. A., Kravtsov, A. V., & Gnedin, N. Y. 2017, *ApJ*, 845, 133, doi: [10.3847/1538-4357/aa8096](https://doi.org/10.3847/1538-4357/aa8096)
- Shimizu, I., Oku, Y., Nagamine, K., Todoroki, K., & Yajima, H. 2020, *MNRAS*, 494, 598, doi: [10.1093/mnras/staa772](https://doi.org/10.1093/mnras/staa772)
- Shimizu, I., Todoroki, K., Yajima, H., & Nagamine, K. 2019, *MNRAS*, 484, 2632, doi: [10.1093/mnras/stz098](https://doi.org/10.1093/mnras/stz098)
- Shin, E.-J., Kim, J.-H., & Oh, B. K. 2021, *ApJ*, 917, 12, doi: [10.3847/1538-4357/abffd0](https://doi.org/10.3847/1538-4357/abffd0)
- Smith, B. D., Bryan, G. L., Glover, S. C. O., et al. 2017, *MNRAS*, 466, 2217, doi: [10.1093/mnras/stw3291](https://doi.org/10.1093/mnras/stw3291)
- Smith, M. C., Sijacki, D., & Shen, S. 2018, *MNRAS*, 478, 302, doi: [10.1093/mnras/sty994](https://doi.org/10.1093/mnras/sty994)
- Spergel, D., Gehrels, N., Baltay, C., et al. 2015, arXiv e-prints, arXiv:1503.03757. <https://arxiv.org/abs/1503.03757>
- Spitzer, Lyman, J. 1990, *ARA&A*, 28, 71, doi: [10.1146/annurev.aa.28.090190.000443](https://doi.org/10.1146/annurev.aa.28.090190.000443)
- Spitzer, L. 1962, *Physics of Fully Ionized Gases*
- Springel, V. 2005, *MNRAS*, 364, 1105, doi: [10.1111/j.1365-2966.2005.09655.x](https://doi.org/10.1111/j.1365-2966.2005.09655.x)
- Springel, V., & Hernquist, L. 2003, *MNRAS*, 339, 289, doi: [10.1046/j.1365-8711.2003.06206.x](https://doi.org/10.1046/j.1365-8711.2003.06206.x)
- Steidel, C. C., Rudie, G. C., Strom, A. L., et al. 2014, *ApJ*, 795, 165, doi: [10.1088/0004-637X/795/2/165](https://doi.org/10.1088/0004-637X/795/2/165)
- Stinson, G., Seth, A., Katz, N., et al. 2006, *MNRAS*, 373, 1074, doi: [10.1111/j.1365-2966.2006.11097.x](https://doi.org/10.1111/j.1365-2966.2006.11097.x)
- Stone, J. M., Tomida, K., White, C. J., & Felker, K. G. 2020, *ApJS*, 249, 4, doi: [10.3847/1538-4365/ab929b](https://doi.org/10.3847/1538-4365/ab929b)
- Strickland, D. K., & Heckman, T. M. 2009, *ApJ*, 697, 2030, doi: [10.1088/0004-637X/697/2/2030](https://doi.org/10.1088/0004-637X/697/2/2030)
- Su, K.-Y., Hopkins, P. F., Hayward, C. C., et al. 2019, *MNRAS*, 487, 4393, doi: [10.1093/mnras/stz1494](https://doi.org/10.1093/mnras/stz1494)
- Sutherland, R. S., & Dopita, M. A. 1993, *ApJS*, 88, 253, doi: [10.1086/191823](https://doi.org/10.1086/191823)
- Takada, M., Ellis, R. S., Chiba, M., et al. 2014, *PASJ*, 66, R1, doi: [10.1093/pasj/pst019](https://doi.org/10.1093/pasj/pst019)
- Taylor, G. I. 1950, *Proceedings of the Royal Society of London. Series A. Mathematical and Physical Sciences*, 201, 192, doi: [10.1098/rspa.1950.0052](https://doi.org/10.1098/rspa.1950.0052)
- Thacker, R. J., & Couchman, H. M. P. 2001, *ApJL*, 555, L17, doi: [10.1086/321739](https://doi.org/10.1086/321739)
- Thompson, W. S. 1871, *Phil. Mag.*, 374
- Thornton, K., Gaudlitz, M., Janka, H. T., & Steinmetz, M. 1998, *ApJ*, 500, 95, doi: [10.1086/305704](https://doi.org/10.1086/305704)
- Tomisaka, K., & Ikeuchi, S. 1986, *PASJ*, 38, 697
- Totani, T., Morokuma, T., Oda, T., Doi, M., & Yasuda, N. 2008, *PASJ*, 60, 1327, doi: [10.1093/pasj/60.6.1327](https://doi.org/10.1093/pasj/60.6.1327)
- Truelove, J. K., Klein, R. I., McKee, C. F., et al. 1997, *ApJL*, 489, L179, doi: [10.1086/310975](https://doi.org/10.1086/310975)
- Turner, M. L., Schaye, J., Crain, R. A., et al. 2017, *MNRAS*, 471, 690, doi: [10.1093/mnras/stx1616](https://doi.org/10.1093/mnras/stx1616)
- Valentini, M., Murante, G., Borgani, S., et al. 2017, *MNRAS*, 470, 3167, doi: [10.1093/mnras/stx1352](https://doi.org/10.1093/mnras/stx1352)
- Vázquez, G. A., & Leitherer, C. 2005, *ApJ*, 621, 695, doi: [10.1086/427866](https://doi.org/10.1086/427866)
- Vázquez-Semadeni, E., Gómez, G. C., Jappsen, A. K., et al. 2007, *ApJ*, 657, 870, doi: [10.1086/510771](https://doi.org/10.1086/510771)
- Veilleux, S., Cecil, G., & Bland-Hawthorn, J. 2005, *ARA&A*, 43, 769, doi: [10.1146/annurev.astro.43.072103.150610](https://doi.org/10.1146/annurev.astro.43.072103.150610)
- Vishniac, E. T. 1983, *ApJ*, 274, 152, doi: [10.1086/161433](https://doi.org/10.1086/161433)
- Weaver, R., McCray, R., Castor, J., Shapiro, P., & Moore, R. 1977, *ApJ*, 218, 377, doi: [10.1086/155692](https://doi.org/10.1086/155692)
- Wendt, M., Bouché, N. F., Zabl, J., Schroetter, I., & Muzahid, S. 2021, *MNRAS*, 502, 3733, doi: [10.1093/mnras/stab049](https://doi.org/10.1093/mnras/stab049)
- Wheeler, J. C., Sneden, C., & Truran, James W., J. 1989, *ARA&A*, 27, 279, doi: [10.1146/annurev.aa.27.090189.001431](https://doi.org/10.1146/annurev.aa.27.090189.001431)
- Yadav, N., Mukherjee, D., Sharma, P., & Nath, B. B. 2017, *MNRAS*, 465, 1720, doi: [10.1093/mnras/stw2522](https://doi.org/10.1093/mnras/stw2522)
- Yepes, G., Kates, R., Khokhlov, A., & Klypin, A. 1997, *MNRAS*, 284, 235, doi: [10.1093/mnras/284.1.235](https://doi.org/10.1093/mnras/284.1.235)
- Zabl, J., Bouché, N. F., Schroetter, I., et al. 2019, *MNRAS*, 485, 1961, doi: [10.1093/mnras/stz392](https://doi.org/10.1093/mnras/stz392)
- . 2020, *MNRAS*, 492, 4576, doi: [10.1093/mnras/stz3607](https://doi.org/10.1093/mnras/stz3607)
- Zabl, J., Bouché, N. F., Wisotzki, L., et al. 2021, *MNRAS*, 507, 4294, doi: [10.1093/mnras/stab2165](https://doi.org/10.1093/mnras/stab2165)